UNIVERSIDAD POLITECNICA DE VALENCIA

motores térmicos

TRABAJO DE FIN DE MÁSTER

Caracterización experimental de turbinas radiales de sobrealimentación bajo flujo pulsante y estudio numérico de un sistema de control activo

Realizado por: Ricardo Gozalbo Bellés
Dirigido por: Dr. Andrés Omar Tiseira

Valencia, 21 de Junio de 2010

Máster en
Motores de Combustión Interna Alternativos

DEPARTAMENTO DE MÁQUINAS Y MOTORES TÉRMICOS

Resumen

El estudio del flujo pulsante a la entrada de una turbina es de vital importancia para poder obtener la máxima energía de los gases de escape. Los estudios experimentales llevados a cabo demuestran que los factores más determinantes en el rendimiento de las turbinas bajo flujo pulsante son la frecuencia de pulsación y la distancia entre el punto de operación y el punto de rendimiento máxima de la turbina. Además, se ha desarrollado y validado una técnica basada en la física de la turbina para extrapolar los mapas de gasto y rendimiento de la turbina, ya que son fundamentales para la realización de simulaciones en códigos fluido-dinámicos unidimensionales. También se ha realizado un estudio numérico de los beneficios del concepto de control activo en turbinas cuando son acopladas a un motor reciproco de automoción.

Summary

The study of pulsating flow in turbines is vital in order to obtain the maximum energy from the exhaust gases. The experimental studies conducted show that the most important factors that affect the turbine performance and efficiency under pulsating flow conditions are the frequency of pulses and the distance between the operating point and the maximum efficiency point. An extrapolation technique based on turbine physics has also been developed and validated in order to allow for extrapolation of turbine mass flow and efficiency maps, as they are essential for one-dimensional gasdynamics simulation codes. A numerical study of the implementation of an active control turbocharger on automotive engines has also been carried out.

ÍNDICE

1. INTRODUCCIÓN

1.1. Motivación

Los turbocompresores son un medio ideal para aumentar la potencia de salida de un motor de combustión interna alternativo tanto gasolina como Diesel y son muy utilizados hoy en día, sobretodo en pequeños motores Diesel de automoción. Sin embargo, hay un problema fundamental que todavía no ha sido solucionado de forma satisfactoria y es la combinación no ideal entre un motor reciproco alternativo proporcionando energía a una máquina centrifuga como la turbina de un turbocompresor.

Incluso con el uso de las actuales turbinas de geometría variable (TGV), este desajuste no se elimina, ya que una TGV solo responde a cambios de puntos de operación [1]. Una TGV asume un flujo ideal, sin cambios para un punto de operación estacionario por cada posición de apertura de los alabes. En cambio, sin importar el punto de funcionamiento del motor, ya sea estacionario o transitorio, las condiciones de entrada a la turbina son siempre altamente pulsantes con grandes cambios de presión y gastos másicos en todo momento. La turbina no recibe nunca un flujo a presión y gasto másico constante, lo que sería lo ideal para una máquina centrifuga, lo cual afecta a su rendimiento global.

Otro método utilizado para mejorar la unión entre el motor recíproco y la turbina de sobrealimentación es el uso de una válvula de descarga (*waste-gate).* Este mecanismo permite derivar los gases de escape alrededor de la turbina permitiendo controlar el gasto másico a través de la turbina, además de controlar la contrapresión generada en el motor [2]. Pero desafortunadamente, este mecanismo tampoco es capaz de eliminar el flujo altamente pulsante proveniente del escape del motor, que afecta negativamente al rendimiento de la turbina, ya que solo responde a cambios del punto de operación y no instantáneamente.

A pesar de ser conscientes de la existencia del problema de acoplamiento fluido dinámico entre motor y turbina, se siguen utilizando los mapas característicos de turbinas para el estudio y modelado unidimensional de turbinas de sobrealimentación debido a la simplicidad de obtención de los mapas. Desafortunadamente, el cálculo del rendimiento de la turbina con dichos modelos no suele ser satisfactoria, ya que los mapas característicos provienen de bancos de ensayos de flujo continuo. Los modelos simples que interpolan las variables termodinámicas medias de dichos mapas y que asumen una turbina como adiabática, no suelen ofrecer buenos resultados.

Es por ello que se considera necesaria la realización de ensayos con flujo pulsante, tanto adiabáticos como no-adiabáticos, para estudiar el efecto producido por el flujo no estacionario en el rendimiento de la turbina. Para la realización de los ensayos existen diferentes tipos de bancos experimentales. Existen bancos específicos para turbinas radiales como los desarrollados por Winterbone et al [3] y Nikpour [4], los cuales utilizan dinamómetros hidráulicos para absorber la energía de la turbina. Arcounamis et al [5] utiliza un compresor radial en vez de un dinamómetro como freno para poder trabajar con turbinas de mayor tamaño. Szymko [6] también desarrolló otra instalación experimental en la que hizo uso de un dinamómetro de corrientes de Focault para absorber la energía, ya que la baja inercia del sistema otorga una mayor precisión en las medidas. Los bancos de ensayos comúnmente utilizados por la mayoría de los fabricantes de turbogrupos y del cual se dispone de uno de ellos en CMT-Motores Térmicos, son los que utilizan el mismo

compresor del turbogrupo como freno [7]. Una de las limitaciones principales de estos últimos, es que al utilizar al compresor como freno, solo se pueden obtener muy pocos puntos de operación en la turbina debido a los límites de choque y bombeo impuestos por el compresor.

Es por ello que también es muy importante desarrollar un método físico de extrapolación para la obtención de mapas de rendimiento completos de la turbina, los cuales son necesarios para los modelos de simulación fluido-dinámicos unidimensionales. Actualmente existen métodos de extrapolación desarrollados por Benson [8], Payri et al [9], and Serrano et al [10] los cuales son capaces de extrapolar de una forma muy fiable los mapas de gasto másico y relación de expansión de la turbina. Dichos métodos no son válidos para la extrapolación del mapa de relación cinemática y rendimiento. Por lo tanto, es necesario desarrollar una técnica de extrapolación de dichos mapas basándose en principios físicos y geométricos para que sea lo más fiable y robusta posible.

Pero no solo el estudio del efecto de los pulsos es importante para ver el efecto que tienen sobre el rendimiento de las turbinas, sino para poder desarrollar nuevos sistemas de acoplamiento entre el motor reciproco y la turbina centrifuga para poder aprovechar al máximo la energía contenida en los gases de escape.

Una solución propuesta son las turbinas con control activo (ACT). Las ACT son un tipo especial de TGV en donde los alabes de entrada al rotor son capaces de variar el área de entrada en fase y con la misma frecuencia que los pulsos de escape del motor. De esta manera, modificando continuamente el área efectiva a la entrada del rotor y adaptándose a las presiones instantáneas, se puede obtener más energía ya que la turbina siempre trabaja en su punto óptimo de operación. Es decir, ya que la turbina no solo se adaptaría al punto de operación del motor (función de una TGV) sino que también se adaptaría al flujo pulsante no estacionario para poder extraer el máximo de energía y mejorar el acoplamiento entre la máquina reciproca y la centrifuga.

El principal inconveniente de las ACT, es el hecho de que pueden surgir problemas de coordinación y desajustes [11], ya que el sistema ACT tiene que adaptarse constantemente a las variaciones de frecuencia y amplitud del fluido. De acuerdo con experimentos que ya se han llevado a cabo con este nuevo concepto de turbogrupo [12], el ACT presenta un buen potencial, obteniendo mejoras en el rendimiento de la turbina de entre 3% y 7%. Básicamente, esto demuestra que el concepto ACT es factible, ya que se consigue una mejora significativa del rendimiento, aunque se deberían llevar a cabo ensayos reales con motores para comprobar realmente su potencial.

El rendimiento de un motor de reciproco de cuatro tiempos es muy dependiente de la contrapresión y de las perdidas por bombeo. Los pulsos de contrapresión también son muy beneficiosos para la extracción de los gases de escape de la cámara de combustión, de ahí a que sea tan importante un buen diseño de los tubos de escape. El problema por tanto es que al instalar una turbina ACT dichos pulsos se van a cancelar, ya que al estar variando el área de entrada al rotor constantemente va a provocar la anulación de dichos pulsos. Por esta razón se hace totalmente necesario el estudio de una turbina ACT combinada con un motor de combustión interna, ya que aunque el rendimiento del turbogrupo aumenta, se desconoce cuál puede ser el efecto global en un motor turboalimentado.

1.2. Objetivos

Los objetivos principales son los siguientes:

- Estudio experimental del efecto de flujo pulsante en el rendimiento de la turbina tanto en condiciones adiabáticas, sin el efecto de transferencia de calor, como en condiciones no-adiabáticas.
- Desarrollo matemático basado en la física y geometría de una turbina para la extrapolación de los mapas de turbina, tanto de gasto másico como de rendimiento, para ser implementado en los códigos unidimensionales de simulación de turbinas
- Estudio numérico, validación e implementación del sistema de control activo de turbinas en un motor Diesel de automoción para intentar aprovechar el flujo de escape pulsante y extraer la máxima energía del fluido.

2. INSTALACIÓN EXPERIMENTAL

2.1. Banco de turbocompresores

Un esquema básico del banco de experimental de ensayo de turbogrupos utilizado para los ensayos de flujo pulsante se puede observar en la Figura 1. Este banco de pruebas ha sido diseñado por CMT-Motores Térmicos y tiene las siguientes características:

- Temperatura máxima a la entrada de la turbina: 674 K
- Presión máxima absoluta a la entrada de la turbina: 3.5 bar
- Gasto másico máximo: 0.19 kg/s

Lado de la turbina: Un compresor de tornillo de 55kW bombea el aire al banco de ensayos. El aire puede ser calentado hasta una temperatura de 674K utilizando un conjunto de cinco resistencias eléctricas. Calentar el aire es opcional y su temperatura puede ser regulada automáticamente dependiendo del tipo de ensayo a realizar. En caso de querer ensayar a muy bajas temperaturas, también existe la posibilidad de conectar un intercambiador de calor. Para generar el flujo pulsante, se utiliza una válvula rotativa que permite controlar tanto la frecuencia de los pulsos, como su forma y amplitud. Dicha válvula se describe con más detalle en la sección 2.2. La válvula rotativa también puede ser desconectada, lo cual permite realizar ensayos bajo condiciones de flujo continuo y estacionario. En la salida de la turbina se encuentra un intercambiador de calor que enfría el aire antes de liberarlo a la atmosfera y un silenciador.

Lado de la compresor: En la toma de aire hay instalado una filtro de aire para evitar que el polvo u objetos extraños entren en el sistema y puedan dañar al compresor. Aguas abajo del compresor hay una válvula de contrapresión con el fin de controlar la carga del compresor, simulando lo que serían las válvulas y cilindros de un motor. Antes de liberar el aire a la atmosfera, pasa por un decantador de aceite y un silenciador.

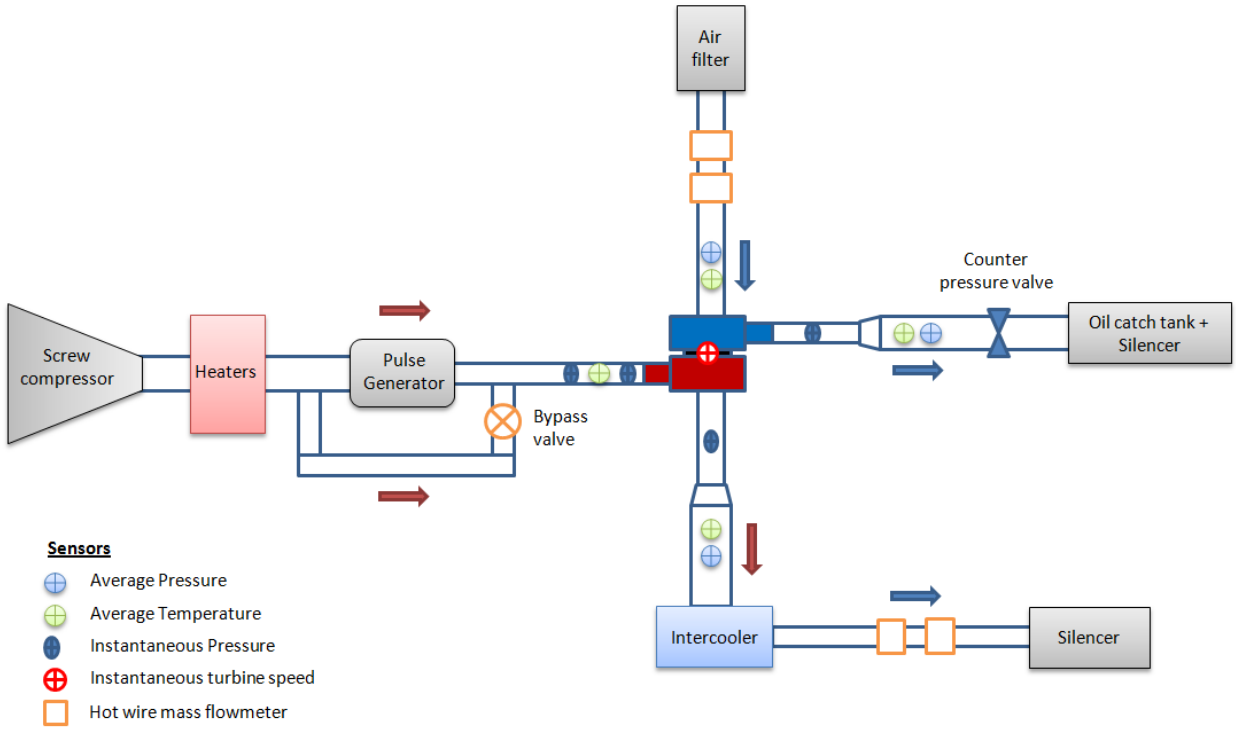

Figura 1. Vista esquemática del banco de ensayo de turbogrupos

Con el fin de registrar las mediciones en los ensayos, se utilizan los siguientes sensores:

Sensores de presión instantánea: Se utilizan para registrar las fluctuaciones instantáneas de presión estática en el flujo generadas por la válvula rotativa. Se instalan cuatro sensores KISTLER piezoresistivos con un rango de medición de 0-5 bar, dos a la entrada de la turbina, uno a la salida de la turbina y otro en la salida del compresor.

Sensores de presión media: Se emplean para registrar la presión estática media del flujo. Se instalan seis sensores KISTLER con un rango de medición de 0-5 bar; dos en la entrada del compresor, dos en la salida del compresor y dos en la salida de la turbina.

Sensores de temperatura: Para medir la temperatura del flujo, se emplean termopares del tipo K. Se instalan 16 termopares; cuatro en cada entrada y salida del turbogrupo. La instalación de los termopares se realice de acuerdo a los estándares de ensayos de turbomáquinas dictados por la SAE J1723 como se muestra en la Figura 2. Se utilizan cuatro termopares por cada tubo de aire: dos termopares a 1/3 del diámetro, un termopar a 1/4 del diámetro y un termopar a 1/2 del diámetro.

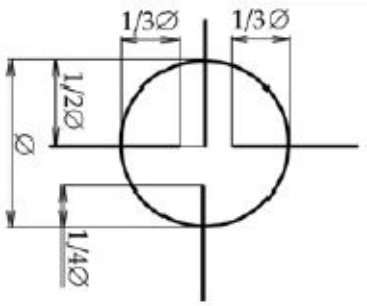

Figura 2. Posicionamiento de los sensores de temperatura según la norma SAE J1723

Caudalimetros: Para registrar el caudal de aire se utilizan los caudalimetros de hilo caliente Siemens VDO. También se instalan de acuerdo a la norma SAE J1723 como se puede observar en la Figura 3. Su rango de medición es de 0 – 720 kg/s y son instalados en parejas a la entrada del compresor y salida de la turbine. Los caudalimetros de la turbina se instalan después del intercambiador de calor ya que su temperatura de máxima de operación es de unos 50ºC.

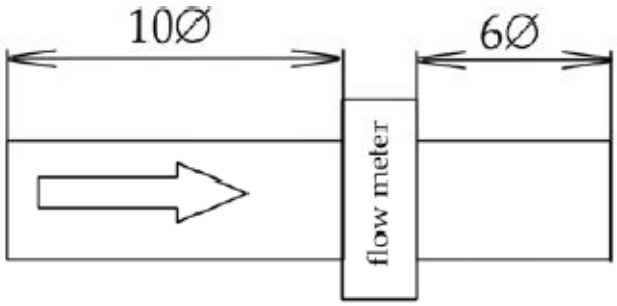

Figura 3. Posicionamiento de los sensores de caudal según la norma SAE J1723

Sensor de régimen: Un sensor PICOTURN con un rango de operación de 0 – 300000 rpm es utilizado para registrar el régimen de giro del turbogrupo.

El sistema de lubricación utilizado en el banco de ensayos se puede observar en la Figura 4. Tanto la presión del aceite como su temperatura y gasto másico se puede controlar y registrar. El sistema de lubricación tiene las siguientes características:

- Caudal máximo de aceite: 80 l/h
- Presión máxima de trabajo: 6 bars
- Temperatura máxima de aceite: 150ºC
- Temperatura mínima de aceite: 25ºC

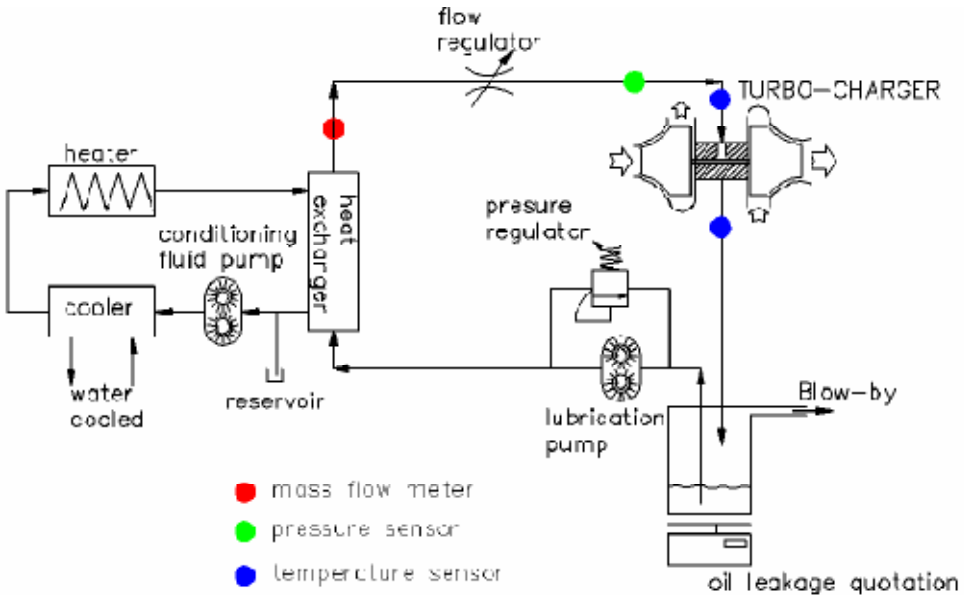

Figura 4. Sistema de lubricación

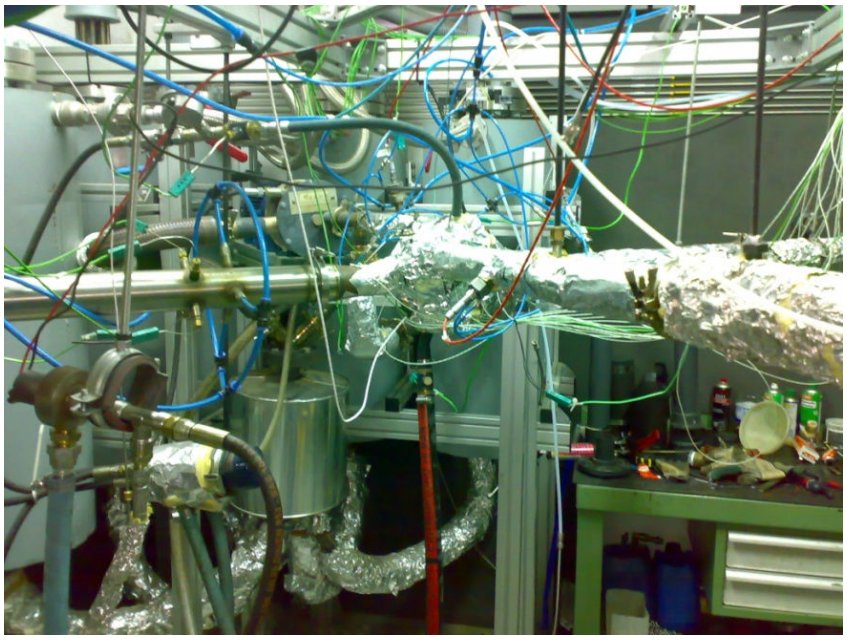

Figura 5. Foto del banco de ensayos experimental de turbogrupos

2.2. Válvula rotativa

Para generar el flujo pulsante necesario para realizar los experimentos, se utilizó una válvula rotativa construida íntegramente por CMT-Motores Térmicos. La válvula está controlada por un motor eléctrico y para que soporte las altas temperaturas del fluido, se ha utilizado el cuerpo central (*housing*) y el eje de un turbogrupo, en vez de rodamientos de bolas convencionales, ya que estos no soportan temperaturas superiores a 150ºC. Con esta configuración, la válvula rotativa es capaz de operar a temperaturas superiores de 600ºC. Para lubricar la válvula se utiliza una derivación del mismo sistema de lubricación principal del banco de ensayos.

La Figura 6 muestra la válvula rotativa instalada en el banco de turbos.

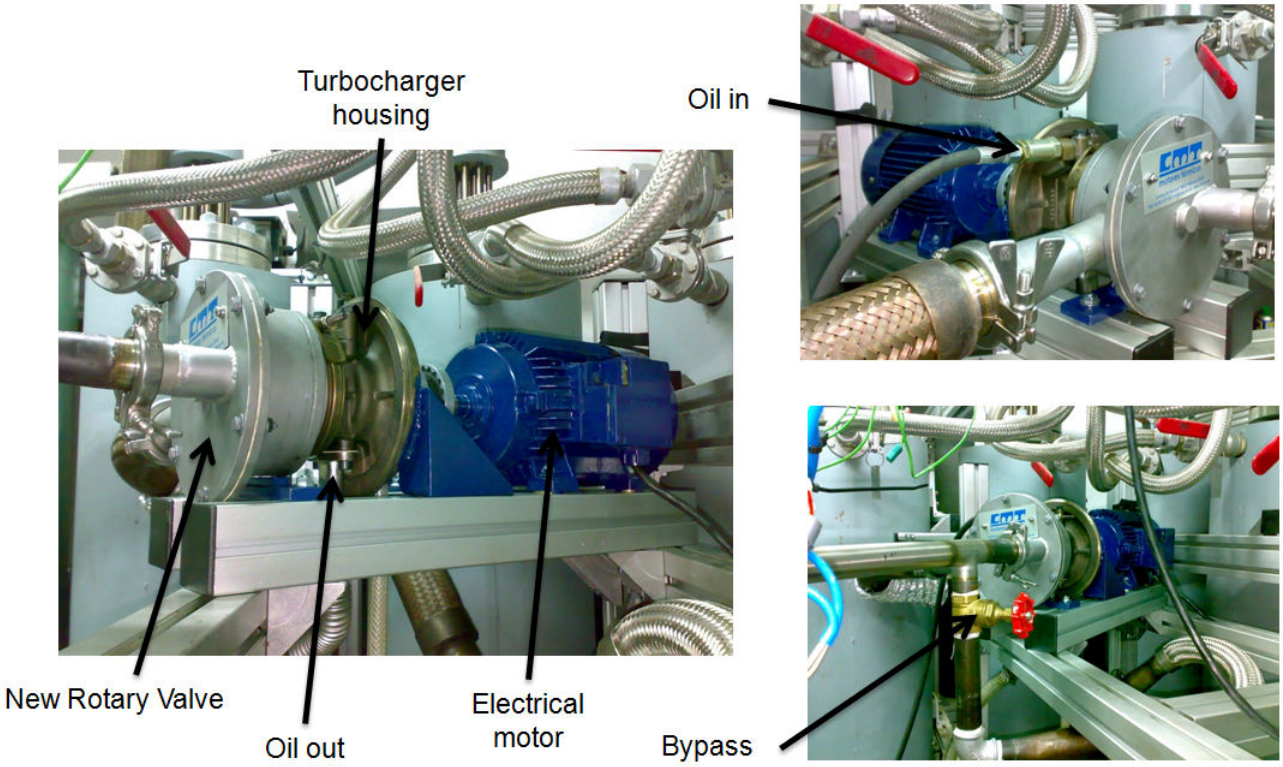

Figura 6. Imágenes del montaje de la válvula rotativa

La válvula rotativa es capaz de poder alterar los siguientes parámetros de forma independientemente entre ellos:

Frecuencia de pulsación: Cambiando el régimen de giro de la válvula rotativa se puede cambiar la frecuencia de los pulsos. Como la válvula está controlada por un motor eléctrico, cambiar el régimen de giro es muy sencillo. El rango de frecuencias que es capaz de generar es de 0 Hz a 150 Hz, lo que implica que es capaz de simular motores de 4 cilindros hasta 4500rpm, motores de 3 cilindros hasta 6000rpm y de 2 cilindros hasta 9000 rpm.

Forma de los pulsos: Para que la forma de los pulsos se asemeje lo máximo posible a los pulsos de escape de un motor reciproco, los discos de la válvula rotativa se pueden intercambiar, de tal forma que al cambiar su forma, se obtienen formas de pulsos diferentes. Actualmente existen tres tipos de discos diferentes (Figura 7) que se pueden intercambiar fácilmente, pero si se desea otra forma de pulso, se pueden fabricar más discos.

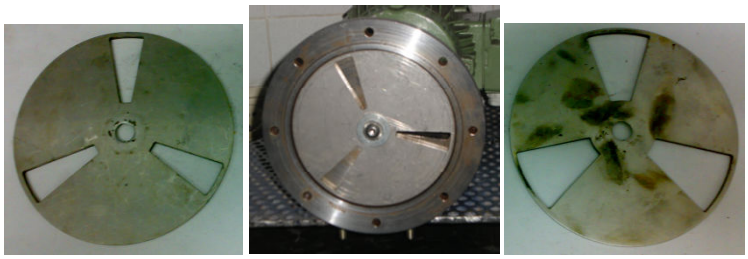

Figura 7. Imágenes de los discos de la válvula rotativa con diferentes aperturas

Amplitud de los pulsos: La amplitud de los pulsos de presión se puede modificar utilizando una derivación controlada por una válvula (Figura 8). De esta forma se puede controlar la cantidad de flujo que pasa a través de la válvula y asi variar la amplitud de los pulsos. Se pueden conseguir pulsos de alrededor de 1 bar, pero depende en gran parte de la presión a la entrada y del gasto másico del flujo, que viene fijadas por las condiciones del ensayo.

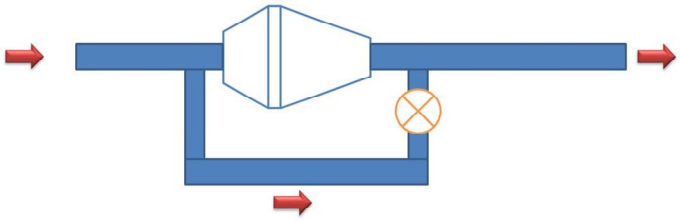

Figura 8. Diagrama de la derivación de la válvula para el control de la amplitud

Un ejemplo de los pulsos que es capaz de generar la válvula rotativa pueden observarse en el Anexo I, diapositiva 27.

3. METODOLOGÍA

Le metodología implementada fue realizar experimentos bajo flujo pulsante en el banco de ensayos tanto con condiciones adiabáticas en la turbina como en condiciones no-adiabáticas. Los experimentos se llevaron a cabo con flujo continuo en el lado del compresor para aislar los fenómenos.

3.1. Campaña de ensayos

3.1.1. Ensayos adiabáticos

Para evitar los efectos de la transferencia de calor en el rendimiento de la turbogrupo, una serie de ensayos adiabáticos fueron llevados a cabo. De experimentos y proyectos anteriores [13], es sabido que para minimizar los flujos de calor entre la turbina y el compresor, la temperatura a la entrada de la turbina tiene que ser igual a la temperatura a la salida del compresor e igual a la temperatura de entra del aceite. Además de mantener estas temperaturas constante a la hora de realizar los ensayos adiabáticos, el turbogrupo también fue aislado apropiadamente para evitar la transferencia de calor con los alrededores.

Gracias a la versatilidad del banco de ensayos y la válvula rotativa, se decidió simular motores con diferentes números de cilindros y diferentes regímenes de giro para estudiar cómo afectan los pulsos de escape en el rendimiento de la turbina. Se simularon motores con dos, tres y cuatro cilindros a bajas velocidades (1000 y 1250 rpm), a velocidades medias (1500 y 2000 rpm) y a velocidades altas (3500 y 4000 rpm). También se ensayaron tres diferentes aperturas de la TGV. La Tabla 1 resume las diferentes configuraciones y frecuencias ensayadas.

	2 Cyl		3 Cyl		4 Cyl		
	F_6	F_5	F_4	F_3	F_2	F_1	
VGT	**1000**	**1250**	**1000**	**1250**	**1000**	**1250**	RPM
0%	16.67	20.83	25.00	31.25	33.33	41.67	Hz
VGT	**1500**	**2000**	**1500**	**2000**	**1500**	**2000**	RPM
50%	25.00	33.33	37.50	50.00		66.67	Hz
VGT	**3500**	**4000**	**3500**	**4000**	**3500**	**4000**	RPM
100%	58.33	66.67	87.50	100.00	116.67	133.33	Hz

Tabla 1. Resumen de las frecuencias y aperturas de la TGV ensayadas

Para similar cargas de motor y puntos de operación diferente, para cada frecuencia seleccionada, se ensayaron tres amplitudes de pulso diferentes. De esta manera se obtiene una gran matriz de puntos que cubre gran parte de los puntos de operación reales de un motor. La Tabla 2 muestra las amplitudes ensayadas.

Amplitude	VGT 0%	VGT 50%	VGT 100%
A1	0.40 bar	0.50 bar	0.50 bar
A2	0.25 bar	0.30 bar	0.35 bar
A3	0.15 bar	0.15 bar	0.25 bar

Tabla 2. Resumen de las amplitudes ensayadas en condiciones adiabáticas

Para cada apertura de TGV, se seleccionaron cinco puntos de operación de la turbina distintos pero al mismo régimen corregido, lo cual permite construir una línea de iso-régimen para cada apertura de TGV. Ensayos de frecuencia y amplitud fueron realizados para cada punto ensayado, lo cual permite construir mapas de rendimiento de turbina frente a relación cinemática. Cada línea de iso-régimen corregido en la turbina pertenece también a una línea de iso-régimen corregido del compresor, por lo que los cinco puntos seleccionados de la línea para realizar los ensayos fueron distribuidos equitativamente desde bombeo a choque en el compresor. Además, por cada punto ensayado, se llevaron a cabo dos ensayos a flujo continuo, que luego se usarían como el rendimiento base para hacer comparaciones. Cada uno de estos ensayos con flujo estacionario se realizaba para cada punto al principio y al finalizar los ensayos con flujo pulsante. Luego se sacaba la media de los estacionarios para reducir la incertidumbre y ser más precisos. En la Figura 9 se puede observar el procedimiento de ensayos gráficamente.

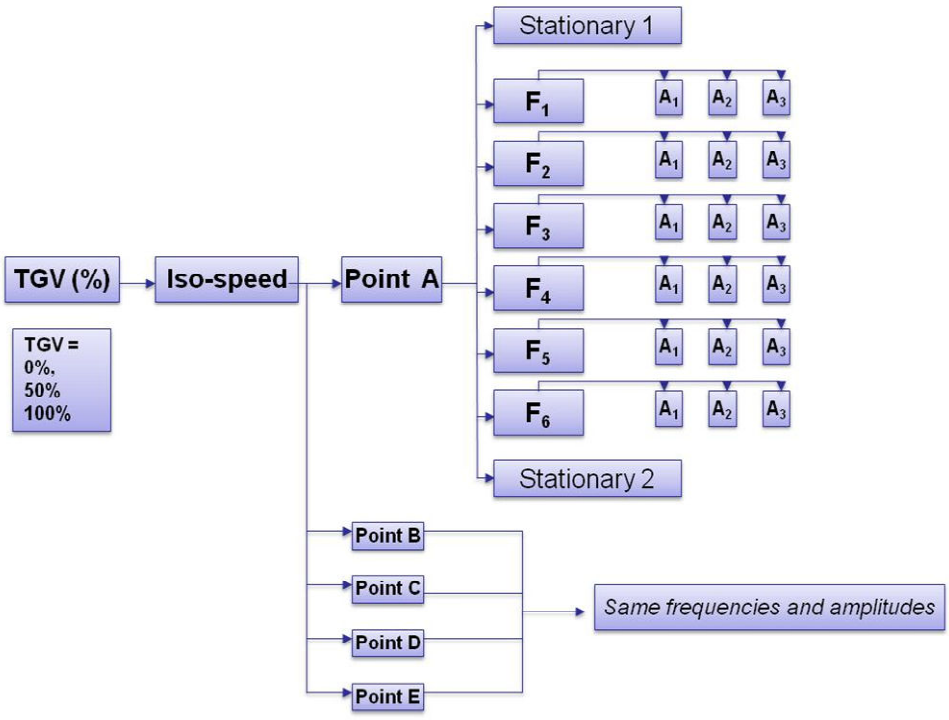

Figura 9. Esquema del procedimiento de ensayos adiabaticos

3.1.2. Ensayos no-adiabáticos

Los ensayos no-adiabáticos se realizaron para estudiar cómo afectan los pulsos al rendimiento de la turbina a alta temperatura. En este caso, aparte de aislar la turbina adecuadamente también se instalaron termopares de pared, tanto en la carcasa del compresor, cuerpo central y carcasa de la turbina para poder medir la transferencia de calor y las pérdidas. El mismo procedimiento seguido con los ensayos adiabáticos fue llevado a cabo, pero en este caso el número de puntos ensayados fue reducido. La Figura 10 muestra el esquema del procedimiento de ensayos para este caso.

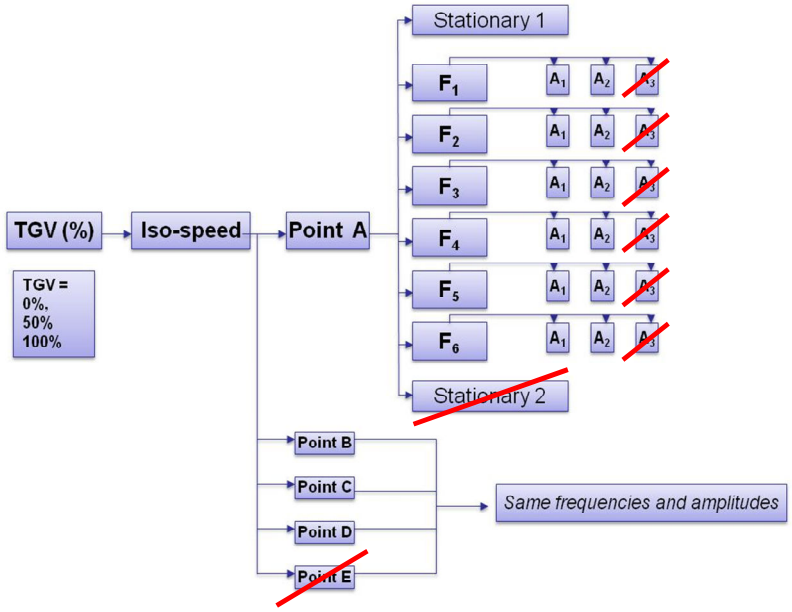

Figura 10. Esquema del procedimiento de ensayos no-adiabáticos

Aunque las frecuencias y aperturas de TGV fueron las mismas que las mostradas en la Tabla 1, las amplitudes fueron también distintas. Las amplitudes utilizadas para los ensayos no-adiabáticos fueron las mostradas en la Tabla 3.

Amplitude	VGT 0%	VGT 50%	VGT 100%
A1	0.50 bar	0.60 bar	0.80 bar
A2	0.30 bar	0.30 bar	0.40 bar

Tabla 3. Resumen de las amplitudes ensayadas en condiciones no-adiabáticas

3.2. Procedimiento de ensayos

3.2.1. Ensayos adiabáticos

Una vez fijada la posición de la apertura de la TGV, cinco puntos de operación eran elegidos, los cuales estaban distribuidos equitativamente entre los límites de bombeo y choque del compresor. Para seleccionar la temperatura de entrada de la turbina y del aceite, se utiliza el promedio de la temperatura de salida del compresor entre choque y bombeo. Esto por lo tanto convierte a los ensayos en "quasi-adiabáticos", ya que la temperatura de salida del compresor varía dependiendo del punto de operación y dicha temperatura no puede ser controlada. Este método se consideró aceptable, ya que si por cada punto ensayado había que cambiar la temperatura de entrada de la turbina, hubiera complicado el proceso de obtención de una línea de iso-régimen corregido en la turbina, ya que habría que haber ido cambiando no solo la temperatura sino los gastos másicos y regímenes de giro.

Al mismo tiempo, el hecho de seleccionar los puntos en el compresor desde bombeo hasta choque, daba la oportunidad de probar cual era la máxima amplitud de pulsos alcanzable, ya que hay que recordar que dicha amplitud depende en gran parte del gasto másico y la presión de entrada y solo se puede determinar haciendo pruebas. Una vez se conseguía la máxima amplitud alcanzable, se utilizaba el siguiente algoritmo para determinar las siguientes amplitudes:

- Amplitud 1 = Amplitud máxima
- Amplitud 2 ~ Amp1 / 2
- Amplitud 3 ~ Amp2 / 2

Cuando se llevaron a cabo los experimentos, se dio el caso que cuando se cambiaba la frecuencia y amplitud para cada punto, la relación de expansión y gasto másico en la turbina cambiaban. Esto implicaba que el punto de operación cambiaba, pero para hacer los puntos comparables entre los ensayos estacionarios y los ensayos con flujo pulsante había que mantener el mismo punto. Por simplicidad, esto se hizo manteniendo el punto de operación fijo en el compresor. El efecto de hacer esto se puede observar claramente en las Figura 11 y Figura 12, donde todos los puntos de los ensayos adiabáticos (en azul) han sido graficados. Como se puede ver, todos los puntos en el compresor caen uno encima del otro, mientras que en la turbina hay una nube de puntos. Esto claramente demuestra que los pulsos están afectando al rendimiento de la turbina, ya que para mantener el mismo punto de operación en el compresor se necesita un nivel de energía diferente en la turbina.

3.2.2. Ensayos no-adiabáticos

En este caso, la temperatura a la salida del compresor no era un problema ya que la temperatura la entrada de la turbina siempre iba a ser muy superior. El mismo procedimiento que en los ensayos adiabáticos fue establecido, pero en este caso en las pruebas iniciales para determinar los puntos de operación entre choque y bombeo del compresor, no solo se comprobaba la máxima amplitud alcanzable sino también la máxima temperatura del flujo alcanzable. Esto es debido a la configuración del banco de ensayos, ya que la máxima temperatura que se puede

obtener depende también en gran parte del gasto máxima y de la presión del fluido, ya que no solo contribuyen las resistencias eléctricas en calentar el fluido, sino que el compresor de tornillo que suministra el caudal de aire también ayuda en el proceso de calentamiento del aire. Por lo tanto, aunque el banco está diseño para alcanzar temperaturas de hasta 400ºC, cuando se opera con bajos caudales, esa temperatura es inalcanzable. Para estos experimentos, la temperatura del aceite se fija a 95ºC y la presión del mismo a 2.2 bares, ya que se considera como la optima para reducir las pérdidas mecánicas.

Una vez se determinan las temperaturas y amplitudes máximas, se sigue el mismo procedimiento que con los ensayos adiabáticos, manteniendo fijo siempre el punto de operación del compresor.

Hay que añadir que para que estos ensayos no-adiabáticos fueran comparables con los ensayados adiabáticos anteriores, se tenía que mantener el mismo régimen corregido de la turbina. Aunque el banco de ensayos tenía la capacidad de mantener el régimen, el incremento de temperatura significaba que los puntos de operación al mismo iso-régimen sobrepasaban la línea máxima de operación del motor. Es decir, que se obtenían unas relaciones de expansión muy altas, a las que un motor en operación normal nunca sería capaz de alcanzar. Esto se puede observar en el Anexo I, diapositiva 23. Por lo tanto, como una turbina acoplada a un motor nunca operaría en estos puntos, se decidió mantener el mismo régimen de giro real del turbogrupo en vez del régimen de giro corregido de la turbina.

3.3. Puntos ensayados

Ensayos adiabáticos:

		Compressor			Turbine		Oil
VGT opening	Turbocharger Speed (rpm)	Corrected Speed (rpm)	Choke temp (ºC)	Surge temp (ºC)	Corrected speed (rpm)	Inlet temp (ºC)	Inlet temp (ºC)
0	106600	105400	60	74	100400	66	66
50	130000	129900	66	90	119000	82	82
100	121000	119800	66	88	111500	76	76

Tabla 4. Puntos ensayos en los ensayos adiabáticos

Ensayos no-adiabáticos:

		Compressor	Turbine		Oil
VGT opening	Turbocharger Speed (rpm)	Corrected Speed (rpm)	Corrected speed (rpm)	Inlet temp (ºC)	Inlet temp (ºC)
0	106600	106100	73600	360	95
50	130000	129300	87300	390	95
100	121000	120200	80600	400	95

Tabla 5. Puntos ensayos en los ensayos no-adiabáticos

Todos los puntos ensayados representados en los mapas de operación de la turbina y compresor.

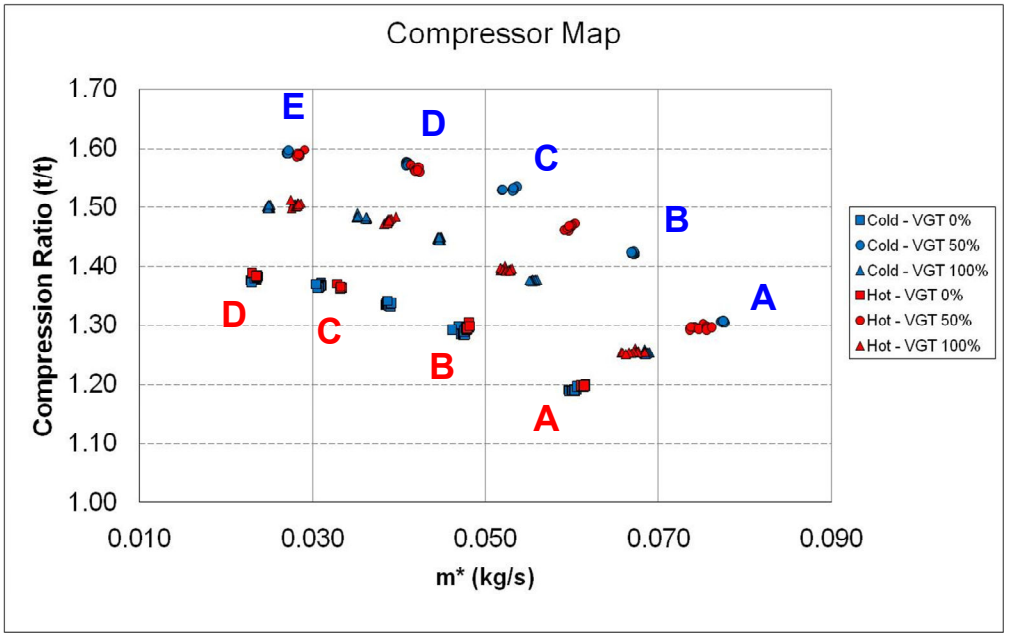

Figura 11. Puntos ensayados mostrados en el mapa del compresor

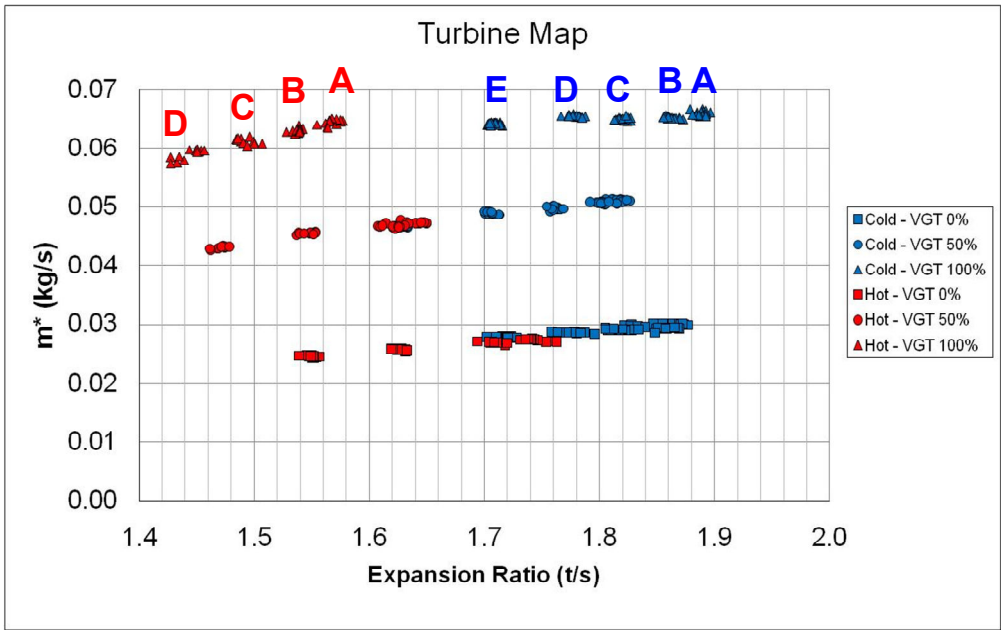

Figura 12. Puntos ensayados mostrados en el mapa de la turbina

Se puede obtener más información sobre los puntos ensayados en el Anexo I, diapositiva 5, 6 y 26.

4. ANÁLISIS DE RESULTADOS EXPERIMENTALES

4.1. Ensayos adiabáticos

Los resultados experimental se pueden agrupar en tres sets diferentes: 1) El efecto de la frecuencia, la amplitud y la apertura de la TGV, 2) el efecto de la distancia entre los puntos ensayados y el máximo rendimiento de la turbina y 3) el efecto del rendimiento mecánico.

4.1.1. Amplitud, frecuencia y apertura de la TGV

El primer análisis de resultados llevado a cabo fue el estudio de cómo afecta al rendimiento de la turbina la frecuencia, la amplitud y la apertura de la posición de la TGV. Inicialmente se realizó un estudio del efecto de la frecuencia por cada apertura de TGV y por número de cilindros independientemente. El problema de agrupar la información de esta manera, es que el efecto real de la frecuencia permanecía oculto detrás del número de cilindros. El problema residía en que las mismas frecuencias aparecían en diferentes configuraciones de regímenes de motor y frecuencias. Por ejemplo:

- 4 cilindros, 1000rpm, TGV 0% = 2 cilindros, 2000rpm, TGV 50% = **33.33Hz**
- 4 cilindros, 2000rpm, TGV 50% = 2 cilindros, 4000rpm, TGV 100% = **66.67Hz**

Por lo tanto, para obtener una visión más clara de cada efecto de forma independiente, todos los resultados fueron agrupados por frecuencias y analizados frente a un término de rendimiento no-dimensional obtenido con respecto al rendimiento de la turbina bajo flujo continuo (Anexo I, diapositiva 7).

Para obtener el rendimiento de la turbina bajo flujo continuo para cada uno de los puntos ensayados, se toma el promedio entre los dos puntos estacionarios medidos para cada punto (del punto A al punto E). Debido al procedimiento utilizado para realizar los ensayos, para cada ensayo de amplitud y frecuencia, el mismo punto de operación en el compresor se mantenía, pero en la turbina variaba ligeramente como se ha explicado anteriormente. Por lo tanto, al obtener la relación cinemática de dichos puntos, los valores variaban ligeramente los unos con los otros (Anexo I, diapositiva 8).

Para facilitar el estudio y comparación del efecto de los pulsos con los puntos estacionarios, era necesario que todos tuvieran la misma relación cinemática, por lo que se decidió extrapolar todos los grupos de puntos con la misma amplitud y frecuencia. Para hacer esto de la forma más precisa, se utilizó el método de extrapolación basado en principios físicos desarrollado en la Sección 5.

Una vez realizadas las extrapolaciones, el rendimiento no-dimensional para cada punto se obtuvo utilizando la siguiente ecuación 1:

$$\Delta\eta = \frac{\eta_i - \eta_{stationary}}{\eta_{stationary}} \quad (1)$$

Donde,

η_i = rendimiento de la turbina para cada punto ensayado

$\eta_{stationary}$ = rendimiento de la turbina para cada punto ensayado estacionario

En el Anexo I, diapositiva 9, se pueden observar los gráficos de frecuencia frente al rendimiento no-dimensional ($\Delta\eta$) separados por amplitud y ordenados por la relación cinemática (puntos A al E). Como se puede observar, hay una clara reducción del rendimiento a medida que disminuye la frecuencia para todos los casos y todos los puntos. Parece ser que hay una frecuencia crítica, alrededor de los 50 Hz, a partir de la cual si se reduce la frecuencia, el rendimiento disminuye considerablemente para todos los casos. En el caso de mayor amplitud, los pulsos parecen que no afectan de ninguna manera al rendimiento de ala turbina, mientras que para la amplitud media y la amplitud baja, se puede observar que el rendimiento en estos casos se reduce alrededor de un -1% y -2%. Además, parece que también existe una tendencia con la relación cinemática, ya que los puntos con mayores relaciones cinemáticas (punto A y B) parecen menos afectados por los pulsos que los puntos con relaciones más bajas (punto D y E). También habría que añadir que hay unos cuantos puntos con rendimientos positivos, lo cual se debe principalmente a la incertidumbre de medida que es alrededor de un 1%.

En el Anexo I, diapositiva 10, se pueden observar gráficas similares pero esta vez los puntos están separados por relación cinemática y ordenados por apertura de la TGV, por lo que se pueden observar una gráfica para cada uno de los puntos ensayados con tendencias similares a las comentadas. En este caso además, el punto E, el que tiene la mayor relación cinemática, muestra una gran dispersión de puntos y una gran reducción del rendimiento, mientras que los puntos A y B, con relaciones cinemáticas más bajas, muestran una mayor resistencia al flujo pulsante, ya que su rendimiento no se ve tan afectado. Además para todos los casos, la apertura de 50% de la TGV parece ser la menos afectada por el efecto de los pulsos que el resto de las aperturas.

Finalmente, otra serie de gráficos pueden ser observados en el Anexo I, diapositiva 11, en la cual los gráficos esta vez están separados por amplitud y ordenados por apertura de la TGV. Una vez más, para todos los casos, la apertura de 50% de la TGV parece mostrar mayor resistencia a los pulsos, ya que es la menos afectada en rendimiento. Además, se ve también de nuevo que para la máxima amplitud, el flujo pulsante parece ser que no tenga ningún efecto sobre el rendimiento de la turbina.

Por lo tanto se puede extraer una tendencia clara de esos resultados y es que existe una frecuencia de pulsos crítica, a partir de la cual si la frecuencia baja, el rendimiento de la turbina se ve fuertemente afectado, mientras que la amplitud parece que juega un papel mucho menos importante. La relación cinemática y la apertura de la TGV también parecen que sean factores importantes, ya que cuando mayor es la relación cinemática, mayor es la reducción de rendimiento,

mientras que la apertura de la TGV del 50% parece ser la más robusta y a la que menos efecto le hace los pulsos.

Esto da que pensar que puede que la distancia entre la relación cinemática del punto ensayado y la relación cinemática en el punto de máximo rendimiento sea un factor importante que explicaría porque los puntos con menores relaciones cinemáticas y puntos con una apertura de TGV del 50% son más robustos.

4.1.2. Distancia del rendimiento máximo

A partir del análisis anterior se genera otro parámetro no-dimensional para investigar el efecto que tiene la distancia entre el punto ensayado y el punto de máximo rendimiento de la turbina. El término se define como se puede observar en la ecuación 2:

$$\Delta\sigma = \frac{\sigma_i - \sigma_{\max}}{\sigma_0 - \sigma_{\max}} \tag{2}$$

Donde,

σ_i = relación cinemática de cada punto ensayado.

σ_0 = relación cinemática a rendimiento cero.

σ_{max} = relación cinemática a rendimiento máximo.

Más detalles de este parámetro se pueden obtener en el Anexo I, diapositiva 12.

Si se gráfica este nuevo término ($\Delta\sigma$) frente al rendimiento no-dimensional ($\Delta\eta$) se obtienen los gráficos mostrados en el Anexo I, diapositiva 14. Los gráficos están separados por rangos de frecuencias y todos los puntos, amplitudes y aperturas de TGV se han graficado juntos. Como se puede observar, hay una clara tendencia decreciente con respecto a $\Delta\sigma$, especialmente en el rango de bajas frecuencias.

Esto significa que cuanto el punto está más cercado al punto de máximo rendimiento, más robusto es y menos afectado se ve por las condiciones de flujo pulsante a la entrada de la turbina. Además, este efecto se ve agravado si la frecuencia de los pulsos se encuentra por debajo de 50Hz, ya que como se puede observar, la tendencia es mucho mas pronuncia para dichos casos comparado con el resto.

Si dibujados el mismo grafico de $\Delta\sigma$ frente a $\Delta\eta$ (Anexo I, diapositiva 15) con todos los puntos ensayos y ordenados por la apertura de le TGV, se puede obtener una explicación de porque los pulsos afectan en menor medida a la apertura del 50%. Como se puede observar en el gráfico, la mayoría de los puntos en la apertura de 50% de la TGV, se corresponden con un $\Delta\sigma$ bajo (es decir, están más cerca del rendimiento máximo), lo cual implica que se ven menos afectados por el flujo pulsante. Además, también se observa que las aperturas de 0% y 100% de la TGV se

corresponden con el mismo rango de $\Delta\sigma$, pero la apertura de 0% se ve más afectada por los pulsos con rendimientos más bajos. Esto se debe principalmente a que las frecuencias ensayadas con la apertura de 0% de la TGV fueron todas por debajo del umbral de 50Hz, mientras que las de la apertura de 100% todas fueran por encima. Esto se puede observar en el Anexo I, diapositiva 16-18. Una vez más se demuestra que la frecuencia de los pulsos juega un papel fundamental.

4.1.3. Rendimiento mecánico

Otro factor importante a tener en cuenta cuando se estudia el efecto del flujo pulsante en turbinas es la influencia del rendimiento mecánico (Anexo I, diapositiva 19). El parámetro usado para definir la diferencia entre el rendimiento mecánico con flujo continuo con el promedio del rendimiento mecánico medida instantáneamente es el siguiente:

$$\Delta\eta_{mech} = \frac{\eta_{mech}^{i} - \eta_{mech}^{stationary}}{\eta_{mech}^{stationary}} \tag{3}$$

Donde,

η^{i}_{mech}= rendimiento mecánico del punto ensayado.

$\eta_{mech}^{stationary}$ = rendimiento mecánico del punto ensayado bajo flujo continuo.

El rendimiento mecánico instantáneo se obtiene utilizando la correlación definida en el Anexo I, diapositiva 20 [14]. Esta correlación es función de la presión del aceite, turbina y compresor, además del número de Prandlt y numero de Reynolds. Como la presión instantánea a la entrada de la turbina era conocida, esto permitió calcular el rendimiento mecánico instantáneo, ya que la presión en el compresor y en el aceite se asumieron como constantes.

Si se grafica el parámetro $\eta_{mech}^{stationary}$ frente a $\Delta\sigma$, se obtiene la gráfica mostrada en el Anexo I, diapositiva 21, donde se muestran todos los puntos ensayados ordenados por apertura de le TGV. Como se puede observar, hay una tendencia claramente decreciente con respecto al rendimiento mecánico a medida que aumenta la distancia del punto de rendimiento máximo ($\Delta\sigma$).

4.2. Ensayos no-adiabáticos

El mismo procedimiento de análisis utilizado con los ensayos adiabáticos fue llevado a cabo. Para hacer los resultados comparables entre los ensayos pulsantes y los ensayos con flujo continuo, se utilizó de nuevo la técnica desarrollada para extrapolar mapas, descrita en la sección 5, lo cual permite obtener el rendimiento de los puntos ensayados para la misma relación cinemática. Después de realizar esta operación, los resultados obtenidos para todas las frecuencias se graficaron frente al rendimiento no-dimensional de la misma forma que se hizo con

los ensayos adiabáticos. Dichos gráficos pueden ser encontrados en el Anexo I, diapositiva 31, donde los puntos han sido separados por amplitudes y ordenados por apertura de TGV.

A diferencia de los ensayos adiabáticos, esta vez no se puede observar ninguna tendencia clara del efecto que provoca el flujo caliente y pulsante en el rendimiento de la turbina. Todos los resultados, incluso para los de mínima y máxima amplitud, parecen oscilar entre un rendimiento de +4% y -4% sin ninguna tendencia clara. Esta vez la apertura de la TGV, ni tan siquiera la amplitud parece que tengan ningún efecto claro.

En el Anexo I, diapositiva 32, se pueden observar las mismas gráficas pero esta vez los puntos han sido ordenados por las diferentes relaciones cinemáticas (punto A a E). Una vez más, no se puede observar ninguna tendencia clara. Todos los puntos oscilan alrededor de un rendimiento de +2% y -2% y parece que la ni la frecuencia, ni la amplitud ni la distancia al máxima rendimiento parece influir.

En dichos gráficos aparecen unos puntos que parecen siempre salirse de la tendencia. Esto como se puede observar en la figura del Anexo I, diapositiva 30, se debe a un error en la medición de los ensayos con flujo continuo, lo que provoca que cuando se comparan los ensayos bajo flujo pulsantes con estos, se observe una discrepancia con el resto de puntos.

Una explicación simple de porque no aparece ninguna tendencia bajo condiciones flujo pulsante caliente, se pude obtener si nos fijamos en las figuras que podemos encontrar en el Anexo I, diapositiva 28-30, donde se pueden observar los gráficos de rendimiento frente a relación cinemática extrapolados para todos los puntos ensayados. Se puede ver claramente que, esta vez, todos los puntos ensayados están muy cerca o encima del área de máximo rendimiento de la turbina. Si recordamos lo visto anteriormente con los ensayos adiabáticos, cuando más cerca están los puntos del punto de máximo rendimiento, menos influencia tienen los pulsos en el rendimiento de la turbina, por lo que esto podría ser una explicación de porque no se ve ninguna tendencia.

La transferencia de calor probablemente es la que mayor influencia tiene en estos resultados, ocultando el efecto del flujo pulsante, pero se necesita un análisis más profundo junto con la realización de un buen modelo unidimensional, el cual debe de incluir un modelo de transferencia de calor.

5. EXTRAPOLACIÓN DE MAPAS

Para poder operar y simular el comportamiento de una turbina y un turbogrupo en un código fluido dinámico unidimensional, se requiere disponer de mapas de turbina completos, tanto de gasto másico, como de relación de expansión y de rendimiento. Es por ello que se necesita desarrollar un modelo de extrapolación de mapas basado en la física de la turbina, ya que debido a los límites de bombeo y choque del compresor, solo se pueden obtener muy pocos puntos de operación experimentales de una turbina.

5.1. Extrapolación del mapa de gasto másico

Para realizar la extrapolación del mapa de gasto másico frente a relación de expansión, se propone utilizar un método de extrapolación basado en la ecuación de la tobera (ecuación 4).

$$\dot{m}^* = A_{eff}\gamma\left(\frac{1}{ER}\right)^{\frac{1}{\gamma}}\sqrt{\frac{2}{\gamma-1}\left[1-\left(\frac{1}{ER}\right)^{\frac{\gamma-1}{\gamma}}\right]} \tag{4}$$

Las diferentes etapas de la turbina se idealizan como una única tobera y un ajuste de esta ecuación con los datos experimentales es llevado a cabo para obtener una estimación de la variación del área efectiva de la tobera frente a los diferentes valores de relación de expansión. Además, gracias a esta ecuación, se puede extrapolar el gasto másico hasta cualquier valor de relación de expansión. El comportamiento físico, junto con la explicación y la validación del método con diferentes turbinas se puede encontrar en la sección 2 del Anexo III.

5.2. Extrapolación del mapa de rendimiento

El método propuesto para extrapolar la curva de rendimiento se basa en una ecuación desarrollada de principios físicos la cual toma en cuenta la definición de rendimiento total a estático, los triángulos de velocidad para cada etapa y el comportamiento termodinámico del fluido. Es de interés que esta ecuación sea función de la relación cinemática y de valores intrínsecos relacionados con mecanismos de pérdidas, datos geométricos y propiedades del gas, para que la turbina pueda ser correctamente caracterizada y se pueda obtener extrapolación apropiada. Los detalles de cómo se obtiene la derivación de la ecuación de rendimiento desde principios básicos se puede encontrar en la sección 3 del Anexo III.

Dependiendo de las condiciones del fluido o del tipo de ensayo, se obtienen tres regresiones diferentes. La ecuación 5 se utiliza cuando los ensayos se han realizado a iso relaciones de expansión, mientras que la ecuación 6 se utiliza cuando los ensayos han sido realizados a iso regímenes de giro corregidos. La ecuación 7 solo es válida en condiciones de flujo chocado. La descripción de cada constante física (K_1, K_2, K_2* y K_3) se puede observar en la sección 3 del Anexo III.

$$\eta_{ts} = -K_1 \upsilon^2 + K_2 \upsilon \frac{A_{eff}}{A_0} \left(\frac{1}{ER} \right)^{\frac{1}{\gamma}} \tag{5}$$

$$\eta_{TS} = -K_1 \upsilon^2 + K_2^* \left[1 - \frac{K_3}{\upsilon^2} \right]^{\frac{1}{\gamma - 1}} \upsilon \tag{6}$$

$$\left(\eta_{ts} \right)_c = -K_1 \upsilon^2 + K_2 \upsilon^2 \frac{\dot{m}_c^*}{U_1^*} \frac{R}{A_0} = \upsilon^2 \left(K_2 \frac{\dot{m}_c^*}{U_1^*} \frac{R}{A_0} - K_1 \right) \tag{7}$$

5.3. Validación y resultados

Las ecuaciones y los métodos de extrapolación propuestos se ha validado utilizando datos de cinco turbinas de sobrealimentación: una turbina de un motor de coche convencional, un set de tres turbinas de camión compuestas por una grande, una media y una pequeña, y una turbina comercial utilizada para la generación de energía. Los detalles y los gráficos de validación de los resultados se pueden observar en la sección 4 del Anexo III.

Como se puede observar en los gráficos, se ha obtenido una buena correlación en la predicción del modelo y los resultados experimentales, obtenidos de varias fuentes y diferentes bancos de ensayos. El modelo permite extrapolar con exactitud los principales parámetros de la turbina: el gasto másico y el rendimiento isentrópico.

Además de la validación del modelo con los puntos experimentales, el resto de variables de las que se compone el modelo también han sido validadas. Dichas variables se componen de datos geométricos de la turbina, ángulos y propiedades del gas y como se puede observar en la sección 4 del Anexo III, los valores obtenidos son consistentes con los valores reales.

La metodología presentada para la extrapolación de mapas de la turbina ha sido publicada en dos artículos científicos que pueden encontrarse en el Anexo II y Anexo III. El artículo presentado en el Anexo II ha sido publicado en el *SAE 2010 World Congress* con referencia 2010-01-1234 y DOI 10.4271/2010-01-1234. El artículo presentado en el Anexo III ha sido enviado a la revista *Energy Conversion and Management* y está pendiente de publicación.

6. CONTROL ACTIVO EN TURBINAS

El estudio del flujo pulsante no solo sirve para ver los efectos que provoca sobre el rendimiento de una turbina, sino que también permite mejorar y desarrollar nuevos sistemas de acoplamiento motor-turbina, para intentar mejorar el aprovechamiento de energía contenida en los gases de escape. El concepto bajo investigación es el control activo en turbinas (ACT) el cual ha sido demostrado muy prometedor en los bancos de ensayo, pero no ha sido probado en combinación con un motor de automoción. Se propone realizar un ensayo numérico para ver si los beneficios obtenidos en el rendimiento de la turbina también se trasladan al rendimiento global de un motor, los cuales son muy dependientes del efecto pulsante en el escape, ya que dichos pulsos ayudan a extraer los gases de la cámara de combustión.

6.1. El concepto ACT

El concepto de control activo en una turbina es una evolución de las actuales turbinas de geometría variables (TGV). La principal diferencia consiste en el hecho de que las TGV solo responden a cambios de punto de operación del motor, mientras que el nuevo concepto de turbina ACT no solo responde a dichos cambios sino que también es capaz de responder a los pulsos de presión de los gases de escape cuando el motor opera en un punto fijo de operación.

Las turbinas con control activo son capaces de alterar en cada instante de tiempo la apertura de los alabes directores, de tal forma que el área efectiva de entrada cambia instantáneamente adaptándose a los pulsos de los gases de escape. De esta forma se consigue extraer la máxima energía del fluido.

Existen numerosos experimentos realizados en esta técnica de control y los beneficios pueden ser cuantificados, pero dicha ganancia tiene un coste ya que el mecanismo de control rápido requerido es muy complejo.

6.2. Modelo unidimensional: OpenWAM

Como se puede observar en el apartado 4 del Anexo IV, el código unidimensional que se va a utilizar para realizar el estudio del efecto de una turbina de control activo acoplada a un motor de combustión interna, es un modelo de acción de ondas conocido como OpenWAM, el cual ha sido desarrollado íntegramente por CMT-Motores Térmicos [15]. Este modelo calcula el comportamiento del motor de combustión interna y del turbogrupo mediante ecuaciones no estacionaras de masa momento y energía y las resuelve por el método elementos finitos [16].

El modelo de la turbina implementado en el OpenWAM se basa en la representación de una turbina con dos toberas ideales descargando a un volumen intermedio. La primera tobera representa el estator de la turbina mientras que la segunda representa el rotor. El volumen intermedio sirve para poder simular la acumulación de masa que ocurre bajo condiciones

transitorias, que en este caso serían las producidas por el flujo pulsante. El modelo es capaz de calcular la caída de presión producida por el estator y el rotor utilizando la curva de rendimiento de la turbina. Con este salto de presión es capaz de calcular las áreas efectivas equivalentes a las toberas que representan el estator y rotor de la turbina. Por tanto, aquí reside la necesidad de tener los mapas completos de rendimiento de la turbina, ya que son requeridos por el modelo para poder calcular el resto de parámetros.

6.3. Calibración del modelo

La calibración del modelo es el aspecto más importante y necesario a la hora de tratar con modelos computacionales. Debido a la complejidad de los sistemas simulados, siempre se incluyen simplificaciones lo cual hace que los resultados puedan incluir errores inducidos por dichas simplificaciones. Aunque el código de OpenWAM es muy fiable y robusto, se requieren factores de corrección para hacer coincidir los valores del modelo con los valores reales.

Para la realización de estos experimentos se ha utilizado un motor de cuatro tiempos convencional de automoción, ya que se disponían previamente de los resultados experimentales. En el apartado 5 del Anexo IV se pueden ver las características de dicho motor y los resultados de los ajustes. Como se puede observar, todos los valores medios modelados tienen un error de ±5% con respecto a los valores medidos, mientras que los valores instantáneos más importantes mostraban un error de ±0.2 bar, lo cual se considera aceptable.

6.4. Ensayos con control activo

Los resultados de los ensayos numéricos realizados con control activo se pueden observar en el apartado 6 del Anexo IV. Se implementó una curva sinusoidal en el código para controlar la apertura de los alabes de la TGV, la cual se sincronizó con los pulsos de escape del motor para de esta forma obtener los máximos beneficios. La TGV se abría en los picos de los pulsos y se cerraba en los valles.

Para poder comparar entre la mejora de rendimiento producido por el control activo y el rendimiento base del motor, el promedio de apertura de la TGV y el dosado se tenía que mantener constante. Mantener el promedio de apertura de la TGV implica que el punto de operación de la turbina y del motor no cambia. Por tanto, si el rendimiento de la turbina cambia, esto se traslada a un aumento de gasto másico de aire, por lo que se aumenta el combustible para mantener el dosado constante y seguir obteniendo resultados comparables.

Como se puede ver en el apartado 6 del Anexo IV, se realizan varios estudios con diferentes amplitudes y diferentes formas de curvas sinusoidales, pero los resultados obtenidos son muy pobres. La teoría detrás del concepto es muy prometedora, pero cuando se monta la turbina en un motor, el motor es el que dicta el punto de funcionamiento de la turbina, lo cual limita en gran parte las posibilidades que tiene el ACT. Como se puede observar en los mapas de rendimiento frente a

desplazamiento de la TGV, toda la mejora conseguida se pierde al tener que compensar para mantener el punto de funcionamiento.

La ganancia máxima de rendimiento de la turbina ha sido de 0.15%, mientras que en la mayoría de los casos ha sido negativa. Estos cambios de rendimiento apenas han repercutido en el rendimiento global del motor.

El estudio numérico presentado sobre las turbinas con control activo ha sido enviado a la revista *International Journal of Automotive Technology (IJAT)* y está pendiente de publicación. Dicho artículo puede encontrarse en el Anexo IV.

7. ESTUDIO DE CODOS EN EL COMPRESOR

Además de los estudios experimentales y numéricos realizados con flujo pulsante en la turbina del turbogrupo, también ha realizado un pequeño estudio sobre el efecto que tiene sobre el rendimiento del compresor la instalación de codos de 90º a la entrada del mismo.

Este estudio responde a las dificultades encontradas hoy en día en la instalación de turbogrupos en motores de vehículos de automoción, ya que el espacio disponible cada vez es menor debido a la cantidad de dispositivos y accesorios que llevan en la actualidad los motores. Se considera por tanto necesario el estudio del efecto que tiene la instalación de codos a la entrada del compresor y los cambios abruptos de dirección del fluido en el rendimiento del compresor.

La metodología seguida para dicho estudio consiste en comparar el efecto que tienen diferentes tipologías de codos de 90º (apartado 2, Anexo V) frente a la configuración sin codo ideal, para poder cuantificar los efectos y poder obtener la mejor configuración posible de codo.

Se empieza estudiando diferentes geometrías de codos en CFD para obtener las mejores configuraciones como se puede observar en el apartado 3 del Anexo V. Una vez realizado el estudio numérico se fabrican los codos para ser ensayos tanto en el banco de flujo continuo como en el banco de turbos. Los ensayos en el banco de flujo continuo sirven para estudiar la caída de presión producida por los codos. En el apartado 4 del Anexo V, se puede encontrar la descripción del banco y la metodología seguida para realizar el estudio. Posteriormente los codos se instalan en el banco de turbos, justo en la entrada del compresor, donde se ensayan bajo condiciones de flujo continuo y caliente. La descripción del banco y la metodología seguida se puede encontrar en el apartado 5 del Anexo V.

Después de analizar los resultados obtenidos, los cuales se pueden encontrar en el apartado 6 del Anexo V, es posible observar que en la mayoría de los casos los codos producen un efecto negativo en la relación de compresión, que se tiende a reducir especialmente a altas velocidades del rotor y altos gastos másicos del flujo. En cambio, los efectos en la línea de bombeo del compresor parecen ser positivos, ya que para la mayoría de los casos, la línea de bombeo se ve desplazada hacia la izquierda del mapa, aunque por desgracia lo mismo le ocurre a la línea de choque, lo cual reduce el máximo gasto de aire que el compresor es capaz de trasegar.

Del estudio teórico y experimental se puede concluir que los fenómenos que mayor efecto tienen sobre el rendimiento del compresor son el índice de uniformidad del fluido y la pérdida de presión causada por el codo. En el apartado 8 del Anexo V, se puede encontrar la geometría del codo que ha dado los mejores resultados en los experimentos.

El estudio experimental presentado sobre el efecto que tiene la instalación de codos de 90º sobre el rendimiento del compresor, está pendiente de ser publicado en una revista científica y puede encontrarse en el Anexo V.

8. CONCLUSIÓN

Del estudio realizado se puede concluir que el flujo pulsante a la entrada de la turbina sí que provoca un efecto negativo en su rendimiento como era de esperar inicialmente, ya que la turbina se trata de una máquina centrifuga mientras que el motor al cual va acoplado es una máquina reciproca alternativa, con lo que la unión no es la óptima.

Después de realizar el estudio experimental sobre el efecto de los pulsos se obtiene que hay dos parámetros principales que afectan al rendimiento: la frecuencia de los pulsos y la distancia del punto de operación al punto de máximo rendimiento. Se han desarrollado parámetros no-dimensionales para estudiar su efecto. La frecuencia parece tener un efecto muy negativo sobre la turbina si es inferior a 50Hz, ya que si la frecuencia baja de este umbral, el rendimiento decae rápidamente a medida que disminuye la frecuencia. En cambio, por encima de esta frecuencia, el rendimiento baja un 1-2% sobre el rendimiento obtenido con flujo continuo pero se mantiene constante para todas las frecuencias. También se ha demostrado que la distancia entre el punto de operación y el punto de rendimiento máximo de la turbina tiene un efecto importante sobre el rendimiento de la turbina. Cuanto más cerca este el punto de operación al punto de máximo rendimiento, más robusta es la turbina y se ve mucho menos afectada por el efecto del flujo pulsante. A medida que nos alejamos del punto de máximo rendimiento, los pulsos tienen un mayor efecto negativo sobre el rendimiento.

De los ensayos con flujo caliente, no-adiabático, no se ha podido obtener ninguna conclusión factible, ya que no se ha observado ninguna tendencia en los resultados. Parece ser que el efecto de los pulsos se queda oculto por detrás del efecto de transferencia de calor, siendo este por tanto más influyente en el rendimiento de la turbina que el propio efecto de los pulsos. De todas formas, se necesita realizar un estudio numérico y modelado detallado utilizando como base estos resultados experimentales, tanto en adiabático como en no-adiabático, para poder discernir con más detalle la influencia real de los pulsos instantáneamente en el rendimiento para entender y cuantificar mejor el efecto de flujo pulsante.

Pero para poder realizar un buen estudio numérico y modelado de la turbina, es necesario disponer de los mapas completos de gasto de la turbina y de su rendimiento. El problema reside en que la obtención de dichos mapas no es sencilla, ya que con el banco de turbos utilizado, los puntos que se pueden ensayar en la turbina son limitados por las características de choque y bombeo en el compresor, por lo que se requiere de una técnica fiable y lo más basada en la física posible de extrapolación de mapas. Es por ello que se ha desarrollado una técnica que permite la extrapolación tanto de mapas de gasto como de mapas de rendimiento de la turbina y ha sido validada con cinco turbinas radiales de sobrealimentación de diferentes tipos, convirtiéndola por tanto en válida para ser usada en códigos unidimensionales de simulación.

Además de estudiar el efecto de los pulsos, también se ha realizado estudio numérico y validación del sistema de control activo en turbinas para intentar aprovechar los pulsos y extraer la máxima energía del fluido. La teoría del concepto es muy prometedora, pero al acoplarla turbina con ACT en un motor reciproco, sus efectos beneficiosos se desvanecen, ya que es el motor el cual dicta el punto de funcionamiento de la turbina, por lo que toda la mejora que se consigue, se pierde al tener que compensar para mantener el punto de funcionamiento. La ganancia máxima de rendimiento de la turbina ha sido de 0.15%, mientras que para la mayoría de los casos ensayados ha sido negativa.

9. BIBLIOGRAFÍA

[1]. Filipi Z., Wang Y. and Assanis D. (2001) *"Effect of Variable Geometry Turbine (VGT) on Diesel Engine and Vehicle System Transient Response"*, SAE 2001-01-1247

[2]. Ghazikhani M., Davarpanaha M. and Mousavi Shaegha S.A., (2008) *"An experimental study on the effects of different opening ranges of waste-gate on the exhaust soot emission of a turbo-charged DI diesel engine"*, Energy Conversion and Management; Volume 49, Issue 10, 2563-2569

[3]. Winterbone, D.E., Nikpour, B., Alexander., G.I., *"Measurement of the performance of a radial inflow turbine in conditional steady and unsteady flow",* IMechE C405/015. Proceedings of the 4th International Conference on Turbocharging and Turbochargers, 153 - 162, 1990.

[4]. Nikpour, B., *"Measurement of the performance of a radial inflow turbine",* Ph.D. thesis, UMIST, Belfast, UK, 1990.

[5]. Arcoumanis, C., Hakeem, I., Khezzar, L., Martinez-Botas, R.F., Baines, N., *"Performance of a mixed flow turbocharger turbine under pulsating flow conditions",* ASME International gas turbine and aeroengine congress and exposition, (95-GT-210), June, 1995.

[6]. Szymko, S., *"The development of an eddy current dynamometer for evaluation of steady and pulsating turbocharger turbine performance",* Ph.D. thesis, Imperial College, London, UK, 2006.

[7]. Galindo, J., Serrano, J.R., Guardiola, C. and Cervelló, C., "*Surge limit definition in a specific test bench for the characterization of automotive turbochargers",* Experimental Thermal and Fluid Science 30, 449–462, 2007.

[8]. Benson, R.S., *"The thermodynamics and gas dynamics of internal-combustion engines"*, vol. I, Oxford University Press, Oxford, ISBN 0 19 856210 1, 1982.

[9]. Payri, F., Benajes, J., Reyes, M., *"Modelling of supercharger turbines in internal combustion engines",* Int J Mech Sci. 8–9:853–69, 1996.

[10]. Serrano, J.R., Arnau, F.J., Dolz, V., Tiseira, A., Cervelló, C., *"A model of turbocharger radial turbines appropriate to be used in zero- and one-dimensional gas dynamics codes for internal combustion engines modelling",* Energy Conversion and Management 49, 3729–3745, 2008.

[11]. García-Nieto S., Martínez M., Blasco X., and Sanchis J., (2008) *"Nonlinear predictive control based on local model networks for air management in diesel engines"*, Control Engineering Practice Volume 16, Issue 12, 1399-1413

[12]. Pesiridis A. and Martinez-Botas R. F. (2007) *"Experimental Evaluation of Active Flow Control Mixed-Flow Turbine for Automotive Turbocharger Application"*, J. Turbomachinery, Volume 129, Issue 1, 44

[13]. J.R. Serrano, P. Olmeda, A. Paez and F. Vidal (2010), *"An experimental procedure to determine heat transfer properties of turbochargers",* Measurement and Science Technology, 21 (2010) 035109 (14pp).

[14]. F. Payri, J.R. Serrano, P. Olmeda, A. Paez and F. Vidal (2010), *"Experimental methodology to characterize mechanical losses in small turbochargers"*, Proceedings of ASME Turbo Expo 2010: Power for Land, Sea and Air. GT2010-22815

[15]. Galindo J, Serrano J R, Arnau J R and Piqueras P. *"Description and analysis of a one-dimensional gas-dynamics model with independent time discretization"*. ASME Internal Combustion Engine Division 2008, ICES2008.20-27.

[16]. Payri F, Galindo J, Serrano JR and Arnau F J. *"Analysis of numerical methods to solve one-dimensional fluid-dynamics governing equations under impulsive flow in tapered ducts"*. International Journal Mechanical Sciences 2004. 981-1004.

ANEXO I: CARACTERIZACIÓN EXPERIMENTAL DE TURBINAS BAJO FLUJO PULSANTE

Characterization of turbochargers under pulsating flow

- RESULTS -

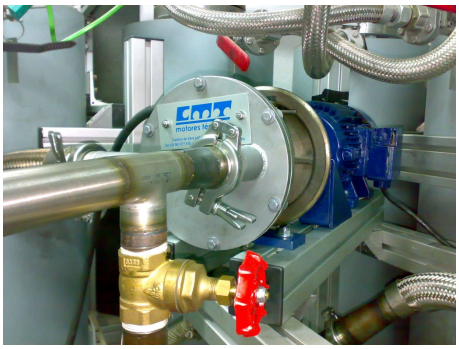

INDEX

- **Cold flow analysis**
- Hot flow analysis

Test campaign

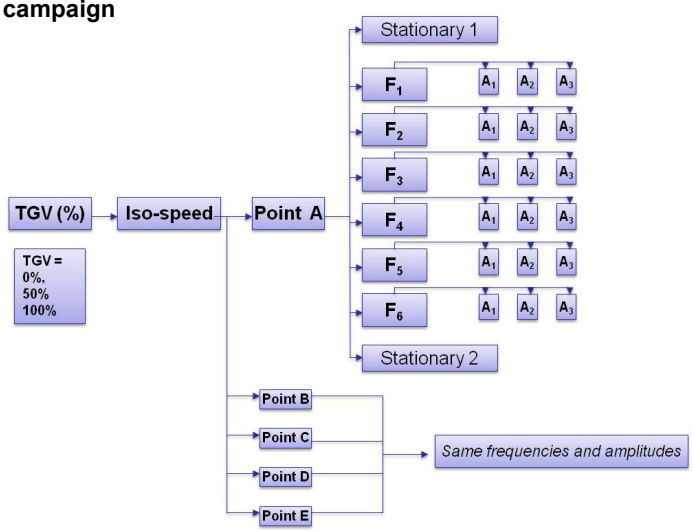

Test campaign

	2 Cyl		3 Cyl		4 Cyl		
	F6	F5	F4	F3	F2	F1	
VGT	1000	1250	1000	1250	1000	1250	RPM
0%	16.67	20.83	25.00	31.25	33.33	41.67	Hz
VGT	1500	2000	1500	2000	1500	2000	RPM
50%	25.00	33.33	37.50	50.00		66.67	Hz
VGT	3500	4000	3500	4000	3500	4000	RPM
100%	58.33	66.67	87.50	100.00	116.67	133.33	Hz

Amplitude	VGT 0%	VGT 50%	VGT 100%
A1	0.40 bar	0.50 bar	0.50 bar
A2	0.25 bar	0.30 bar	0.35 bar
A3	0.15 bar	0.15 bar	0.25 bar

Points tested

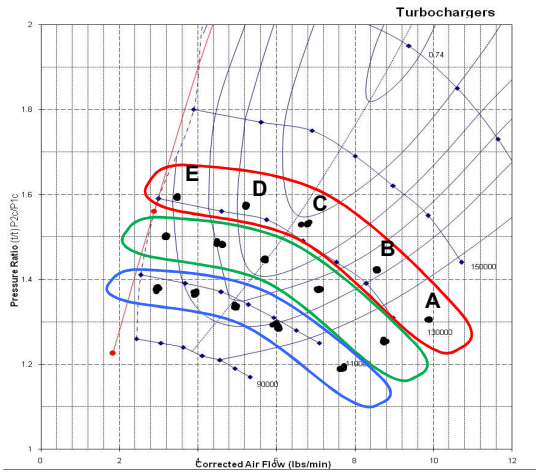

TGV 100%
Temperature choke: 66ºC
Temperature surge: 88ºC
Compressor speed*: 120000 rpm

TGV 50%
Temperature choke: 66ºC
Temperature surge: 90ºC
Compressor speed*: 131000 rpm

TGV 0%
Temperature choke: 60ºC
Temperature surge: 74ºC
Compressor speed*: 105000rpm

Total number of points tested

TGV 100% = **100** points
TGV 50% = **85** points
TGV 0% = **100** points

Points tested

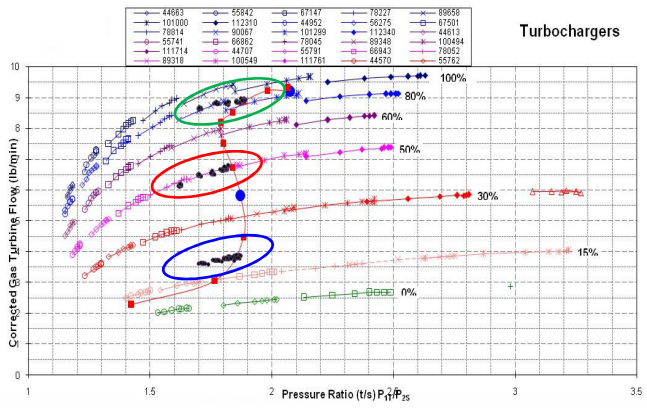

TGV 100%
Turbine speed*: 111000 rpm
Inlet temperature: 76ºC
Oil temperature: 76ºC

TGV 50%
Turbine speed*: 119000 rpm
Inlet temperature: 80ºC
Oil temperature: 80ºC

TGV 0%
Turbine speed*: 100000 rpm
Inlet temperature: 66ºC
Oil temperature: 66ºC

Pulse Frequency Analysis

Efficiency analysis was carried out separately for each TGV opening and number of cylinders.

Unfortunately, this did not allow to study the effect of the TGV opening and the real effect of frequency, as it was hidden under the number of cylinders.

For example:
4 Cyl,1000rpm,TGV 0% = 2 Cyl,2000rpm,50Hz = 33.33Hz
4 Cyl ,2000rpm,TGV 50% = 2 Cyl,4000rpm,TGV 100% = 66.67Hz

A new point of view can be obtained if all the results are **just** grouped by frequency and plotted versus non-dimensional efficiency (non-dimensional with respect to continuous flow efficiency).

A clearer tendency can be seen with respect to pulsating frequency (and not so much to the way you achieve that frequency).

Therefore, plots of frequency against non-dimensional efficiency have been presented here.

Pulse Frequency Analysis

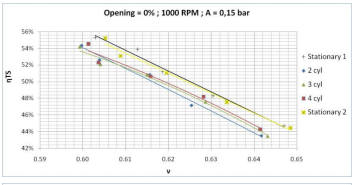

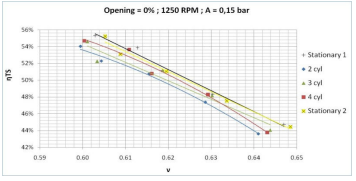

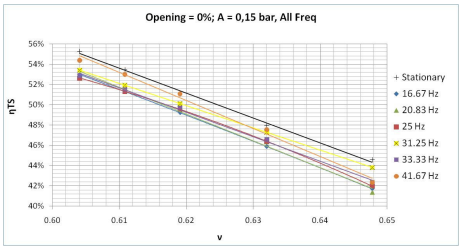

For consistency, the tested points have been interpolated in order to obtain the same blade to jet speed ratio

Average efficiency between the 2 stationary points has also been calculated.

This way, the non-dimensional efficiency for each frequency has been calculated taking the mean stationary efficiency with respect to the efficiency at each pulsating frequency at the same blade to jet speed ratio.

Cold flow analysis

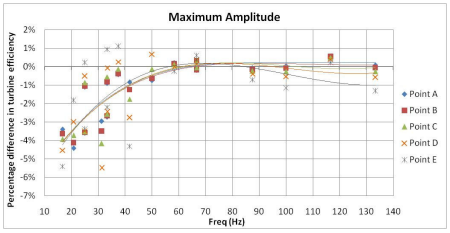

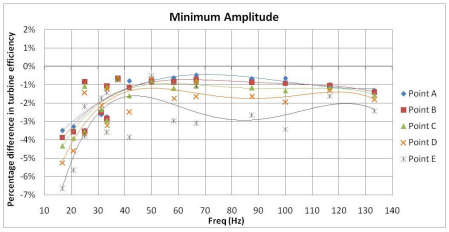

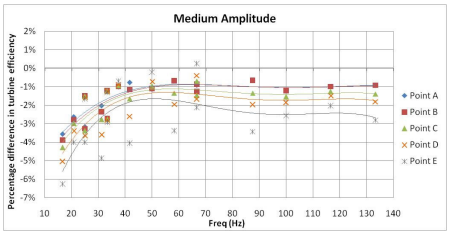

POINTS DISCRIMINATED BY AMPLITUDE AND IDENTIFIED BY BSR

- A clear efficiency reduction with decreasing frequency in all cases from Point A to Point E
- No effect at maximum amplitude over 50Hz
- Medium and minimum amplitude affects turbine efficiency over 50Hz (-1% to -2%, clear hierarchy with point A to E)
- Just a few points over 0% (<+1% → measurement uncertainty)

Cold flow analysis

Points discriminated by BSR and identified by VGT%

Point E (far BSR to BSR of max efficiency) shows high dispersion and high efficiency reduction. Points A & B show higher resistance to efficiency reduction. Seem only sensible to frequency effect.

VGT-50% (closer BSR to BSR of max efficiency) shows lower efficiency reduction.

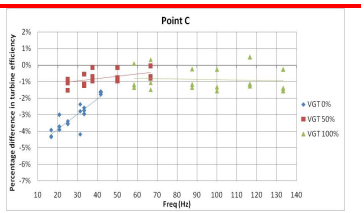

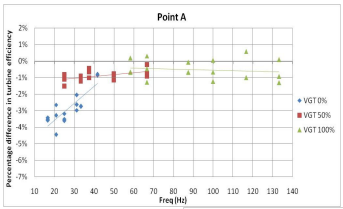

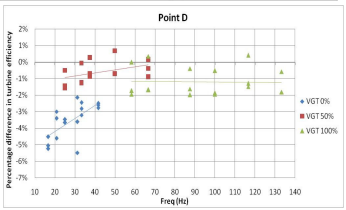

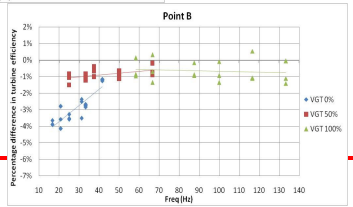

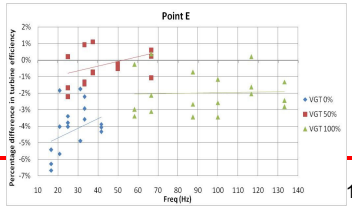

Cold flow analysis

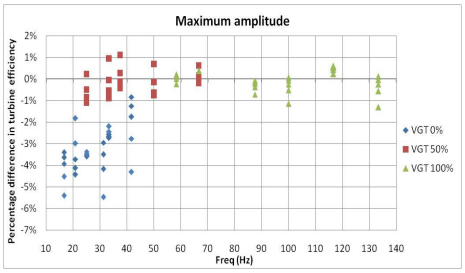

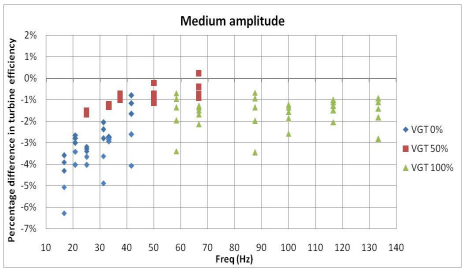

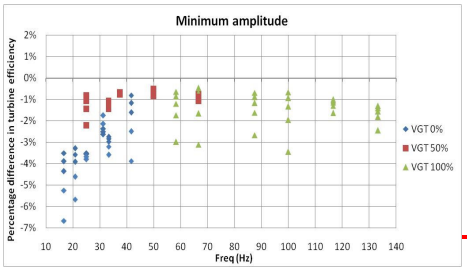

Points discriminated by Amplitude and identified by VGT%

VGT-50% (closer BSR to BSR of max efficiency) shows lower efficiency reduction.

Maximum amplitude extends points excursion to higher efficiency areas.

DISTANCE OF BSR TO BSR OF MAX EFFICIENCY IS EXPECTED TO BE AN IMPORTANT VARIABLE TO EXPLAIN EFFICIENCY REDUCTION

Cold flow analysis

The parameter used to define the distance of the operation point from the maximum theoretical blade to jet speed ratio is the following:

$$\Delta\sigma = \frac{\sigma_i - \sigma_{\max}}{\sigma_0 - \sigma_{\max}}$$

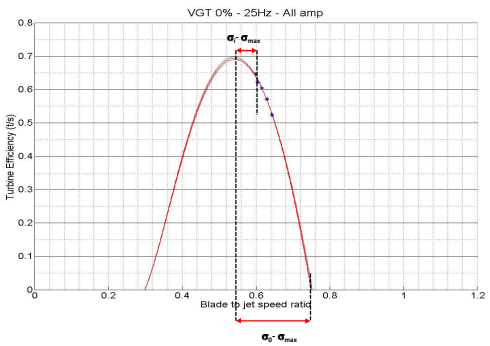

Efficiency extrapolation

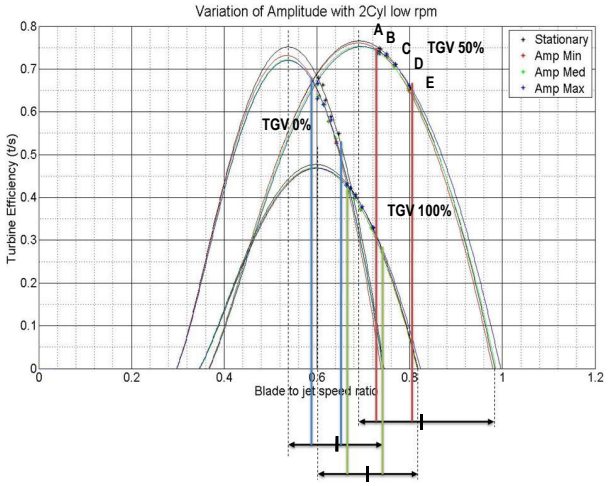

One explanation of the reason why 50% opening offers better results could be because the tested points are closer to the maximum efficiency. In this area turbine aerodynamic design is more robust and might mean that it is less affected by pressure pulses.

Cold flow analysis

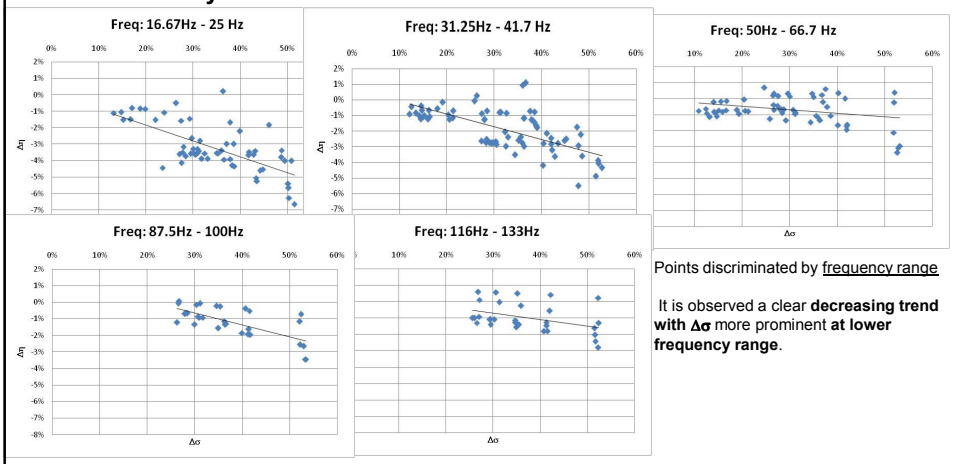

Points discriminated by frequency range

It is observed a clear **decreasing trend with Δσ** more prominent **at lower frequency range**.

Cold flow analysis

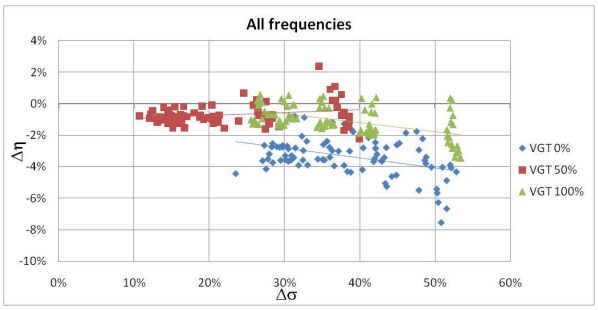

•VGT 50 % falls the less because shows the lower **Δσ** and they begin to fall when frequency decreases.

•VGT 0% falls the most because shows the higher **Δσ** and the lower frequency range.

•VGT 100% falls the less when shows the lower **Δσ** (due to Max amplitude higher excursions). Maximum reductions are at the higher **Δσ** (always lower than VGT 0% due to the higher frequency).

Cold flow analysis

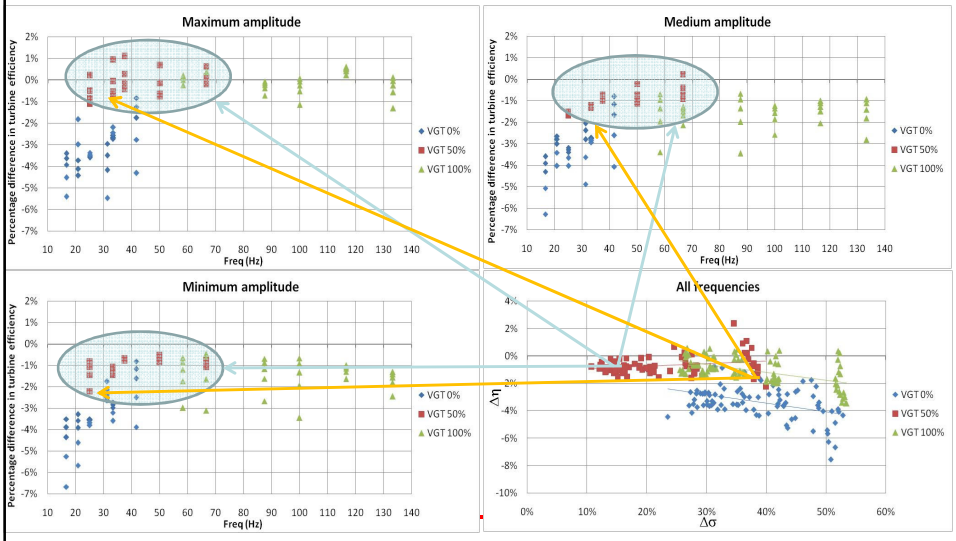

UNIVERSIDAD POLITECNICA DE VALENCIA

motores térmicos

Cold flow analysis

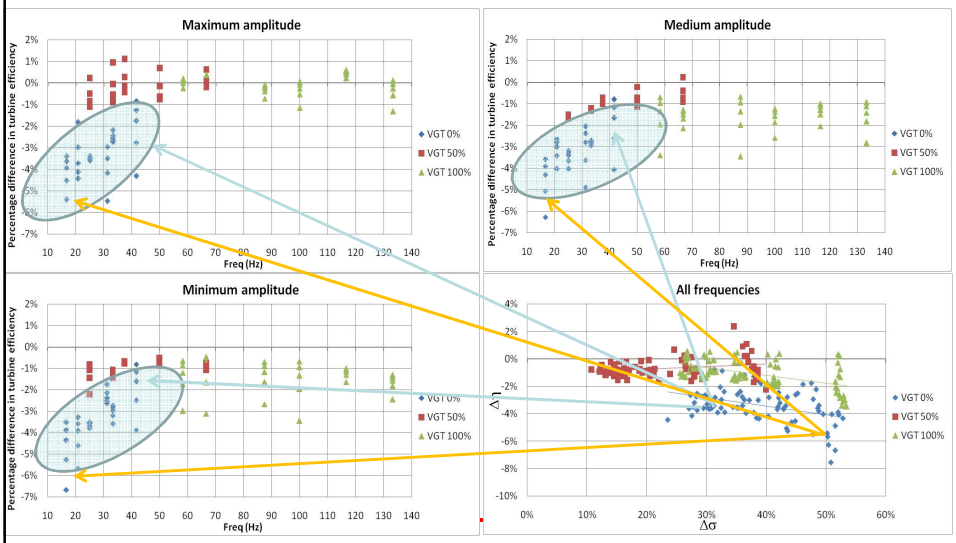

UNIVERSIDAD POLITECNICA DE VALENCIA

motores térmicos

Cold flow analysis

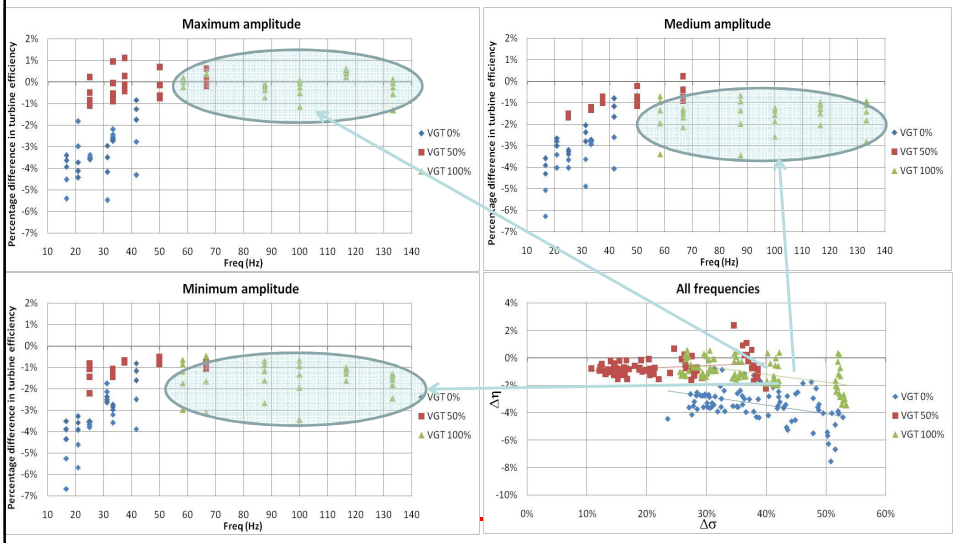

Cold flow analysis

Influence of mechanical efficiency

Example for VGT 0%

The parameter used to define the difference of stationary mechanical efficiency with the mean mechanical efficiency measured instantaneously is the following:

$$\Delta\eta_{mech} = \frac{\eta_{mech}^{i} - \eta_{mech}^{stationary}}{\eta_{mech}^{stationary}}$$

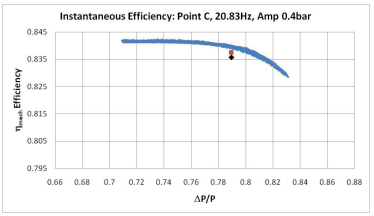

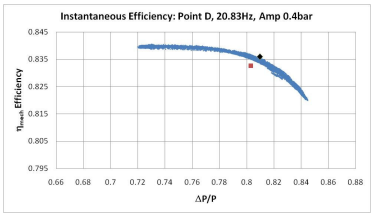

■ = Average mechanical efficiency
◆ = Stationary mechanical efficiency

Mechanical efficiency

$$\eta_{mech} = 0.322 \cdot \left[1 - e^{-0.00003 \cdot \mathrm{Re}_{Shaft}^{0.902} \cdot \mathrm{Pr}^{0.681}}\right] + 0.678 \cdot \left[1 - e^{-1.084 \cdot \left(\Delta P / P\right)^{-6.983}}\right]$$

$$\frac{\Delta P}{P} = \frac{P_{oil\_in} - \left(P_{Tur} - P_{Com}^{-}\right)}{P_{oil\_in}}$$

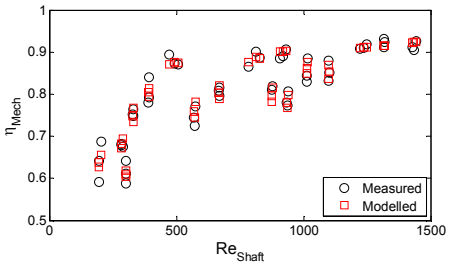

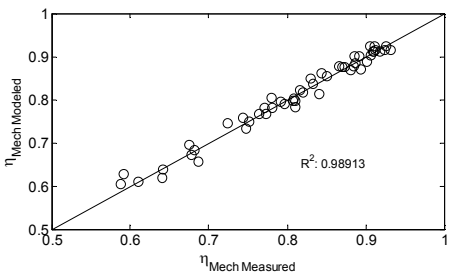

Cold flow analysis

Mechanical efficiency influence has been computed in a range between +1% and -2% with respect to steady flow estimated values.

Even some trend with $\Delta\sigma$ is observed, main reason is due to axial load average value and instantaneous oscillation ($\Delta P/P$)

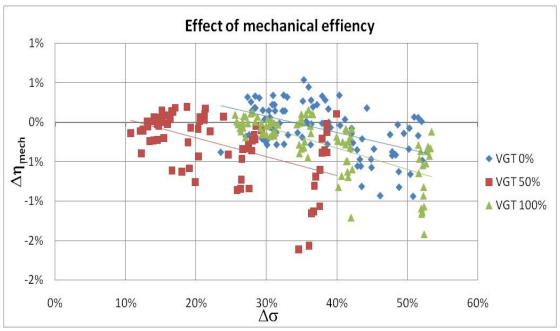

INDEX

- Cold flow analysis
- **Hot flow analysis**

Hot testing procedure

- Only 4 operation points (A,B,C,D) tested for each VGT opening
- Only 2 AMPLITUDES tested for each operation point
- Only 1 stationary point tested for each operation point
- All operation points at each VGT opening at iso-speed and iso-temperature
- Same frequencies as cold flow tests

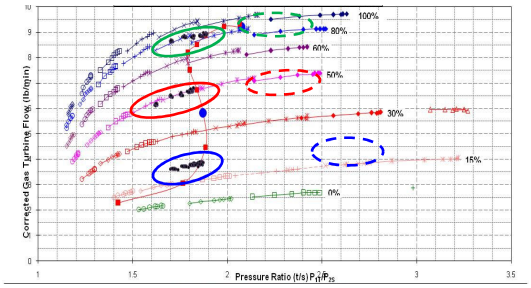

For comparison between hot and cold tests the **same turbocharger uncorrected speed was kept constant**

Hot testing procedure

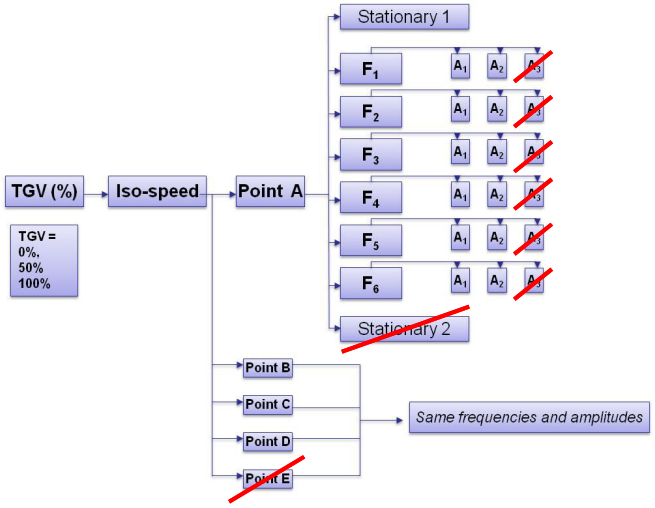

Hot testing procedure

	2 Cyl		3 Cyl		4 Cyl		
	F_6	F_5	F_4	F_3	F_2	F_1	
VGT	**1000**	**1250**	**1000**	**1250**	**1000**	**1250**	RPM
0%	16.67	20.83	25.00	31.25	33.33	41.67	Hz
VGT	**1500**	**2000**	**1500**	**2000**	**1500**	**2000**	RPM
50%	25.00	33.33	37.50	50.00		66.67	Hz
VGT	**3500**	**4000**	**3500**	**4000**	**3500**	**4000**	RPM
100%	58.33	66.67	87.50	100.00	116.67	133.33	Hz

Amplitude	VGT 0%	VGT 50%	VGT 100%
A1	0.50 bar	0.60 bar	0.80 bar
A2	0.30 bar	0.30 bar	0.40 bar

Summary of results

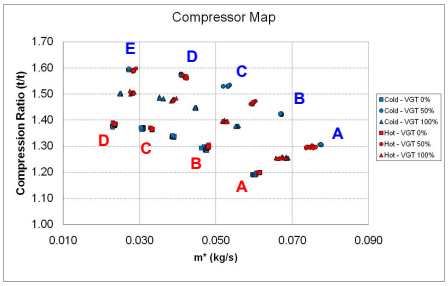

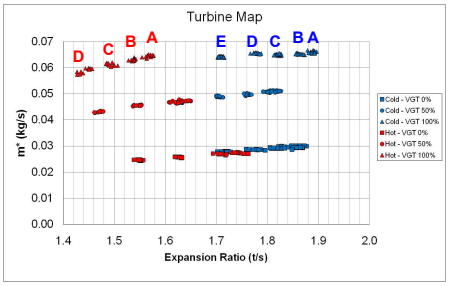

	Cold tests					Hot tests				
VGT	Speed (rpm)	Compressor speed* (rpm)	Turbine speed* (rpm)	TIT (ºC)	Oil Temp (ºC)	Speed (rpm)	Compressor speed* (rpm)	Turbine speed* (rpm)	TIT (ºC)	Oil Temp (ºC)
0%	**106600**	105400	100400	66	66	**106600**	106100	73600	360	95
50%	**130000**	129900	119000	82	82	**130100**	129300	87300	390	95
100%	**121000**	119800	111500	76	76	**121100**	120200	80600	400	95

Pressure pulses

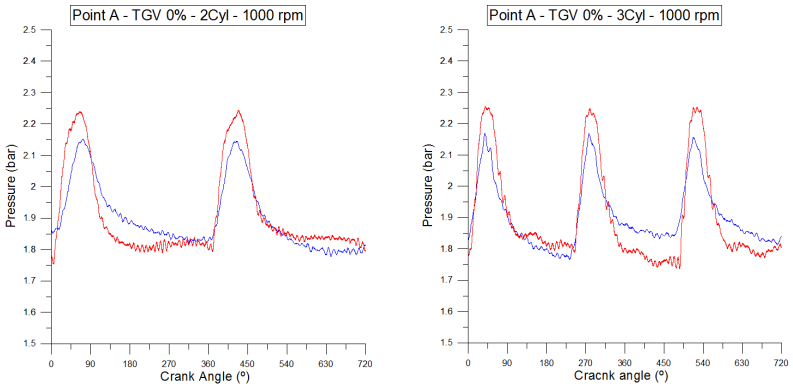

= Hot pulsating rotary valve

= Cold pulsating rotary valve

Analysis

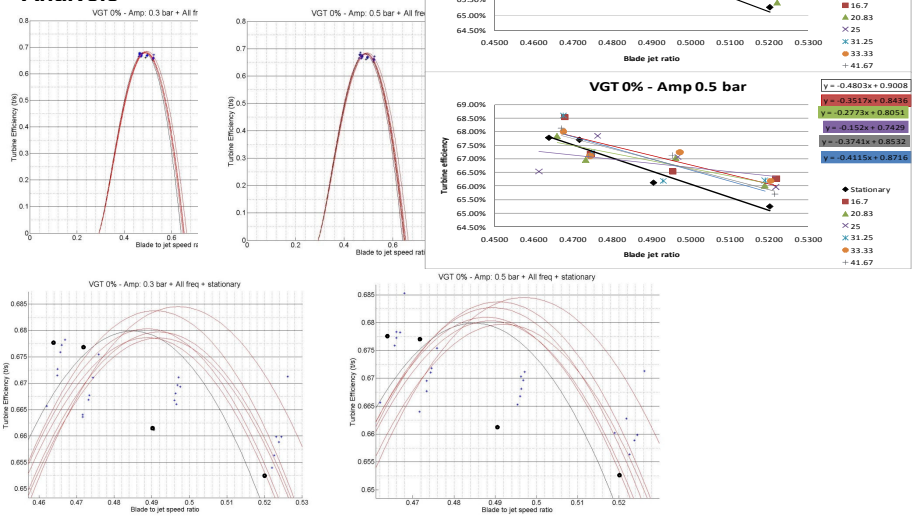

UNIVERSIDAD POLITECNICA DE VALENCIA

Analysis

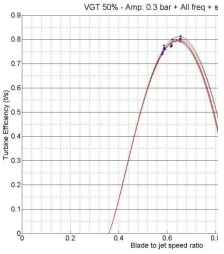

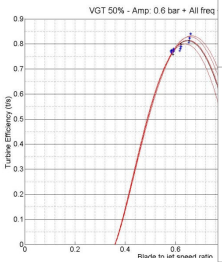

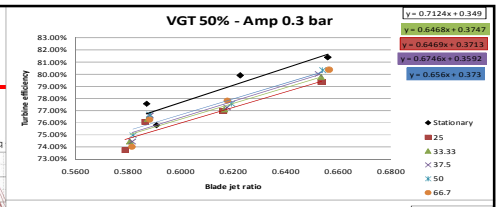

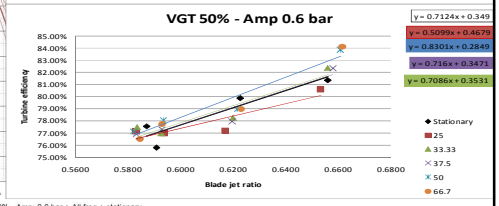

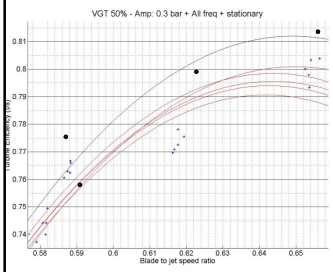

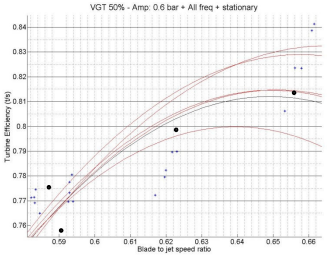

29

UNIVERSIDAD POLITECNICA DE VALENCIA

Analysis

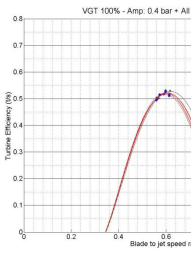

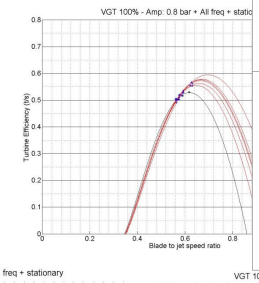

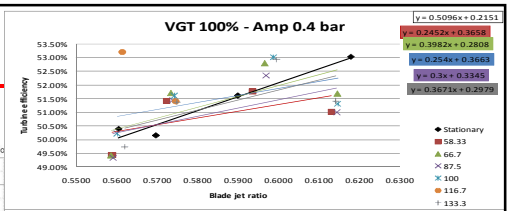

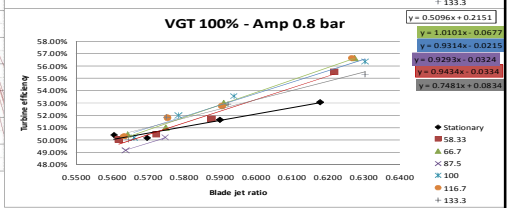

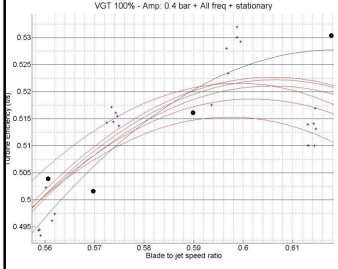

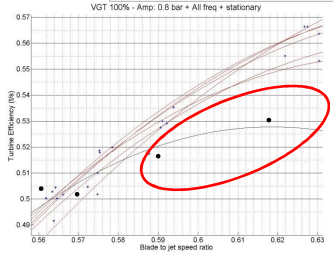

30

Analysis

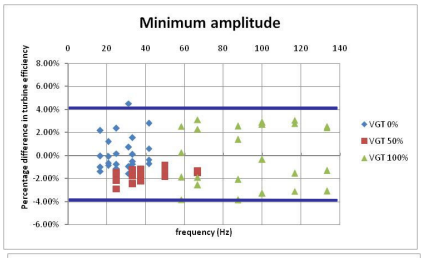

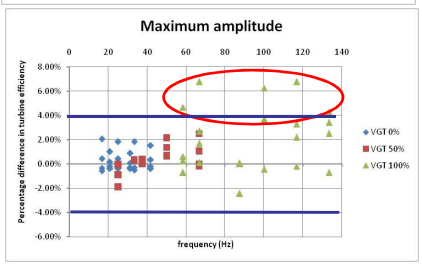

Graphs plotted using CMT extrapolation technique

Pulsating flow seems to have no significant effect on turbine efficiency under hot conditions.

No effect from amplitude
No effect from frequency

Analysis

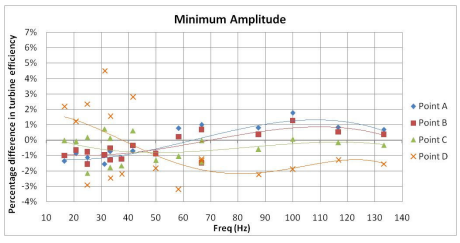

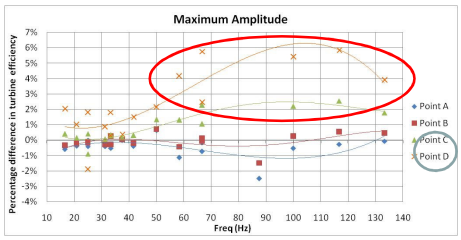

Graphs plotted using CMT extrapolation technique

Pulsating flow seems to have no significant effect on turbine efficiency under hot conditions.

No effect from amplitude
No effect from frequency

No clear tendency between points

ANEXO II: ESTIMATION OF THE EXTENDED TURBINE MAPS FOR A RADIAL INFLOW TURBINE

SAE International™

Estimation of the Extended Turbine Maps for a Radial Inflow Turbine

2010-01-1234
Published
04/12/2010

Jose Ramon Serrano, Benjamin Pla, Ricardo Gozalbo and Diego Ospina
Univ. Politecnica de Valencia

ABSTRACT

Characterization of radial turbine performance is usually represented by turbine characteristics maps. These maps illustrate the relationship between the most representative variables which describe the system behavior.

Many times, due to design constrains available in these test beds, it is not possible to get measurements of the different variables at different turbine rotational speeds over a wide range of expansion ratios. Sometimes this represents a problem when an appropriate engine simulation must be carried out due to the lack of reliable information to run the simulation in operation points where there are no available turbine data. Although an extrapolation could be done using mathematical methods, there are no physics behind which assures an acceptable confidence in the new generated information.

The present paper develops a physics based method for the extrapolation of the radial turbine maps to zones where there is no experimental information.

This method takes into account the definition of the turbine specific diameter as a function of the representative variables illustrated in the maps in order to get a relationship that allows expressing the corrected mass flow against known information, geometric, thermodynamic and specific data and as a function of the expansion ratio. The efficiency is extrapolated by an expression developed from the definition of turbine total to static efficiency and the consideration of velocity triangles.

Results are compared against experimental information and it is found that there is a good agreement between theoretical and test data.

INTRODUCTION

When studying the performance characteristics of turbomachinery it is a great help if results from different sources are directly comparable, even for machines of somewhat different size. A way to do this is via a characterization of the main performance parameters involved in the operation of such elements and the compilation of these results into characteristic curves. The aforementioned parameters should be preferably standardized because it will allow better comparisons between the performance of the elements [1].

For a radial inflow turbine the standardized performance parameters used to characterize its behavior are a mass flow parameter, usually defined as the mass flow circulating through the stage corrected with a ratio between the square root of turbine inlet temperature to the turbine inlet pressure, and the turbine total to static efficiency used in this form to discount the kinetic energy lost in the exit. Although there could be variations in the way to define these parameters, the philosophy of being comparable by means of standardization remains in any case. To compute the characteristics curves, the mass flow parameter usually is plotted against the turbine expansion ratio for different speeds while the efficiency is used to be plotted against the blade to jet speed ratio, a ratio of the rotor tip linear velocity to the isentropic velocity through the turbine stage, or the expansion ratio, for different speeds too [2]. A typical radial turbine map is shown in Figure (1).

The turbine characteristic curves, or simply turbine maps, usually are constructed by taking appropriate measurements of turbine mass flow, inlet and outlet pressures and temperatures and then using this information to calculate the required parameters to be plotted. This data set is measured through a series of experiments in special design test rigs. Several types of these test rigs have been constructed by

different researchers and for different purposes. Dale [3] used a test facility built at Imperial College to conduct research about unsteady flow in radial turbines. Winterbone et al. [5] and Nikpour [6] also developed a similar facility using a hydraulic dynamometer. Arcoumanis et al. [7] replace the dynamometer by a radial compressor to enable increased power of larger turbines to be absorbed. Szymko [4] developed an installation where an eddy current dynamometer was located in order to absorb the power of the turbine and for providing a low and known inertia of the rotating assembly which aids in the measurement accuracy of the instantaneous torque.

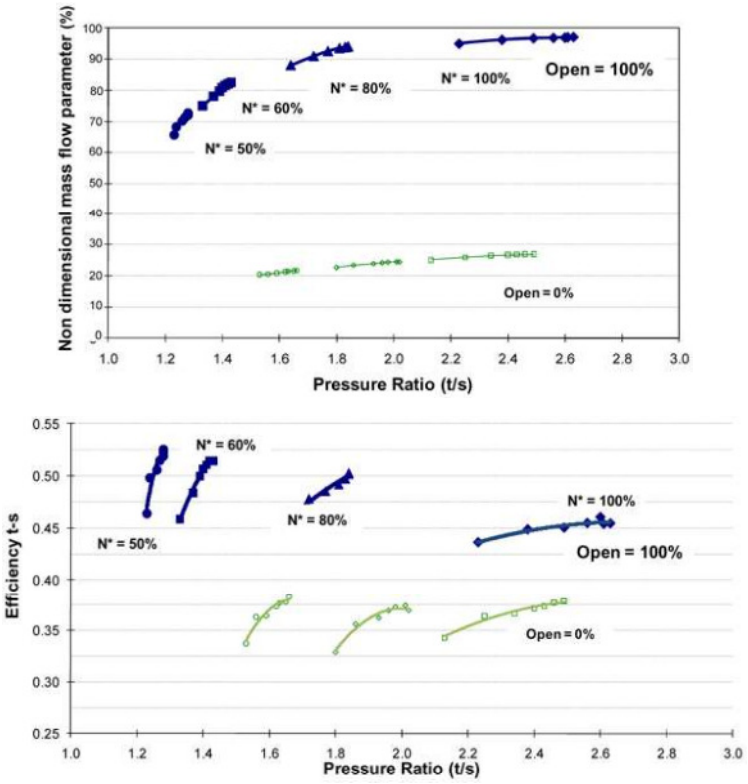

Figure 1. Passenger car turbocharger radial turbine maps

In the continuous flow test bed at *CMT-Motores Térmicos*, the compressor is used as a braking device [8]. This facility is employed for taking measurements of mass flow, temperatures and pressures for turbochargers so the turbine maps can be calculated. By controlling the energy supplied to the turbine and the backpressure in the compressor side, it is possible to get measurements for a wide range of turbine speeds. However the widespread of data that can be collected depends strongly on the surge and choked limits in the compressor. It follows that these turbine maps are valid for just for a range of expansion and blade to jet speed ratios. Outside this range there is no experimental data available.

Some turbine models such as those developed by Benson [9], Payri et al. [10] and Serrano et al. [11] make use of those characteristic curves to model the mass flow versus expansion ratio behavior of the turbine and for solving boundary conditions in engine simulation codes. These authors provide a reliable method to calculate the mass flow vs. expansion ratio curve for unsteady flow and for variable and fixed geometry turbines but not for the efficiency vs. blade to jet speed ratio curve. In addition, they are 1D or 0D models more complex than straightforward extrapolations that are sometimes required.

This paper proposes a reliable method for extrapolating the efficiency curve and an alternative way to calculate the mass flow curve via a series of equations based on physical principles. The definition of turbine efficiency is used as well as those for specific variables such as specific diameter. One objective will be to develop an expression for the efficiency as a function of the blade jet to speed ratio and some constants related to loss mechanisms, geometrical and gas properties so they can be fitted easily to the available experimental information of any radial turbine map. In the same way of thinking, a similar procedure will be done for the mass flow map, in this case based on the definition of specific diameter. The objective here is more to backup the goodness of the method depicted in references [10] and [11]. This set of equations will allow an initial extrapolation of the maps. The procedure will be validated with experimental data and will be valid for stationary and quasi-stationary flow, which is a different approach that the one proposed in references [10] and [11].

This model allows the fitting of a physical based mathematical formula to the turbine maps and consequently the extension of the curves to values experimentally inexistent, using mainly information contained into the maps and a few gas properties and geometrical information. The extrapolation is semi-empirical for the fluid-dynamic characteristics of the turbine. This procedure will be demonstrated for three turbines with different characteristics.

DESCRIPTION OF TURBINES

Three different turbines will be used for the application of the extension technique described in this paper. They are selected to cover a significant range of applications. The first one is a small turbine from a turbocharger of a passenger car engine which was tested at CMT - Motores Térmicos continuous test rig (Figure (1)). The second one is a truck turbocharger radial turbine described in the "Turbo trends and requirements forum" of the 8th International Conference on Turbochargers and Turbocharging [12] (Figure (2)) that was meassured in the brake developed by Szymko et al [13]. This is a larger turbine which has a wide range of efficiencies and mass flow measurements than those usually found in conventional

turbine maps. Finally, a single stage commercial radial inflow turbine used for an analysis made by Futral [14] (Figure (3)).

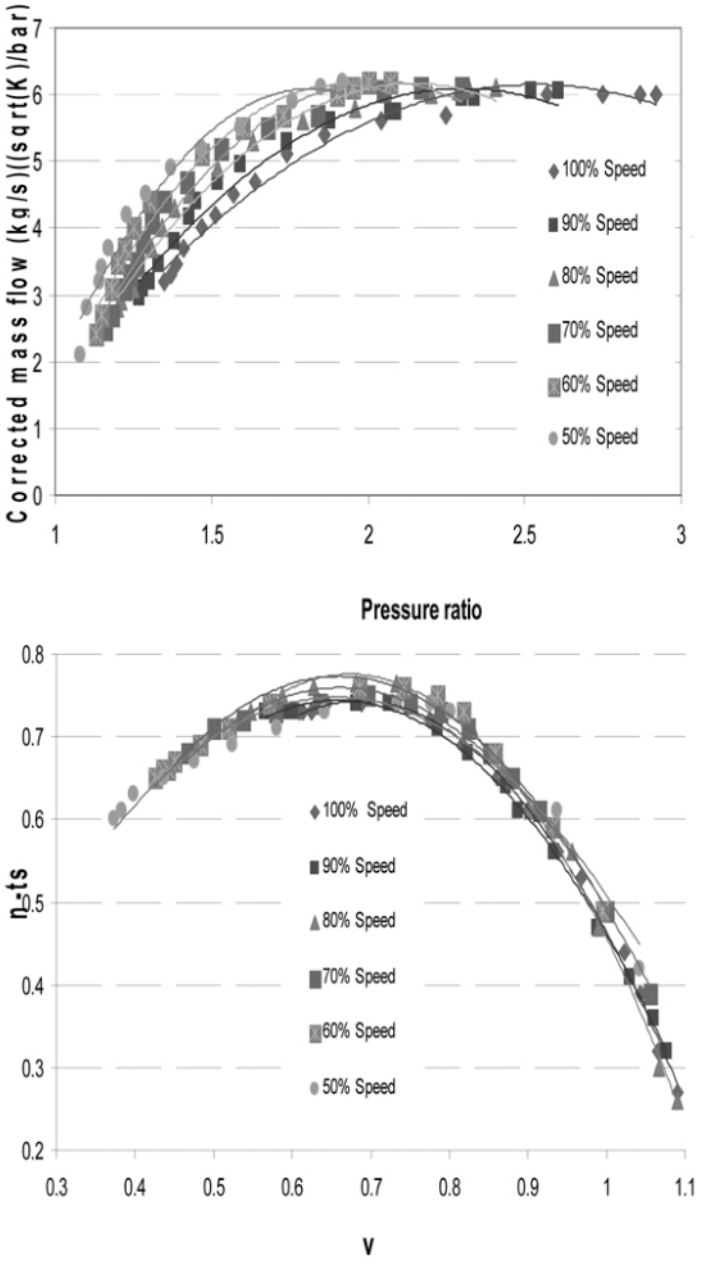

Figure 2. Truck turbocharger radial turbine maps (From reference [12])

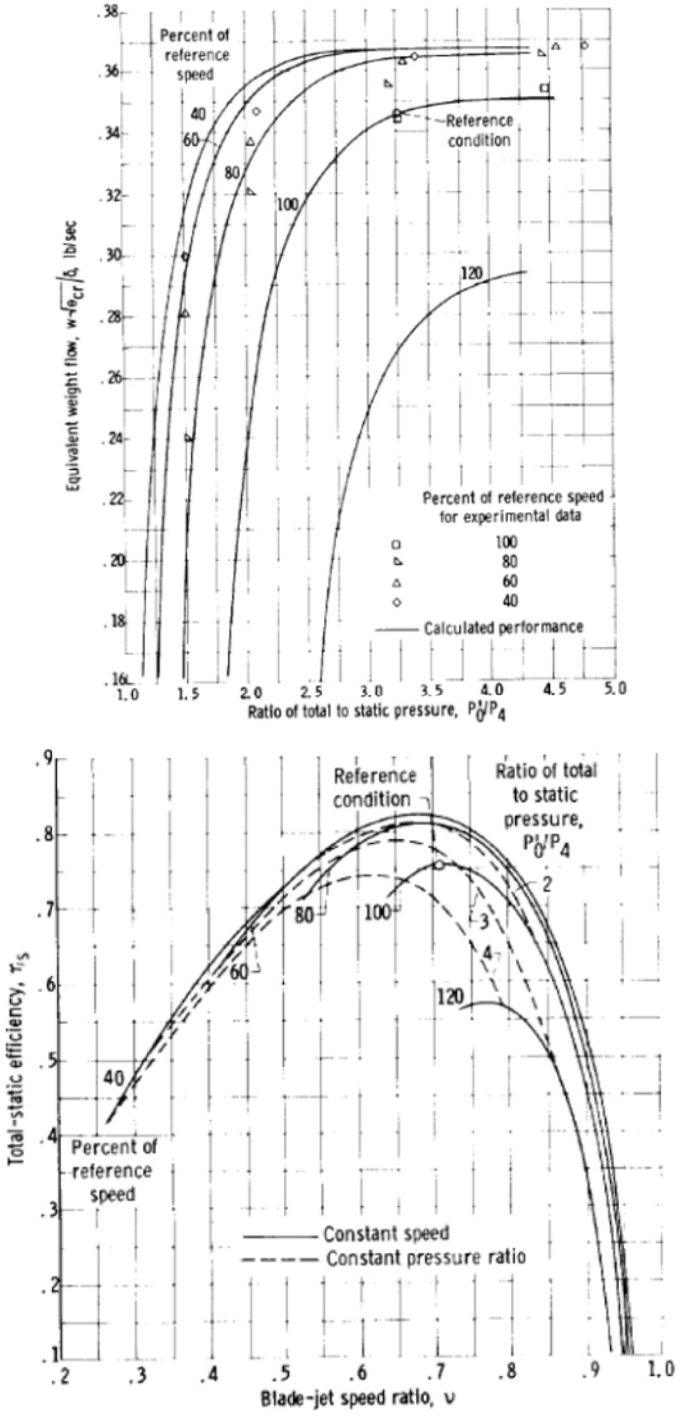

Figure 3. Single stage commercial radial inflow turbine maps (from reference [13])

Nomenclature for the turbine corresponds to Figure (4) in the enthalpy versus entropy diagram. Where '0' correspond to stator inlet, '1' to rotor inlet and '2' to rotor outlet conditions respectively. 'R' refers to relative conditions.

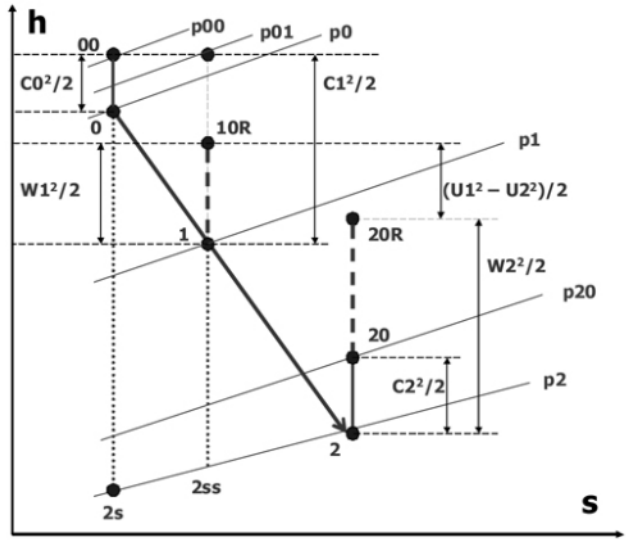

Figure 4. Enthalpy - entropy (h-s) diagram

Figure 5 shows the triangles of velocities for a radial turbine. It also shows the flow angles and the constant circulation velocity assumed in the analysis ($C_0 = C_{r1} = C_{a2}$). The angle α_1 is defined as the angle between absolute velocity vector and meridional plane at mean channel. In the case of turbines with nozzles in the stator vane, it is the angle between the stator blade chord and the line which joins the centre of rotation of the blade and the centre of the wheel. The angle β_2 is defined as the angle between the velocity vector relative to the wheel and meridional plane at mean channel. It is the geometric rotor exit blade angle.

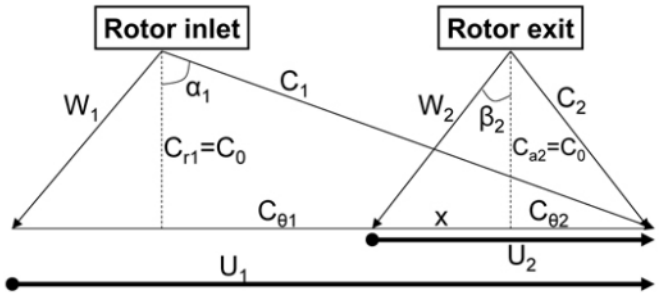

Figure 5. Triangles of velocities for a radial inflow turbine

EFFICIENCY EQUATION

An equation which allows the representation of the efficiency map and with the potential for doing extrapolations must be developed. For the accomplishment of this task, it is useful to remind the definition of total to static efficiency:

$$\eta_{ts} = \frac{h_{00} - h_{02}}{h_{00} - h_{2s}} = \frac{T_{00} - T_{02}}{T_{00} - T_{2s}} \tag{1}$$

The objective will be to transform equation (1) into an expression as a function of the blade jet to speed ratio and some constants that can be fitted to the experimental data. For doing this, the triangles of velocities at the inlet and exit of the turbine must be taken into account. From Figure (5) it can be considered that:

$$\tan\alpha_1 = \frac{C_{\theta 1}}{C_0} \Rightarrow C_{\theta 1} = C_0 \tan\alpha_1 \tag{2}$$

$$\tan\beta_2 = \frac{x}{C_0} \Rightarrow x = C_0 \tan\beta_2 \tag{3}$$

$$U_2 = x + C_{\theta 2} \Rightarrow C_{\theta 2} = U_2 - x \tag{4}$$

Recalling the general relationship between the lineal velocity and the rotational velocity and applying it to the rotor:

$$\frac{U_1}{r_1} = \frac{U_2}{r_2} \Rightarrow U_2 = U_1\left(\frac{r_2}{r_1}\right) \tag{5}$$

Inserting equations (3) and (5) into (4):

$$C_{\theta 2} = U_1\left(\frac{r_2}{r_1}\right) - C_0 \tan\beta_2 \tag{6}$$

Recalling equation (1) and expanding it:

$$\eta_{ts} = \frac{h_{00} - h_{02}}{h_{00} - h_{2s}} = \frac{T_{00} - T_{02}}{T_{00} - T_{2s}} = \frac{T_{00} - T_{02}}{T_{00}\left(1 - \left(\frac{1}{ER}\right)^{\frac{\gamma-1}{\gamma}}\right)} \tag{7}$$

From the definition of power and Euler's equation [1], it can be stated that:

$$W = \dot{m} \cdot C_p\left(T_{00} - T_{02}\right) \tag{8}$$

$$W = \dot{m}\left(U_1 C_{\theta 1} - U_2 C_{\theta 2}\right) \tag{9}$$

Combining (8) and (9):

$$T_{00} - T_{02} = \frac{U_1 C_{\theta 1} - U_2 C_{\theta 2}}{C_p} \tag{10}$$

Inserting equation (2), (5), (6) and (10) into (7) and arranging terms:

$$\eta_{ts} = \frac{U_1 C_{\theta 1} - U_2 C_{\theta 2}}{C_p T_{00}\left(1 - \left(\frac{1}{ER}\right)^{\frac{\gamma-1}{\gamma}}\right)} \tag{11}$$

$$\eta_{ts} = \frac{U_1 C_0 \tan\alpha_1 - U_1\left(\frac{r_2}{r_1}\right)\left[U_1\left(\frac{r_2}{r_1}\right) - C_0 \tan\beta_2\right]}{C_p \cdot T_{00}\left(1 - \left(\frac{1}{ER}\right)^{\frac{\gamma-1}{\gamma}}\right)} \tag{12}$$

From the definition of the blade jet to speed ratio [2] it is recalled that the velocity which would be attained if the working fluid in the turbine were expanded in an ideal nozzle over the same expansion ratio as that of the turbine is:

$$C_s^2 = 2C_p \cdot T_{00}\left[1 - \left(\frac{1}{ER}\right)^{\frac{\gamma-1}{\gamma}}\right] \tag{13}$$

Comparing equation (13) to the denominator of equation (12) then efficiency equation can be written as (14):

$$\eta_{ts} = \frac{-2U_1^2\left(\frac{r_2}{r_1}\right)^2 + 2U_1 C_0\left(\tan\alpha_1 + \left(\frac{r_2}{r_1}\right)\tan\beta_2\right)}{C_s^2} \tag{14}$$

recalling that:

$$\upsilon = \frac{U_1}{C_s} \tag{15}$$

and arranging terms into constants equation (14) can be written as:

$$\eta_{ts} = -K_1\upsilon^2 + K_2\upsilon\frac{C_0}{C_s} \tag{16}$$

where:

$$K_1 = 2\left(\frac{r_2}{r_1}\right)^2 \tag{17}$$

$$K_2 = 2\left(\tan\alpha_1 + \left(\frac{r_2}{r_1}\right)\tan\beta_2\right) \tag{18}$$

It is necessary to develop an expression for the term C_0/C_s in equation (16) in order to be functional. One way to do that is firstly to replace directly the definitions of the velocities implied in this ratio. C_s has been already defined in equation (13). C_0, circulation velocity, can be found using the continuity equation:

$$C_0 = \frac{\dot{m}RT_0}{p_0 A_0} \tag{19}$$

Inserting equations (13) and (19) into C_0/C_s and solving for the mass flow:

$$\dot{m} = \left(C_0/C_s\right)\frac{p_0 A_0}{R_0 T}\sqrt{\gamma RT_{00}}\sqrt{\frac{2}{\gamma-1}\left(1 - \left(\frac{1}{ER}\right)^{\frac{\gamma-1}{\gamma}}\right)} \tag{20}$$

Recalling the equation through a nozzle [15]:

$$\dot{m} = A_{eff}\frac{p_{00}}{\sqrt{\gamma RT_{00}}}\gamma\left(\frac{1}{ER}\right)^{\frac{1}{\gamma}}\sqrt{\frac{2}{\gamma-1}\left(1 - \left(\frac{1}{ER}\right)^{\frac{\gamma-1}{\gamma}}\right)} \tag{21}$$

Equating expressions (20) and (21) and solving for C_0/C_s:

$$\frac{C_0}{C_s} = \frac{A_{eff}p_{00}\gamma\left(\frac{1}{ER}\right)^{\frac{1}{\gamma}}RT_0}{p_0 A_0 \gamma RT_{00}} = \frac{A_{eff}}{A_0}\left(\frac{1}{ER}\right)^{\frac{1}{\gamma}}\left(\frac{T_0}{T_{00}}\right)^{\frac{1}{\gamma}} \tag{22}$$

For hot tests usually T_0/T_{00} is close to one, so substituting equation (22) into (16):

$$\eta_{ts} = -K_1\upsilon^2 + K_2\upsilon\frac{A_{eff}}{A_0}\left(\frac{1}{ER}\right)^{\frac{1}{\gamma}} \tag{23}$$

In equation (23) it is interesting to note that, providing ER is constant, the efficiency is zero at a blade to jet speed ration

equal to zero. According to equations (13) and (14) and with constant ER, this is only possible if rotor tip velocity (U_1) is zero at this condition. This results in a turbine efficiency map passing through the origin at zero blade to jet speed ration for every constant ER curve, as it could be expected.

Nevertheless, it is normal practice and easier measuring turbocharger characteristics at constant corrected rotor tip speed either than at constant ER. Therefore, an expression with this constant variable will be looked for. Corrected rotor tip velocity of the turbine is defined as:

$$U_1^* = \frac{U_1}{\sqrt{T_{00}}} \tag{24}$$

Combining equation (24) with (13) and (14) and solving for 1/ER:

$$\left(\frac{1}{ER}\right) = \left[1 - \frac{U_1^{*2}}{2C_p \upsilon^2}\right]^{\frac{\gamma}{\gamma-1}} \tag{25}$$

Inserting (25) in (23):

$$\frac{C_0}{C_s} = \frac{A_{eff}}{A_0}\left[1 - \frac{(\gamma-1)U_1^{*2}}{2\gamma R \upsilon^2}\right]^{\frac{1}{\gamma-1}}\left(\frac{T_0}{T_{00}}\right)^{\frac{1}{\gamma}} \tag{26}$$

Equation (26) is valid if flow has not been choked in the turbine. When chocked corrected mass flow ($\dot{m}_c^*$) is got, then C_0 for choked flow conditions can be written as:

$$C_0 = \frac{\dot{m}RT_0}{p_0 A_0} = \frac{\dot{m}_c^* R\sqrt{T_0}}{A_0}\left(\frac{T_0}{T_{00}}\right)^{\frac{2-\gamma}{2\gamma}} \tag{27}$$

Considering equation (27), blade to speed ratio definition (14) and corrected tip speed definition (24) and solving for C_0/C_S it is possible to obtain such velocity ratio in choked flow conditions, as shows equation (28):

$$\left(\frac{C_0}{C_S}\right)_c = \frac{\upsilon}{U_1}\frac{\dot{m}_c^* R\sqrt{T_0}}{A_0}\left(\frac{T_0}{T_{00}}\right)^{\frac{2-\gamma}{2\gamma}} = \frac{\dot{m}_c^*}{U_1^*}\frac{R\upsilon}{A_0}\left(\frac{T_0}{T_{00}}\right)^{\frac{1}{\gamma}} \tag{28}$$

For turbine operative points located in a constant rotational speed line, U^*_1 is a constant and for hot tests usually T_0/T_{00} is close to one. Therefore, inserting equation (26) or (28) into (16) and rearranging constants it is obtained turbine efficiency for normal flow as equation (29) or for choked flow as equation (30) respectively:

$$\eta_{TS} = -K_1\upsilon^2 + K_2^*\left[1 - \frac{K_3}{\upsilon^2}\right]^{\frac{1}{\gamma-1}}\upsilon \tag{29}$$

$$\left(\eta_{ts}\right)_c = -K_1\upsilon^2 + K_2\upsilon^2\frac{\dot{m}_c^*}{U_1^*}\frac{R}{A_0} = \upsilon^2\left(K_2\frac{\dot{m}_c^*}{U_1^*}\frac{R}{A_0} - K_1\right) \tag{30}$$

Where K_1 and K_2 have been already defined in equations (17) and (18) respectively and:

$$K_2^* = 2\frac{A_{eff}}{A_0}\left(\tan\alpha_1 + \left(\frac{r_2}{r_1}\right)\tan\beta_2\right) \tag{31}$$

$$K_3 = \frac{(\gamma-1)U_1^{*2}}{2\gamma R} \tag{32}$$

K^*_2 has to be further expanded by considering the A_{eff} as variable. Payri [16] and Zinner [17] proposed a linear relationship between the effective area A_{eff} and the blade jet to speed ratio. Taking into account this fact and equation (25), a relationship between A_{eff} and υ is established in equation (33).

$$A_{eff} = -a\cdot\upsilon + b \tag{33}$$

Additionally, considering the two nozzles model for the stator and the rotor [11] and plotting their effective areas versus blade jet to speed ratio for a given operative conditions of the passenger car turbine, Figure (6) is obtained. It shows that a linear negative trend in the form of equation (33) can be obtained.

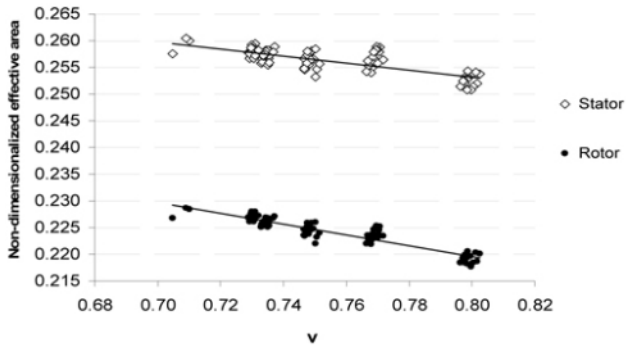

Figure 6. Effective areas for the passenger car radial turbocharger turbine tested at cold flow in CMT - Motores Térmicos

Table 1 shows the experimental values for some constants determined from geometrical variables measurements (r_1, r_2, A_0, α, and β) and from gas properties (γ and R).

Table 1. Constants experimental values for passenger car and commercial turbine

	Passenger car turbine	Commercial turbine
K_1	0.670	0.645
K_2^*/A_{eff}	223.5	379.5
$K_3/(U_1^*)^2$	4.33 E-04	2.02 E-03

Equation (29) and equation (30) have been applied to the turbines previously described in order to get the efficiency extended map. The results of the extension of these curves are shown in Figures (7),(8),(9) for different turbine speeds. Forcing the curves up to an efficiency value near zero was done in order to get a general view of the entire turbine behavior. As it can be seen, there is a good agreement between the fitted curve and the experimental data.

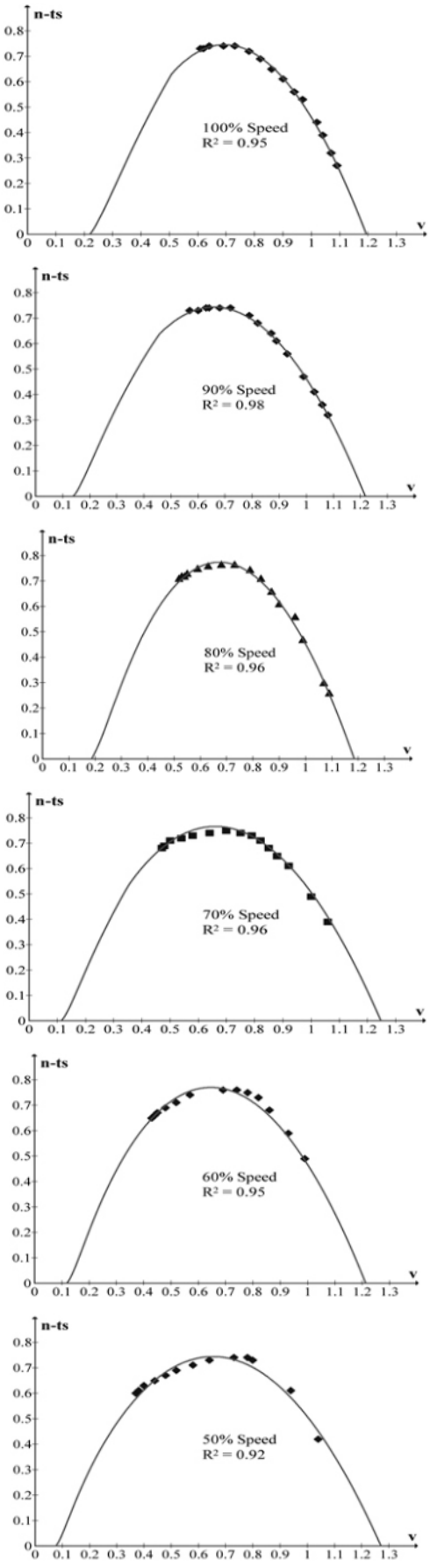

Figure 7. Efficiency extension for truck turbocharger radial turbine (U_1* from 100% to 50% every 10%)

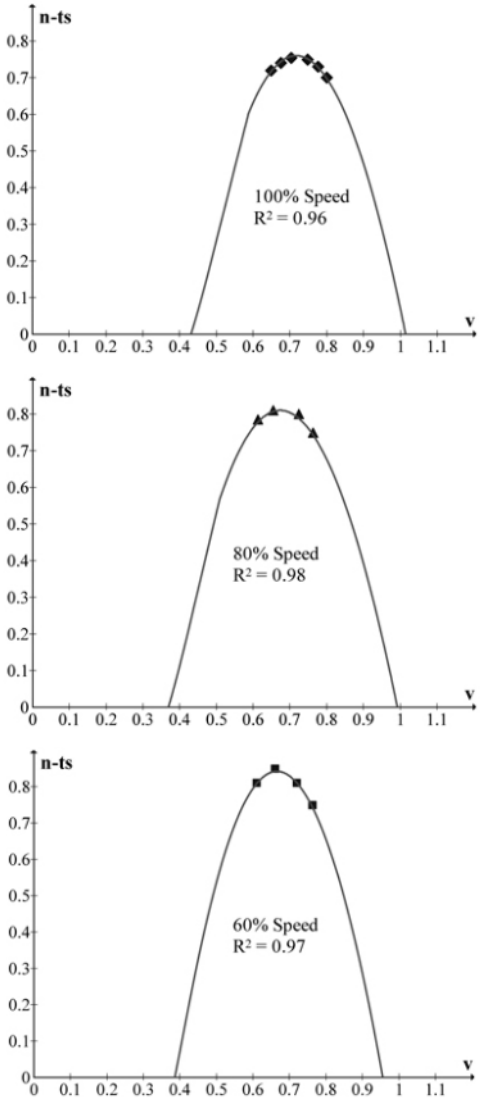

Figure 8. Efficiency extension for single stage commercial radial turbine (U_1* = 100%, 80% and 60%)

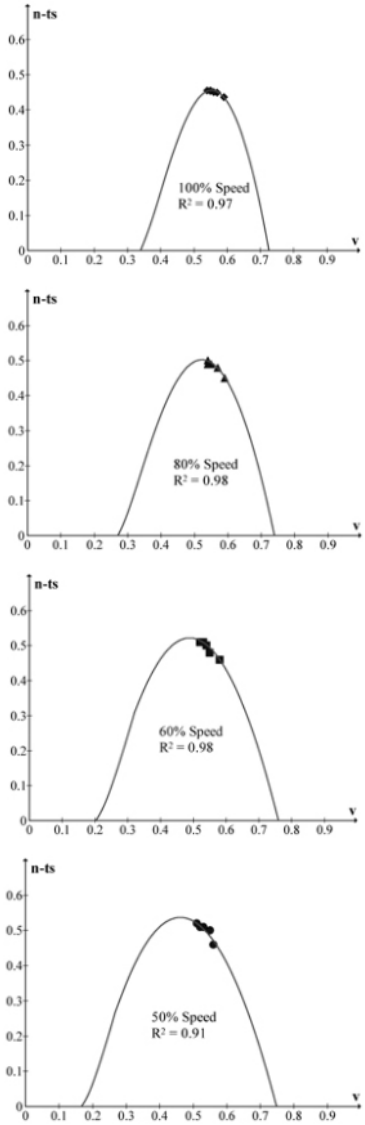

Figure 9. Efficiency extension for passenger car turbocharger radial turbine (U_1* = 100%, 80%, 60% and 50%)

DISCUSSION OF EFFICIENCY EQUATION

It is interesting to note that the efficiency is zero at a blade to jet speed ratio different than zero. This is due to these are curves at constant corrected speed (U_1*). They would have passed by zero point if they had been curves at constant expansion ratio (as discussed when equation (23) was explained). Nevertheless, as U_1* is constant the only way to make υ equal to zero is with C_S infinitum, i.e. with ER infinitum. Figure (10) shows the relationship between υ and ER. It is clear that υ decreases when ER increases but even for significant high values of ER the blade to jet speed ratio

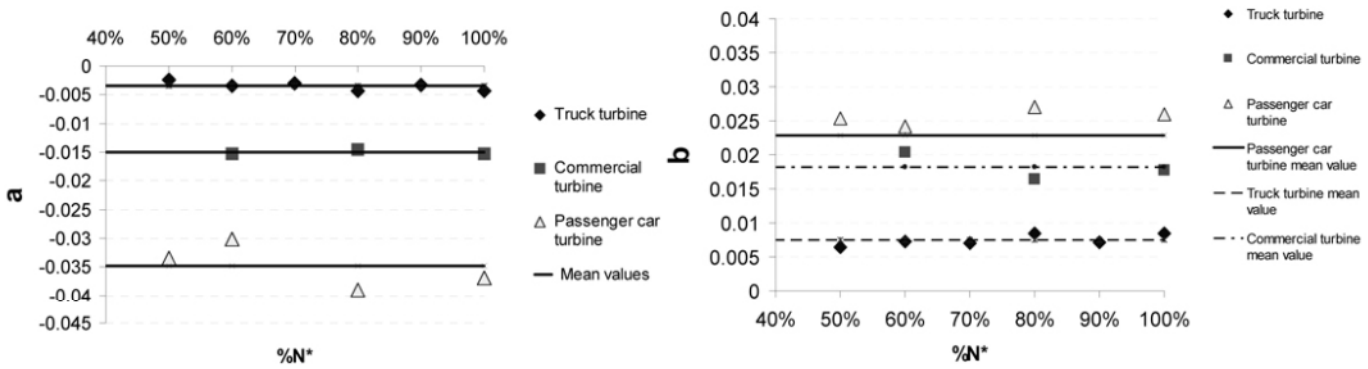

Figure 11. Trends in the 'a' and 'b' constant from the A_{eff} equation (33)

do not achieve a value of zero. It goes to zero asymptotically and in a very slow way. It means that in the choked zone of the turbine (high increasing ER), the efficiency is expected to decrease to zero at a blade to jet speed ratio sensibly higher than zero, due to further increments of ER (i.e. υ reductions) the mass flow doesn't increase anymore, therefore actual power decreases dramatically with respect to isentropic power. Figure (10) also shows that high υ corresponds to very low ER. Hence, it is expected to have a zero efficiency point at a high blade to jet speed ratio. This is the point predicted in the curves from Figures (7),(8),(9).

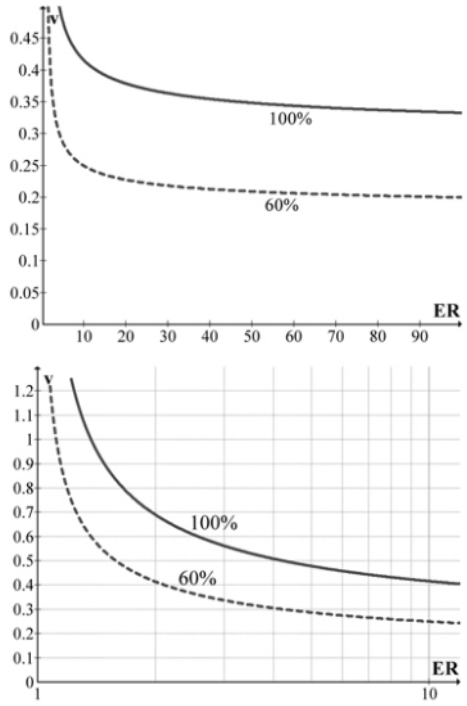

Figure 10. Blade to speed ratio versus ER for passenger car radial turbine (U_1* = 60% and 100%)

Figure (11) shows the trend in the coefficients presented into equation (33) for calculating A_{eff} it is observed that there is a small variability of all these coefficients which suggest that they are varying around representative values of that constants.

<figure 11 here>

The variations Aeff versus υ acording to equation (33) is shown in Figure (12). Figure (12) shows a thick-solid line computed from mean values shown in Figure (11) for every turbine. Figure (12) shows also a number of lines that correspond to the specific 'a' and 'b' coefficients for every turbo speed. A_{eff} is not plotted below a certain value of υ due to choked flow conditions. This value has been calculated from equation (34), this equation has been developed following two nozzles in series hypothesis [11]; i.e. equation (34) represents the square of the expansion ratio for a nozzle choked flow (ER_c). Therefore, when such $(ER_{MAX})_c$ is reached flow must be choked.

$$\left(\frac{1}{ER_{MAX}}\right)_c = \left[\frac{1}{ER_c}\right]^2 = \left[\left(\frac{2}{\gamma+1}\right)^{\frac{\gamma}{\gamma-1}}\right]^2 = \left(\frac{2}{\gamma+1}\right)^{\frac{2\gamma}{\gamma-1}} \qquad (34)$$

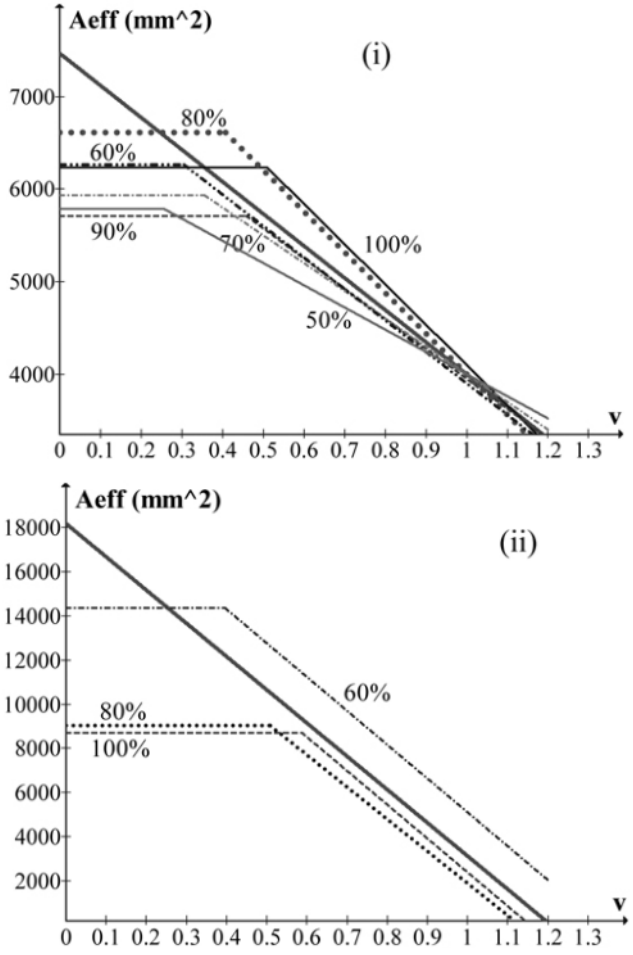

Figure 12. Effective area variation for the truck turbocharger turbine (i) and commercial turbine (ii)

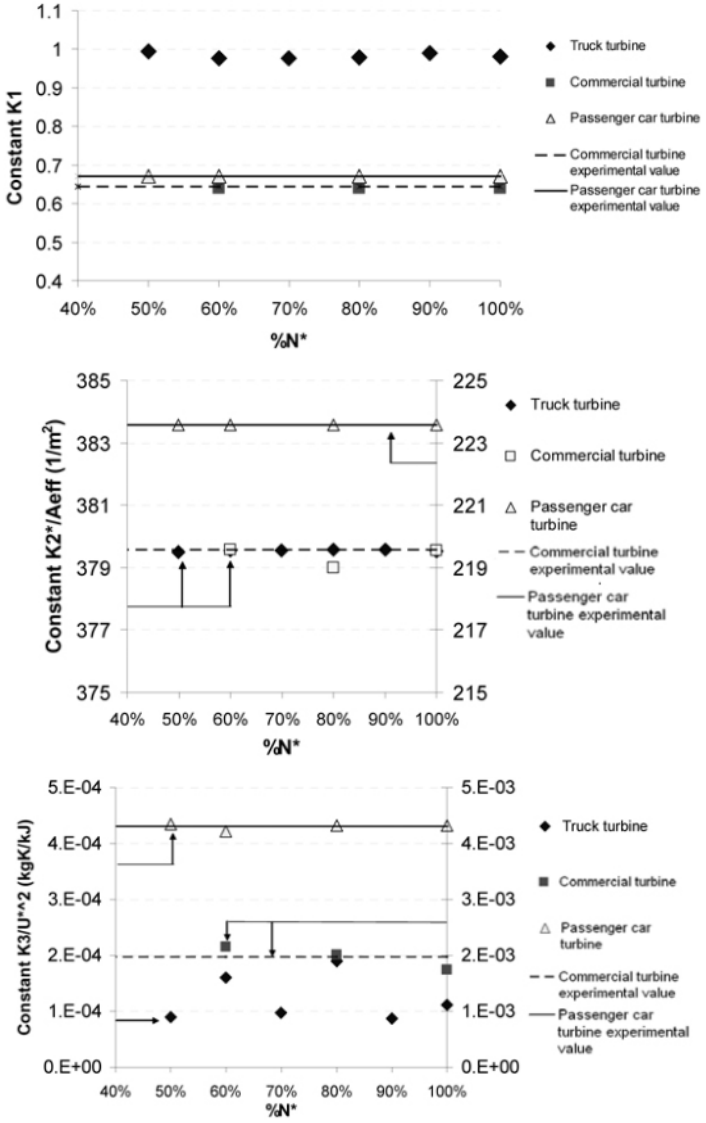

Figure 13. Model prediction of the constants from Table 1 *corresponding to efficiency* equation (29)

Figure (13) shows how the constants of equation (29) that have been obtained from the statistical procedure of fitting equation (29) to efficiency experimental data (Figure (7), Figure (8) and Figure (9)) are indeed values independent on turbocharger speed. In addition, Figure (13) shows a comparison between these constants from the fitting procedure and the experimentally obtained values shown in Table 1. These comparison provides consistency to model results.

MASS FLOW EXTENSION PROCEDURE

The procedure for the mass flow extension is based upon the definition of the specific speed:

$$SD = \frac{2r_1 \cdot \Delta h_0^{\frac{1}{4}}}{\sqrt{V}} = \frac{\left[2r_1\left[c_p \cdot \eta_{ts} \cdot T_{00}\left(1-\left(\frac{P_2}{P_{00}}\right)^{\frac{\gamma-1}{\gamma}}\right)\right]^{\frac{1}{4}}\right]}{\left(\frac{\dot{m}}{\rho_{00}}\right)^{\frac{1}{2}}} \quad (35)$$

The total enthalpy change across the stage has been treated using the definition of the total to static efficiency shown in equation (7). The volumetric flow can be converted into corrected mass flow via:

$$\sqrt{\frac{\dot{m}}{\rho_{00}}} = \left(\frac{\dot{m}}{\rho_{00}}\right)^{\frac{1}{2}} = \dot{m}^{*\frac{1}{2}} \cdot T_{00}^{\frac{1}{4}} \cdot R^{\frac{1}{2}} \quad (36)$$

Thus combining equations (35) and (36) and operating:

$$SD = \frac{\left[2r_1\left[c_p \cdot \eta_{ts} \cdot \left(1-\frac{1}{ER^{\frac{\gamma-1}{\gamma}}}\right)\right]^{\frac{1}{4}}\right]}{\sqrt{\dot{m}^*} \cdot \sqrt{R}} \quad (37)$$

This is an expression of the specific diameter as a function of the relevant turbine variables. Dividing and multiplying equation (37) by $[1/ER]^{\frac{\gamma-1}{4\gamma}}$:

$$SD = \frac{\left[2r_1\left[c_p \cdot \eta_{ts} \cdot \left(1-\frac{1}{ER^{\frac{\gamma-1}{\gamma}}}\right)\right]^{\frac{1}{4}}\right]}{\sqrt{\dot{m}^*} \cdot \sqrt{R}} * \frac{\left[\frac{1}{ER}\right]^{\frac{\gamma-1}{4\gamma}}}{\left[\frac{1}{ER}\right]^{\frac{\gamma-1}{4\gamma}}} \quad (38)$$

By operating, equation (38) can be split into:

$$SD_A = \frac{2r_1\left[c_p \cdot \eta_{ts}\right]^{\frac{1}{4}}}{\sqrt{\dot{m}^*} \cdot \sqrt{R}} \cdot \left[\frac{1}{ER}\right]^{\frac{\gamma-1}{4\gamma}} \quad (39)$$

$$SD_B = \left[ER^{\frac{\gamma-1}{\gamma}} - 1\right]^{\frac{1}{4}} \quad (40)$$

As can be seen, specific diameter could be break down into two relevant functions, SDA and SDB. Rearranging function SD_A:

$$SD_A = \frac{\left[2r_1\left[c_p \eta_{ts}\left(\frac{1}{ER}\right)^{\frac{\gamma-1}{\gamma}}\right]^{\frac{1}{4}}\right]}{\dot{m}^{*\frac{1}{2}} \cdot R^{\frac{1}{2}}} \quad (41)$$

Taking into account equation (25) the function SD_A, as expressed in equation (41), can be plotted against blade jet to speed ratio. This has been done for several turbines including all the speed range of the truck turbocharger radial turbine shown in Figure (2). This turbine has the property of having a well extended turbine experimental data. The results for this turbine are illustrated in Figures (14). The other two turbines are shown in Figures (15) and (16).

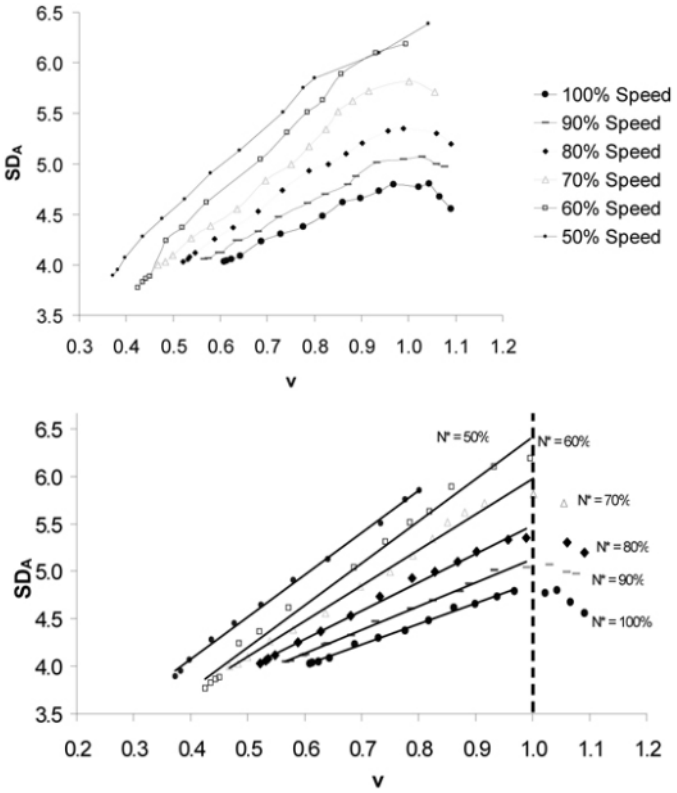

Figure 14. Fit for SD_A vs. v for the truck turbocharger radial turbine

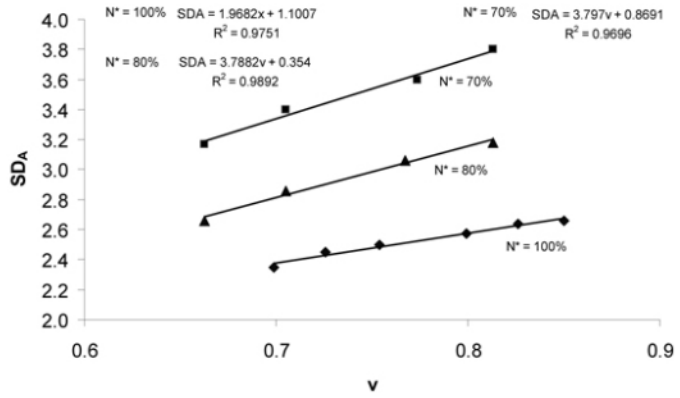

Figure 15. SD_A vs. υ for the single stage commercial radial turbine

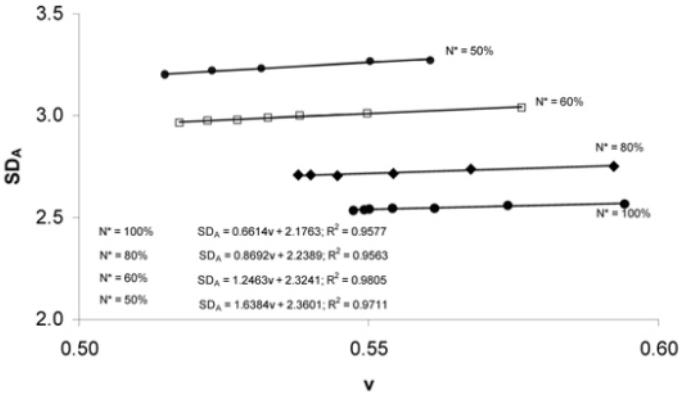

Figure 16. SD_A vs. υ for the passenger car turbocharger radial turbine

Figures (14),(15),(16) show an almost linear trend between function SD_A and the blade to jet speed ratio for a wide operative range of this variable. This is supported in the fact that efficiency maps use to be between υ = 0 and υ = 1.2 [1,2]. Therefore, a linear fit should be sufficient for representing this trend with a functional accuracy. The behavior pointed out by the SD_A function is useful in the further analysis of equation (41). Providing that SD_A correlates well with blade to jet speed ratio and therefore to the expansion ratio, and that a relationship between turbine efficiency and expansion ratio is already known as in equation (29), equation (41) shows that it is possible to find the values for the corrected mass flow corresponding to the extended efficiency map. Figure (17) shows this procedure. This procedure has been applied to the example turbines described in order to get the corrected mass flow extended map. The results of the extension of these curves are shown in Figures (18) (19) and (20) for selected turbine speeds.

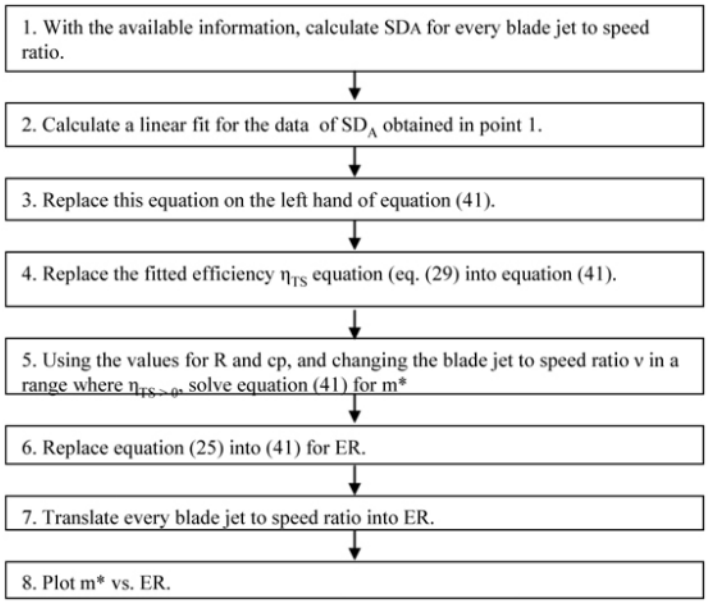

Figure 17. Procedure for corrected mass flow extension

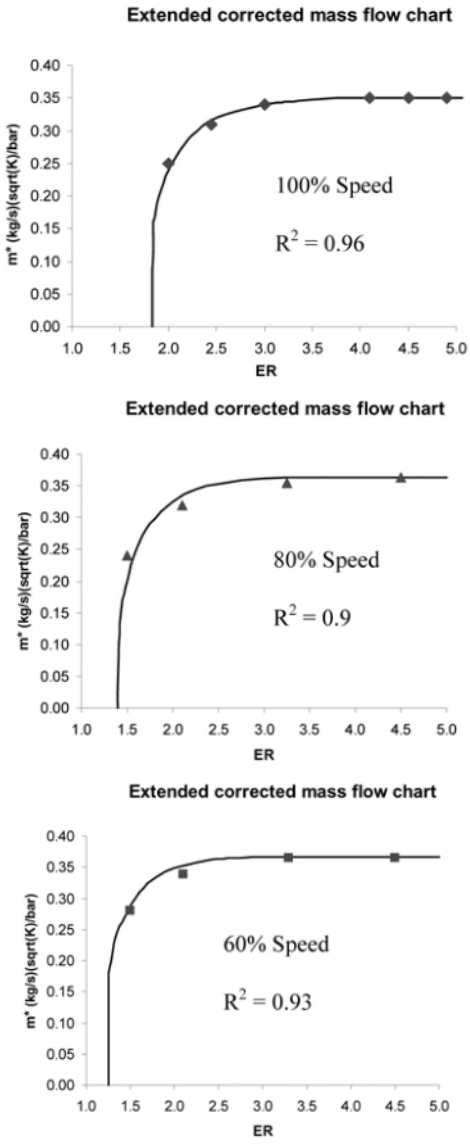

Figure 18. Corrected mass flow for single stage commercial radial turbine (U_1 = 100%, 80% and 60%)*

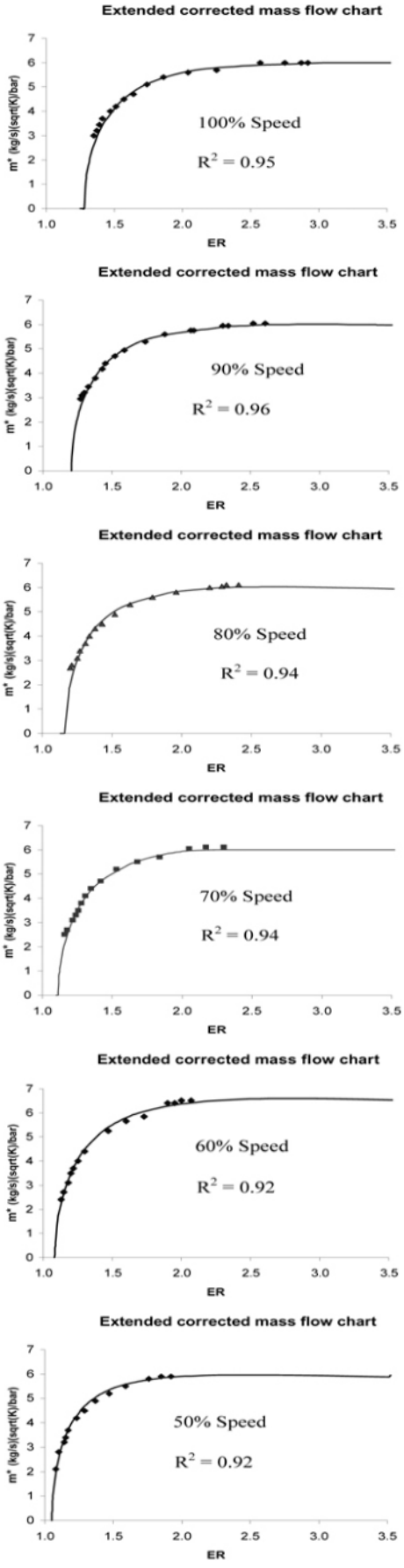

Figure 19. Corrected mass flow for truck turbocharger radial turbine (U_1 from 100% to 50% every 10%)*

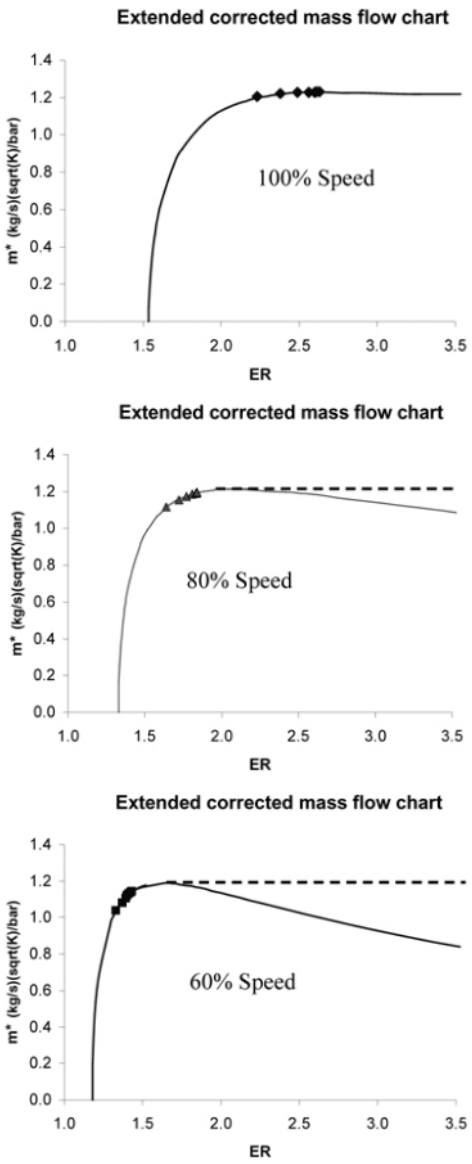

Figure 20. Corrected mass flow for passenger car turbocharger radial turbine (U_1* = 100%, 80%, and 60%)

DISCUSSION OF MASS FLOW EXTENSION PROCEDURE

A good initial estimation of the extended maps must rely on the less required information for getting the new one. This is because the simplicity of the method would be diminished if it is necessary to make a lot of measurements directly in the turbine. In this way, the model requirements would be comparable to those found in mean line thermodynamic models and the usefulness of the estimation method would be less.

Thus, the methodology exposed only relies on the information contained into the turbine maps which have been thoroughly used and, via equation (41), to the rotor tip diameter and two constants depending on the gas conditions, namely, the specific heat at constant pressure and the gas constant. This makes the method to work as a good initial quick estimation of the extended turbine maps.

One important aspect to note is the intrinsic physical base of the equations developed to provide a way for executing the extrapolation of the maps. Some authors [1,2] have followed the path of using only mathematical functions to fit the efficiency and mass flow curves in order for the turbine simulation to run off. It should be a simply approach to the modeling task but there is a lack of confidence that the data outside the boundaries of the experimental data get close to the reality due to the lack of physics behind the procedure. As it has been shown, the mathematical curves involved in the methodology outlined have been derived from physical equations which represent an aspect of the real behavior and characterization of radial turbines. They involved the definition, among another, of total to static efficiency, specific diameter, blade jet to speed ratio and the extensive use of the triangles of velocities. This approach gives a good estimation of the extended data in the maps. The methodology also has been applied to three different size turbines and for three different applications and the results seems to be not affected by this fact.

The linearity of the function SDA cannot be assured in the whole turbine operative range (as shows truck turbine experimental data for values of υ>1). Assuming a linear behavior down the lower values of υ may cause that the choke line in the extended mass flow map decreases with a negative slope. In this case, the last corrected mass flow value before this behavior appears is taken into account to construct a horizontal line which chokes mass flow for the subsequent expansion ratios. It has been checked that ER of such choking conditions are below the values predicted by equation (34). On the other hand, for the higher boundary and if enough experimental points are available, Figures (12) show that a linear trend with a negative slope begins to develop after υ=1. Using this behavior for the extended mass flow map extension makes that the mass flow curve falls almost vertically at the lowest expansion ratios.

SUMMARY/CONCLUSIONS

A procedure for the extrapolation of the radial turbine maps has been presented. It has been addressed that one the main problems in turbine modeling is the absence of the ability to simulate the behavior of the system for conditions outside the data that has been measured in the turbine maps. A need for a method capable for extrapolating the turbine maps was pointed out and a specific methodology for the accomplishment of this task was developed.

Expressions for extrapolation of the turbine maps, either efficiency and corrected mass flow, have been developed. They were derived using physical based equations to characterize the nature of the turbine. A fit of these expressions was carried out to the data contained in the turbine maps to get their extension to a range of operation where the experimental data do not exist.

Results were compared against experimental information and it was found that there is a good agreement between theoretical and test data. This methodology of getting the extended turbine maps is useful to get a quick estimation of the unknown data and for being implemented into turbine simulation codes. For future work it also will be important to test the methodology in an overall turbine simulation and compare proposed extrapolation predictions with measurements at very low or zero power turbine operative conditions.

REFERENCES

1. Watson, N., Janota, M.S., Turbocharging the Internal Combustion Engine, MacMillan Publishers LTD, London, ISBN 0 333 24290 4, 1982.

2. Baines, N., Moustapha H., Zelesky, M., Japikse, D., Axial and Radial Turbines, Concepts NREC, Vermont, ISBN 0 933283 12 0, 2003.

3. Dale, A.P., "Radial, vaneless, turbocharger turbine performance," Ph.D. thesis, Imperial College, London, UK, 1990.

4. Szymko, S., "The development of an eddy current dynamometer for evaluation of steady and pulsating turbocharger turbine performance," Ph.D. thesis, Imperial College, London, UK, 2006.

5. Winterbone, D.E., Nikpour, B., Alexander., G.I., "Measurement of the performance of a radial inflow turbine in conditional steady and unsteady flow," c405/015. Turbocharging and turbochargers, IMechE, 4th:153-162, 1990.

6. Nikpour, B., "Measurement of the performance of a radial inflow turbine," Ph.D. thesis, UMIST, Belfast, UK, 1990.

7. Arcoumanis, C., Hakeem, I., Khezzar, L., Martinez-Botas, R.F., Baines, N., "Performance of a mixed flow turbocharger turbine under pulsating flow conditions," ASME International gas turbine and aeroengine congress and exposition, (95-GT-210), June 1995.

8. Serrano, J.R., Guardiola, C., Dolz, V., Tiseira, A. et al., "Experimental Study of the Turbine Inlet Gas Temperature Influence on Turbocharger Performance," SAE Technical Paper 2007-01-1559, 2007.

9. Benson, R.S., The thermodynamics and gas dynamics of internal-combustion engines, vol. I, Oxford University Press, Oxford, ISBN 0 19 856210 1, 1982.

10. Payri, F., Benajes, J., Reyes, M., "Modelling of supercharger turbines in internal combustion engines," Int J Mech Sci. 8-9:853-69, 1996.

11. Serrano, J.R., Arnau, F.J., Dolz, V., Tiseira, A., Cervelló, C., "A model of turbocharger radial turbines appropriate to be used in zero- and one-dimensional gas dynamics codes for internal combustion engines modelling," Energ Convers Manage, 2008,.

12. Martínez-Botas, R.F,. Proceedings of the 8th International Conference on Turbochargers and Turbocharging. "Turbocharger Trends and Requirements Forum", London, 15-18 May 2006.

13. Szymko, S., McGlashan, N. R., Martinez-Botas, R., and Pullen, K. R., "The development of a dynamometer for torque measurement of automotive turbocharger turbines," Proceedings of the Institution of Mechanical Engineers, Part D (Journal of Automobile Engineering), Vol. 221, No. D2, 2007, pp. 225-239.

14. Futral, S. M., Wasserbauer, C. A., "Off-design performance prediction with experimental verification for a radial-inflow turbine," NASA Technical Report TN D-2621, 1965.

15. Heywood, J., Internal Combustion Engine Fundamentals, McGraw-Hill Science/Engineering/Math, ISBN 0 07 028637 X, 1988.

16. Muñoz, M., Payri, F., Motores de Combustión Interna Alternativos, Sección de Publicaciones de la E.T.S. de Ingenieros Industriales Fundación General - U.P.M, Madrid, ISBN 84 86043 01 9,1989

17. Zinner, K., Supercharging of Internal Combustion Engines, Springer-Verlag, New York, ISBN 3 540 08544 0,1978.

CONTACT INFORMATION

Dr. José Ramón Serrano
jrserran@mot.upv.es
Universidad Politécnica de Valencia. CMT-Motores Térmicos
Camino de Vera s/n. 46022 Valencia. Spain
phone: +34 96387 9657.
fax: +34 96387 7659

ACKNOWLEDGMENTS

Authors wish to thank the economical support of this work to Spanish Grant TRA2007-65433/TAIR from Ministerio de Educación y Ciencia. D.G. Investigación.

DEFINITIONS/ABBREVIATIONS

A	Area	m^2
c	Specific heat	J/kgK
C	Absolute velocity	m/s
ER	Expansion ratio	
h	Enthalpy	J/kg
$\dot{m}$	Mass flow	kg/s
$\dot{m}^*$	Corrected mass flow: $\dot{m}\left(\sqrt{T_{00}}/p_{00}\right)$	$(kg/s)\left(\sqrt{T}/p\right)$
p	Pressure	Pa
r	Rotor radius	m
R	Ideal gas constant (also indicates rotor relative conditions)	J/(kgK)
T	Temperature	K
U	Blade tip velocity	m/s
U*	Corrected blade tip velocity	$(\mathrm{m/s})/\sqrt{\mathrm{T}_{00}}$
$\dot{V}$	Volume flow	m^3/s
W	Relative velocity	m/s
$\dot{W}$	Power	Watt

Greek letters

α	Absolute gas angle	rad
β	Relative gas angle	rad
η	Efficiency	
θ	Tangential component	
ρ	Gas density	kg/m^3
γ	Ratio of specific heats	
ν	Blade jet to speed ratio	
ω	Turbine speed	rad/s
ω*	Corrected turbine speed: $\omega/\sqrt{T_{00}}$	$(\mathrm{rad/s})/\sqrt{\mathrm{T}_{00}}$
Δ	Change	

Subscripts

0	Stagnation conditions (also indicates stator inlet conditions)
1	Conditions at the rotor inlet
2	Conditions at the rotor exit
c	Constant pressure (also indicates choked flow conditions)
eff	Effective
s	Isentropic conditions
ts	Total to static conditions

ISSN 0148-7191

doi:10.4271/2010-01-1234

SAE Customer Service:
Tel: 877-606-7323 (inside USA and Canada)
Tel: 724-776-4970 (outside USA)
Fax: 724-776-0790
Email: CustomerService@sae.org
SAE Web Address: http://www.sae.org
Printed in USA

ANEXO III: A PHYSICAL MODEL BASED METHODOLOGY TO EXTRAPOLATE MAPS OF EFFICIENCY AND CORRECTED MASS FLOW FROM RADIAL TURBINES OF THE TYPE USED IN TURBOCHARGERS

A physical model based methodology to extrapolate maps of efficiency and corrected mass flow from radial turbines of the type used in turbochargers

F. Payri, J.R. Serrano*, R. Gozalbo and D. Ospina

Universidad Politécnica de Valencia. CMT-Motores Térmicos.
Camino de Vera, s/n. 46022. Valencia, SPAIN.

ABSTRACT

This paper details a physical based methodology to perform an extension of the radial turbine performance maps, both mass flow characteristics and the efficiency curve. This method takes into account a narrow range of experimental data, which is usually the data available when such turbines are part of a turbocharger. The nozzle equation is used to develop an interpolation and extrapolation of the mass flow rate trough the turbine. Then, specific information is extracted from this extrapolation and is fed into a total to static efficiency equation to carry out an extension of the efficiency curve. This equation is developed using the definition of the total to static efficiency, velocity triangles and thermodynamic and fluid fundamental equations.

This procedure has been applied to five radial turbines of different sizes and types. Results are compared against experimental information available in the literature or provided by the turbine manufacturers and a good agreement has been found between theoretical and experimentally estimated data.

Keywords: Turbochargers, radial turbines, efficiency and mass flow rate maps extrapolation, physical models based extrapolation.

*Contact author:
@mail: jrserran@mot.upv.es
Phone:+ 34 96 387 96 57 Fax:+ 34 96 387 76 59

DEFINITIONS, ACRONYMS, ABBREVIATIONS

A	Area (m^2)
C_p	Gas specific heat at constant pressure (J/kgK)
C	Absolute velocity (m/s)
ER	Expansion ratio
ER^*	Expansion ratio at choked flow conditions
h	Enthalpy (J/kg)
k_i	Equation (3) coefficients
k', k''	Equation (19) coefficients
K_i	Equations (23,27 and 32) coefficients
$\dot{m}$	Mass flow (kg/s)
$\dot{m}^*$	Corrected mass flow ($kg/s \times T^{0.5}/Pa$): $\dot{m}\left(\sqrt{T_{00}}/p_{00}\right)$
p	Pressure (Pa)
r	Rotor radius (m)
R	Ideal gas constant (J/kgK)
T	Temperature (K)
U	Blade tip velocity (m/s)
U^*	Corrected blade tip velocity ($m/s \times T^{0.5}$): $U/\sqrt{T_{00}}$
W	Relative velocity (m/s)
$\dot{W}$	Power

Greek symbols

α	Absolute velocity gas angle
β	Relative velocity gas angle
η	Efficiency
θ	Tangential component
ρ	Gas density (kg/m^3)
γ	Ratio of specific heats
ν	Blade to jet speed ratio
ν^*	Blade to jet speed ratio at choked flow conditions
Δ	Change

Subscripts and superscripts

0	Stagnation conditions (also indicates inlet turbine conditions)
1	Conditions at the rotor inlet
2	Conditions at the rotor exit
c	Choked flow conditions
$*$	Choked flow conditions with ER and ν. Corrected conditions with U and $\dot{m}$
eff	Effective
s	Isentropic conditions
ts	Total to static process

1. INTRODUCTION

A way to characterize the performance of a radial inflow turbine widely used in a turbocharger is via a turbine map. Turbine maps usually are presented using two separate plots: one for the mass flow rate and one for the energy conversion efficiency, which usually is taken as the total to static efficiency. The former chart is presented as the corrected mass flow ($\dot{m}^*$) as a function of the total to static expansion ratio (ER). The corrected mass flow ($\dot{m}^*$) is defined as the mass flow rate multiplied by a ratio between the square root of the turbine total inlet temperature and the turbine total inlet pressure 0. The other chart is the total to static efficiency (η_{ts}) as a function of the blade to jet speed ratio (υ), which is a ratio of the rotor tip linear velocity to the isentropic velocity through the turbine stage, for different turbine rotational speeds 0.

Data for constructing this kind of maps is taken from experiments carried out in special test rigs constructed for this purpose. Dale [2] used a test facility built at Imperial College to conduct research on unsteady flow in radial turbines. Winterbone et al. [3] and Nikpour [4] also designed a facility and used a hydraulic dynamometer in order to perform torque measurements. Arcoumanis et al. [5] used a radial compressor instead of a dynamometer to enable increased power of larger turbines to be absorbed. Szymko [6] developed an installation where an eddy current dynamometer was used in order to absorb the power of the turbine and for providing a low known inertia of the rotating assembly, which increases the measurement accuracy of the instantaneous torque. In the continuous flow test bench at *Universidad Politécnica de Valencia*, the approach is to use a compressor as a braking device [7]. In this last case, a collection of only a narrow range of data is possible, due to the surge and choke limits of the compressor, so a limited widespread of the data is available for constructing the aforementioned turbine maps. Nevertheless, this is a common situation for most of the maps provided by the manufacturers of the turbochargers used in automotive industry. Also, this is standard technique for the OEMs [8][9] of the automotive

industry to characterize turbine maps using the whole turbocharger assembly, due to avoids using special devices of specific knowhow for disassembling, balancing and reassembling the turbine to specific brakes that in the other hand are not commercially available.

In addition, new advancements in engine technologies are pushing the limits of operation for turbochargers to low expansion ratios, which in turn brings the analysis of turbine phenomena to higher blade to jet speed ratios [10]. In this region, it is important to have at one's disposal estimations of turbine efficiency; since it gives the possibility to run reliable full engine simulations, this is one of the main reasons stated by Martin et al. [11] to look for techniques to extrapolate turbochargers maps. This is necessary even when specific turbine models -such as those developed by Benson [12], Payri et al. [13] and Serrano et al. [14]- are used for solving boundary conditions in engine simulation codes, since this kind of models need to be calibrated against a complete enough set of experimental information. Having a method which allows estimating the efficiency in regions where there is no experimental data available is a tool which would help in the improvement of engine analysis and prediction of their operational characteristics. As deducted from the works of Katrasnik [15][16] in advanced engine concepts like hybrids the available 1D models will benefit from more robust physical based methodologies to turbine maps extrapolation.

This paper proposes a methodology for the accomplishment of turbine maps interpolation and extrapolation based on physical concepts. This will help to solve the lack of turbine data at off design operative conditions.

Typical radial turbine maps are shown in figure 1 and figure 2 for the five turbines used in this work. These five turbines are taken as examples for the application of the methodologies and equations presented in this paper. Figure 1 shows three vaneless stator radial turbines' performances maps. For the large size truck turbine information was taken from "Turbo trends and requirements forum" of the 8th International Conference on Turbochargers and Turbocharging [17] (figure 1A) and it was tested in the rig developed by Szymko [6]. The medium and small size turbochargers are

also radial, vaneless stator turbines that have been used in a truck engine, as low and high pressure turbines respectively, in a two stage system. The maps for these turbines are shown in figures 1B and 1C and were obtained from the turbochargers manufacturer who tested them in a hydraulic brake test rig for turbine characterization. It can be highlighted that while Figure 1A data was measured at constant turbine corrected speed, Figure 1B and 1C data was measured at constant turbine expansion ratio. Figure 2 shows two turbines with nozzles in the stator. The first one (figure 2A) is a single stage commercial radial inflow turbine used for an analysis carried out by Futral [18] and its main application is the development of power for space applications. The second turbine (figure 2B) is from a turbocharger of a passenger car engine. It is a small variable geometry turbine, with uncambered airfoil section nozzles, which has been tested at *Universidad Politécnica de Valencia* turbochargers test rig [7].

Detailing paper contents, first a method for the extrapolation of the mass flow chart is proposed based on the nozzle equation (1).

$$\dot{m}^* = A_{eff}\gamma\left(\frac{1}{ER}\right)^{\frac{1}{\gamma}}\sqrt{\frac{2}{\gamma-1}\left[1-\left(\frac{1}{ER}\right)^{\frac{\gamma-1}{\gamma}}\right]} \quad (1)$$

The turbine stages are idealized as a single nozzle and a fit of this equation to the mass flow experimental data is carried out to obtain an estimation of the throat effective area variation for different blade to jet speed ratio values. In turn, this estimation allows an extrapolation of the mass flow to unknown values of expansion ratio using the same equation. Physical explanation of this behaviour and validation of the procedure for different turbines is provided in section 2. A method for extrapolating the efficiency curve is proposed based on an equation developed from physical principles which involves the definition of total to static efficiency, the velocity triangles for the stage and the thermodynamic behaviour of the flow. It is important for this expression to be a function of the blade jet to speed ratio and some intrinsic data related to any loss mechanisms,

geometrical and gas properties, so the turbine can be correctly characterized and the extrapolation can be carried out. The details of the efficiency equation derivation from basic equations are provided in section 3. This equation and the proposed extrapolation procedure are validated with the five different turbines mentioned before: One turbocharger turbine for a passenger car, a set of three turbines composed of a large, a medium and a small size truck turbocharger and a commercial radial inflow turbine for power generation. Details and charts showing validation process results are provided along section 3. Section 4 provides a discussion of the procedure for experimental data extrapolation, where the fitting constants of efficiency equation are analysed and checked against control values. Finally, section 5 is devoted to highlight the main conclusions from the paper.

2. EXTENSION OF TURBINES CORRECTED MASS FLOW MAP

The procedure for the extension of the mass flow map is based mainly on the definition of the subcritical corrected mass flow through the orifice of a single isentropic nozzle. Equation (1), previously introduced, explains the flow behaviour in this situation, a formal demonstration of this expression can be found in the appendix of reference [19]. Some authors have attempted to model the turbine as a single nozzle with some success, for example Watson 0 and Benson [12], and the same basic approach is followed here, but taking into account the possibility for the effective flow area (A_{eff}) to be variable instead of a constant value in equation (1). This fact will be shown later. Now, considering the corrected mass flow charts described in Figures 1 and 2 and the turbine modelling approach as a single nozzle, it is possible to say that equation (1) represents the mathematical relationship between the corrected mass flow and the expansion ratio plotted in the charts. That is, providing that gas properties are known (i.e. gamma) and the variation of A_{eff} is also known for every ER, then it would be possible to plot the entire mass flow curve for any point of operation.

Therefore, the objective will be to estimate A_{eff} as a function of turbine operative conditions. Equation (1) can also be used to find an indirect operational relationship between A_{eff} and these conditions; i.e. Total to static ER, the corrected speed (U*) or the blade to jet speed ratio (υ).

Taking into account the definition of blade to jet speed ratio given in equation (2) and turbine experimental data, which in this case is the corrected mass flow, the expansion ratio and the gas properties; it is possible to calculate the blade to jet speed ratio for every tested point.

$$\upsilon = \frac{U}{C_s} = \frac{U^*}{\sqrt{2c_p\left(1-\left(\frac{1}{ER}\right)^{\frac{\gamma-1}{\gamma}}\right)}} \tag{2}$$

Indeed, for every experimental point of operation there are known values of ER and U*. Providing that the basic gas properties (i.e. gamma and c_p) are also known, the related blade to jet speed ratio can be obtained via equation (2).

In the case of turbines tested at constant U* lines (like the results shown in figure 1A, for the large size truck turbine, and in figure 2, for the commercial and passenger car turbines) it is quite convenient to plot the effective area A_{eff} as a function of the blade to jet speed ratio since a strong linear trend is obtained. This is clearly shown in figure 3 where A_{eff} for the large size truck turbine has been plotted, in a dimensionless format, as a ratio with the turbine volute inlet section (A_0). The wide operative range of υ that has been able to be measured, thanks to Szymko device [6], in the case of the large size turbine (figure 1A and figure 3) guarantees the accuracy of this lineal trend. Similar trends were also found by other authors; Zinner [20] proposed direct relationships between A_{eff} and ER for a constant turbocharger speed and Muñoz et al. [21] proposed a linear approximation for Zinner relationships. Figure 4 shows also linear trends for the commercial and the passenger car turbines whose maps are shown in figure 2. The narrower operative range tested for the passenger car turbine is a drawback as very few points are available for the extrapolation.

Nevertheless, the consistent linear trend showed for the wider operative ranges tested with the other two turbines, used to exemplify this phenomenon, allows trusting in the linear trends shown in figure 4B.

On the other hand, when the turbines are characterized at constant expansion ratio, such as the medium and small truck turbines (figure 1B and 1C), this trend changes and becomes quadratic, as it is shown in figure 5. This is not surprising since due to the different testing procedure (at constant ER instead of at constant U*) the operative conditions in the turbine are intrinsically different. Indeed, figure 5 shows that A_{eff} decreases at constant expansion ratio (attending to equation (2) C_s would be constant in these conditions) when turbocharger speed increases. This behaviour is a consequence of the centrifugal force field created by the rotor of the radial turbine 0. Such a field reduces the mass flow through the turbine for a given expansion ratio (figures 1A and 1B), therefore the virtual nozzle that reproduces turbine mass flow behaviour must show a decreasing trend in the A_{eff} to A_0 ratio. Finally, the decreasing trend shown in figure 5 is quadratic due to the centrifugal forces are proportional to the square of the corrected speed [10].

Nevertheless, it would be expected that independently on which variable has been hold constant during turbine testing (U* or ER) the same type of function could relate A_{eff} to A_0 ratio with turbine operative variables. In addition, from figures 3, 4 and 5 it seems that A_{eff} to A_0 ratio should be a function of both υ and U*. In this paper the relation shown in equation (3) is proposed:

$$\frac{A_{eff}}{A_0} = k_1 + k_2 \cdot \upsilon \cdot U^* + k_3 \cdot \upsilon + k_4 \cdot U^* \qquad (3)$$

Equation (3) has been obtained after exploring several possibilities and considering both the linear trend with υ and some quadratic behaviour with U*. The 'k_i' coefficients of equation (3) are listed in Table 1 together with the R^2 factor for the three vaneless stator truck turbine maps plotted in figure 1. Figure 6 shows graphically this relation for these three turbines. Since R^2 factor is so close

to one, it indicates a high level of correlation between A_{eff} to A_0 ratio and the two independent variables (υ and U*) with the proposed equation (3) structure. Figure 6 shows clearly the constant speed lines in the case of the large size truck turbine and also the previously stated linear behaviour with υ for this turbine. In addition, in the case of the medium and small size truck turbines figure 6 also shows the constant ER lines (from figures 1B and 1C) crossing diagonally the plane U*-υ. Since ER is not directly used as an independent variable of equation (3) the quadratic behaviour showed in figure 5 is now represented by the 'k_2' coefficient in equation (3). Such a quadratic behaviour can be clearly observed appearing in figure 6 as curved surfaces (since equation (3) is not the equation of a plane surface). Finally, it is worth highlighting that the 'k_i' coefficients show some clear trends with turbine size in the case of vaneless stator turbines, specially k_1 and k_2, as have been represented in the fourth column of Table 1.

Thus, equation (3) in conjunction with equations (1) and (2) are used to fit the experimental mass flow data and to perform an extrapolation of the mass flow map by using the following procedure:

1. Using the data available in the map, equation (1) and equation (2), A_{eff} for the experimental points can be calculated and plotted versus the independent variables (υ and U*).

2. Equation (3) is then used to fit the aforementioned calculated A_{eff} and values for the 'k_i' coefficients can be obtained.

3. Evaluating equations (1), (2) and (3) for a wide range of ER and/or U*, an extrapolation of the sub critical nozzle equation (1) that fits the experimental mass flow data can be carried out.

Because of the intrinsically sub critical condition of the nozzle equation (1), the mass flow never chokes [19]. Indeed, the curve begins to increase up to a certain ER* value and then decreases (figure 7). Obviously, this situation happens when the first derivative of equation (1) is zero. Once this point is reached, the corrected mass flow remains frozen and the corresponding ER* can be

considered the critical expansion ratio for which choked flow is achieved. Therefore, an extra step can be added to previous procedure:

4. When the first derivative of the sub critical nozzle expression, equation (1), is zero the turbine is choked and, from this point on (ER*), the corresponding value of corrected mass flow is kept constant as the ER is increased.

Results of such extrapolation procedure for the five example turbines are shown in figures 7 to 9. Figure 7 shows for the large size truck turbine the experimental points and in continuous line the results from the extrapolation. A dotted line is plotted just to show the non-physical behaviour of equation (1) after critical conditions are reached as well as to identify ER* conditions for every U*. In figure 8, dotted lines do not appear since ER* conditions have not been plotted. Finally, Figure 9 corresponds to the stator vaned turbines, and since measurements were performed at constant U* the same graphical code than in figure 7 has been used. It is worth clarifying that some experimental values taken from the commercial turbine analysis (figure 9A) correspond to mass flows values extracted directly from the curve shown in figure 1D because of the absence of more experimental information in this reference. In figure 9B the advantages presented by this extrapolation technique can be seen more clearly, taking into account the reduced amount of ER values available in the experimental points. The reduced range of ER is due to the fact that the turbine has been tested coupled with the compressor [7], and the compressor is the brake limiting turbine operative range, as it is currently done in any standard gas stand used for turbochargers testing [8].

3. EXTENSION OF TURBINES TOTAL TO STATIC EFFICIENCY MAP.

The task of extending the efficiency map must begin with the development of an efficiency equation based on the definition of total to static efficiency:

$$\eta_{ts} = \frac{h_{00} - h_{02}}{h_{00} - h_{2s}} = \frac{T_{00} - T_{02}}{T_{00} - T_{2s}} \tag{4}$$

The triangle of velocities for the analysis is presented in figure 10A and the enthalpy – entropy diagram for the turbine stage is also presented in figure 10B. Figure 10B shows total enthalpy and rothalpy points and it is also possible to observe the term corresponding to the rotor centrifugal force field (i.e.: $(U_1^2-U_2^2)/2$) that is proportional to the square of turbocharger speed, as discussed previously.

Taking into account the velocity triangles, it can be said that:

$$\tan\alpha_1 = \frac{C_{\theta 1}}{C_0} \Rightarrow C_{\theta 1} = C_0 \tan\alpha_1 \tag{5}$$

$$\tan\beta_2 = \frac{x}{C_0} \Rightarrow x = C_0 \tan\beta_2 \tag{6}$$

$$U_2 = x + C_{\theta 2} \Rightarrow C_{\theta 2} = U_2 - x \tag{7}$$

Recalling the general relationship between the lineal velocity and the rotational velocity and applying it to the rotor equation (8) is obtained. In equation (8), r_2 has been defined as the radius that separates in two equal parts the cross section between hub and shroud at turbine wheel outlet.

$$\frac{U_1}{r_1} = \frac{U_2}{r_2} \Rightarrow U_2 = U_1\left(\frac{r_2}{r_1}\right) \tag{8}$$

Combining equations (6) and (8) into (7):

$$C_{\theta 2} = U_1\left(\frac{r_2}{r_1}\right) - C_0 \tan\beta_2 \tag{9}$$

Recalling equation (4) and expanding it:

$$\eta_{ts} = \frac{h_{00} - h_{02}}{h_{00} - h_{2s}} = \frac{T_{00} - T_{02}}{T_{00} - T_{2s}} = \frac{T_{00} - T_{02}}{T_{00}\left(1 - \left(\frac{1}{ER}\right)^{\frac{\gamma-1}{\gamma}}\right)} \tag{10}$$

From the definition of power and Euler's equation of turbomachinery [10], it can be stated that:

$$\dot{W} = \dot{m} \cdot C_p \left(T_{00} - T_{02} \right) \tag{11}$$

$$\dot{W} = \dot{m} \left(U_1 C_{\theta 1} - U_2 C_{\theta 2} \right) \tag{12}$$

Combining (11) and (12):

$$T_{00} - T_{02} = \frac{U_1 C_{\theta 1} - U_2 C_{\theta 2}}{C_p} \tag{13}$$

Inserting equation (5), (8), (9) and (13) into (10) and arranging terms:

$$\eta_{ts} = \frac{U_1 C_0 \tan \alpha_1 - U_1 \left(\frac{r_2}{r_1} \right) \left[U_1 \left(\frac{r_2}{r_1} \right) - C_0 \tan \beta_2 \right]}{C_p \cdot T_{00} \left(1 - \left(\frac{1}{ER} \right)^{\frac{\gamma - 1}{\gamma}} \right)} \tag{14}$$

Defining C_s as proposed by Watson 0, i.e.: the velocity which would be attained if the turbine working fluid was expanded in an ideal nozzle over the same expansion ratio as that of the turbine (figure 10), then it can be written:

$$C_s^2 = 2 C_p \cdot T_{00} \left[1 - \left(\frac{1}{ER} \right)^{\frac{\gamma - 1}{\gamma}} \right] \tag{15}$$

Recalling equation (15), then equation (14) can be written as:

$$\eta_{ts} = \frac{-2 U_1^2 \left(\frac{r_2}{r_1} \right)^2 + 2 U_1 C_0 \left(\tan \alpha_1 + \left(\frac{r_2}{r_1} \right) \tan \beta_2 \right)}{C_s^2} \tag{16}$$

Recalling equation (2) and grouping into K_i coefficients:

$$\eta_{ts} = -K_1 \upsilon^2 + K_2 \upsilon \frac{C_0}{C_s} \tag{17}$$

where:

$$K_1 = 2 \left(\frac{r_2}{r_1} \right)^2 \qquad K_2 = 2 \left(\tan \alpha_1 + \left(\frac{r_2}{r_1} \right) \tan \beta_2 \right) \tag{18}$$

K_2 is further expanded as a function of υ assuming that the angle α_1 (figure 10) has a linear variation with the blade to jet speed ratio, as equation (19) shows where *k'* and *k''* are constants. This is proposed due to the strong dependence of α_1 flow angle on turbine operative conditions, especially in vaneless turbines 0. Nevertheless, it is expected a smooth angle variation with υ [18] so the constant *k'* should tend to small values near to zero and *k''* should tend to values near the geometric value of stator blades angle (in the case of turbines with vaned stator).

$$\alpha_1 = k'\upsilon + k'' \tag{19}$$

From here on, equation (17) will be used in a different way if the turbine tests have been performed at constant ER or at constant U*.

3.1. Constant Expansion Ratio Tests

It is necessary to find a relation between υ and term C_0/C_s in equation (17) in order to make it functional. One way to do that is firstly to replace directly the definitions of the velocities implied in this ratio. C_s has been already defined in equation (15), C_0 is the circulation velocity (figure 10) and can be found using the continuity equation:

$$C_0 = \frac{\dot{m}RT_0}{p_0 A_0} \tag{20}$$

Inserting equations (15) and (20) into C_0/C_s and solving for the mass flow:

$$\dot{m} = \left({}^{C_0}\!\!\diagup\!\!{}_{C_s} \right) \frac{p_0 A_0}{R_0 T} \sqrt{\gamma R T_{00}} \sqrt{\frac{2}{\gamma - 1}\left(1 - \left(\frac{1}{ER} \right)^{\frac{\gamma - 1}{\gamma}} \right)} \tag{21}$$

Recalling the equation (1) again, equating with equation (21) and solving for C_0/C_s:

$$\frac{C_0}{C_s} = \frac{A_{eff} p_{00} \gamma \left(\frac{1}{ER}\right)^{\frac{1}{\gamma}} RT_0}{p_0 A_0 \gamma R T_{00}} = \frac{A_{eff}}{A_0} \left(\frac{1}{ER}\right)^{\frac{1}{\gamma}} \left(\frac{T_0}{T_{00}}\right)^{\frac{1}{\gamma}} \quad (22)$$

For hot tests, usually T_0/T_{00} is close to one, so assuming this simplification and substituting equation (22) into (17), equation (23) is obtained:

$$\eta_{ts} = -K_1 \upsilon^2 + K_2 \upsilon \frac{A_{eff}}{A_0} \left(\frac{1}{ER}\right)^{\frac{1}{\gamma}} \quad (23)$$

A_{eff} to A_0 ratio is further expanded as a function of υ considering that the ratio comes from equation (3).

In equation (23) it is interesting to note that, providing that ER is a constant, the efficiency is zero at a blade to jet speed ratio equal to zero. Assuming a constant value of ER is only possible if the rotor tip velocity (U_1) is zero at this condition. This results in a turbine efficiency map crossing through the origin at zero blade to jet speed ratio for every constant ER curve, as it would be expected.

Therefore, equation (23) will be used for extrapolating and analyzing data which has been measured at constant expansion ratio, in this paper this correspond to the data of the small and medium size truck turbines. The results obtained from fitting equation (23) to measured data and extrapolating are shown in figure 12.A for the medium size truck turbine and figure 12.B for the small size truck turbine. Figure 12 in general shows a good accuracy between measured and calculated efficiency and also shows expected values of υ when extrapolating to zero efficiency values. It is worth noting that the ratio between A_{eff} and A_0 has been obtained using equation (3) and the values used are shown in the corresponding charts from figure 6.

3.2. Constant Corrected Rotor Tip Speed Tests

Nevertheless, it is normal practice (indeed easier if a turbine brake is not available) to measure turbocharger characteristics at constant corrected rotor tip speed rather than at constant ER.

Therefore, an expression with this variable as a constant will be necessary. Corrected rotor tip velocity of the turbine is defined as:

$$U_1^* = \frac{U_1}{\sqrt{T_{00}}} \tag{24}$$

Combining equation (24) with (2) and (15) and solving for 1/ER:

$$\left(\frac{1}{ER}\right) = \left[1 - \frac{U_1^{*2}}{2C_p \upsilon^2}\right]^{\frac{\gamma}{\gamma-1}} \tag{25}$$

Inserting (25) in (22):

$$\frac{C_0}{C_s} = \frac{A_{eff}}{A_0}\left[1 - \frac{(\gamma-1)U_1^{*2}}{2\gamma R \upsilon^2}\right]^{\frac{1}{\gamma-1}}\left(\frac{T_0}{T_{00}}\right)^{\frac{1}{\gamma}} \tag{26}$$

For turbine operative points located in a constant rotational speed line, U^*_1 is constant and for hot tests usually T_0/T_{00} is close to one. Therefore, turbine efficiency can be expressed just as a function of υ as equation (27) shows:

$$\eta_{TS} = -K_1 \upsilon^2 + K_2^*\left[1 - \frac{K_3}{\upsilon^2}\right]^{\frac{1}{\gamma-1}} \upsilon \tag{27}$$

Where K_1 has been already defined in equation (18) and K^*_2 and K_3 are defined as:

$$K_2^* = 2\frac{A_{eff}}{A_0}\left(\tan\alpha_1 + \left(\frac{r_2}{r_1}\right)\tan\beta_2\right) \tag{28}$$

$$K_3 = \frac{(\gamma-1)U^{*2}_1}{2\gamma R} = \frac{U^{*2}_1}{2Cp} \tag{29}$$

K_2^* expression is further expanded as a function of υ considering that A_{eff} to A_0 ratio comes from equation (3) and that the angle α_1 (figure 10) is a linear function of the blade to jet speed ratio, equation (19).Equation (27) has been applied to the turbine data, measured at constant U* and described in previous sections, in order to get the efficiency extended map. The results of the extension of these curves are shown (independently for every U^*_i) in figure 12 for the large size

truck turbine with vaneless stator and in figure 13 for the commercial type and passenger car turbines with nozzles in the stator. A good accuracy between measured efficiency and the values predicted by equation (27) has been obtained.

In order to get a general view of the entire turbine behaviour, the curves were extrapolated up to efficiency values near zero at both low and high υ limits. As figure 12 and figure 13 show, zero efficiency (at low υ values) is obtained at values of υ higher than zero. This is clear since U* is constant and therefore υ zero cannot be obtained at least C_s becomes infinitum. The same conclusion can be obtained from the mathematical structure of equation (27), i.e. at υ zero it is an undetermined equation.

Indeed, figure 12 and figure 13A show the υ* values at which choked flow is reached in the turbine [$\upsilon^*=(U/C_s)^*$] for every U*, from these points up to lower values of υ the efficiency should only decrease, as the extrapolation predicts. Nevertheless, such extrapolation at choked flow conditions is not performed using equation (27) as will be discussed in section 3.3.

3.3 Choked flow conditions

Since equations (23) and (27) are based in A_{eff} to A_0 ratio from equation (3), they are only valid if flow is not choked in the turbine. Therefore, a new expression is needed when dealing with chocked corrected mass flow ($\dot{m}_c^*$). Indeed C_0 for choked flow conditions can be written as:

$$C_0 = \frac{\dot{m}RT_0}{p_0A_0} = \frac{\dot{m}_c^*R\sqrt{T_0}}{A_0}\left(\frac{T_0}{T_{00}}\right)^{\frac{2-\gamma}{2\gamma}} \tag{30}$$

Considering equation (27), blade to speed ratio definition (2) and corrected tip speed definition (24) and solving for C_0/C_s it is possible to obtain such velocity ratio in choked flow conditions, as shows equation (31):

$$\left(\frac{C_0}{C_S}\right)_c = \frac{\upsilon}{U_1}\frac{\dot{m}_c^* R\sqrt{T_0}}{A_0}\left(\frac{T_0}{T_{00}}\right)^{\frac{2-\gamma}{2\gamma}} = \frac{\dot{m}_c^*}{U_1^*}\frac{R\upsilon}{A_0}\left(\frac{T_0}{T_{00}}\right)^{\frac{1}{\gamma}} \tag{31}$$

Therefore, assuming once again that for hot tests usually T_0/T_{00} is close to one, turbine efficiency for choked conditions can be expressed as:

$$\left(\eta_{ts}\right)_c = -K_1\upsilon^2 + K_2\upsilon^2\frac{\dot{m}_c^*}{U_1^*}\frac{R}{A_0} = \upsilon^2\left(K_2\frac{\dot{m}_c^*}{U_1^*}\frac{R}{A_0} - K_1\right) \tag{32}$$

Equation (32) has been used to predict and extrapolate decreasing efficiency at υ values beyond choked flow conditions in figures 12 and 13. No discontinuity with equation (27) is shown at initial choked flow point; moreover, the results predicted in figure 13.A show good accuracy with experimental data.

4. RESULTS DISCUSSION

Since equations (23), (27) and (32) are strongly non-linear with υ, moreover considering that equations (3) and (19) are embedded inside, the fitting procedure of these turbine efficiency equations to the experimental data must be done using a non lineal numerical method. Usually, when performing this kind of nonlinear statistical fitting, it is necessary to impose initial values to the equation constants and the obtained results are strongly dependant of the provided initial values.

For this reason, the initial values for the constants presented in the efficiency equations are collected from experimental information of the turbine geometry. These constants are: The ratio of turbine wheel radiuses for the K_1 coefficient -see equation (18)-, the turbine volute inlet section for the A_0 constant and the angle at the rotor blade outlet (the metal angle) for the β_2 constant (see equation (18) and figure 10).

Figure 14 shows, for the studied turbines, a comparison between the initial values provided to the non-linear fitting procedure (experimentally estimated) and the final values (theoretically calculated) obtained from the procedure as convergence results. These theoretically calculated constants are responsible of the accuracy shown from figure 11 to figure 13 between measured turbine efficiency data and calculated turbine efficiency from equations (23), (27) or (32). Considering the simplicity of the proposed model and the uncertainty in both turbine efficiency measurements and measurement of geometrical constants, it can be concluded that Figure 14 shows a good agreement between the constants that fit measured efficiency and the experimentally estimated values that has been initially provided. For the large size truck turbine, the experimentally estimated values plotted in figure 14 are just the average of the theoretically calculated ones; this has been done due to the absence of geometrical data in the bibliographical source [17].

Regarding K_3 constant from equation (27) and considering its definition in equation (29), it is clear that equation (33) is fulfilled:

$$\frac{K_3}{\left(U_1^*\right)^2} = \frac{1}{2 \cdot Cp} \tag{33}$$

Therefore, the result of applying equation (33) to the K_3 values (obtained from the non-linear fitting procedure) provides always a value of 0.498 kgK/kJ. As it would be expected, since the turbines tested at constant U* that have been described in this paper were tested with hot air at relatively low temperatures and in these conditions air heat capacity is around 1.004 kJ/kgK.

Finally, *k'* and *k''* constants from equation (19) provide a certain analysis of α_1 variation with υ. Figure 15 shows that there is a small variation of the angle for a wide range of υ as it was expected [18]. Figure 15.A shows the variation of α_1 with the blade to jet speed ratio for the studied turbine with vaned stator. Experimentally estimated values of stator blades α_1 angle (metal angle) are

shown in table 2. A reasonable agreement has been obtained between Table 2 data and the corresponding average α_1 values from Figure 15.A.

For the small and medium truck turbines, without stator blades, the α_1 values provided in table 2 has been theoretically estimated assuming momentum conservation in turbine volute and in the vaneless stator 0. A more significant discrepancy can be observed if the values from table 2 (60º and 62º respectively) are compared to those predicted by the non-linear fitting and shown in figure 15.B. In Figure 15.B the different expansion ratios are shown by the different symbol sizes, the higher is the expansion ratio, the bigger is the symbol. Nevertheless, this result does not diminish model accuracy since also according to Watson 0 a high variability of α_1 angle is expected for different operative conditions in vaneless stator turbine. The simple model presented in this paper averaged this variability with a α_1 angle that correctly fits the measured turbine efficiency data. For the large size truck turbine it has not been possible to perform a similar analysis due to the absence of geometrical data in the bibliographical source [17].

Finally, it is worth highlighting that the consistency in the analysis performed of the model constants (obtained from the non-linear statistical fitting of the results) provides an additional validation of the model reliability.

5. CONCLUSIONS

A procedure for the extension of both mass flow and efficiency maps for a radial turbine has been shown. It has been illustrated that there is a need for obtaining a good estimation of the efficiency and mass flow in the outer boundaries of the experimental data and a physical based methodology for the accomplishment of this task has been proposed.

Equations for the extrapolation of turbine maps have been developed based on physical principles and a fit procedure to the experimental data has been performed. This methodology of obtaining the extended turbine maps is useful to get a quick estimation of the unknown data and for being

implemented into 0D and 1D codes for turbochargers simulation. The obtained results have been compared against experimental information of five different radial turbines obtained from a variety of sources. It has been found a good agreement between model predictions and test data in the two main dependent variables of turbine maps, i.e. turbine isentropic efficiency and turbine mass flow ratio. The good agreement obtained between the measured and the predicted values of these two variables guarantees the quality of the extrapolations obtained with the model developed through the paper.

In addition, the extrapolation of measured data performed with the model has been also validated by an analysis and discussion of the model constants. This set of model constants is composed by geometrical data, flow angles and flow heat capacity. These constants have been obtained from a non-linear statistical fitting between model equations and experimental data and they shown a clear consistency with the expected values experimentally and/or theoretically calculated.

REFERENCES

[1] Watson, N., Janota, M.S., Turbocharging the Internal Combustion Engine, MacMillan Publishers LTD, London, ISBN 0 333 24290 4, 1982.

[2] Dale, A.P., "Radial, vaneless, turbocharger turbine performance," Ph.D. thesis, Imperial College, London, UK, 1990.

[3] Winterbone, D.E., Nikpour, B., Alexander., G.I., "Measurement of the performance of a radial inflow turbine in conditional steady and unsteady flow," *IMechE* C405/015. *Proceedings of the 4th International Conference on Turbocharging and Turbochargers*, 153 - 162, 1990.

[4] Nikpour, B., "Measurement of the performance of a radial inflow turbine," Ph.D. thesis, UMIST, Belfast, UK, 1990.

[5] Arcoumanis, C., Hakeem, I., Khezzar, L., Martinez-Botas, R.F., Baines, N., "Performance of a mixed flow turbocharger turbine under pulsating flow conditions," ASME International gas turbine and aeroengine congress and exposition, (95-GT-210), June, 1995.

[6] Szymko, S., "The development of an eddy current dynamometer for evaluation of steady and pulsating turbocharger turbine performance," Ph.D. thesis, Imperial College, London, UK, 2006.

[7] Galindo, J., Serrano, J.R., Guardiola, C. and Cervelló, C., "Surge limit definition in a specific test bench for the characterization of automotive turbochargers," Experimental Thermal and Fluid Science 30, 449–462, 2007.

[8] CIMAC (The International Council on Combustion Engines), "TURBOCHARGING EFFICIENCIES - DEFINITIONS AND GUIDELINES FOR MEASUREMENT AND CALCULATION" CIMAC Working Group 'Turbocharger Efficiency'. Number 27/2007.

[9] SAE J1826, issued 1989-04, Reaffirmed 1995-03, "Turbocharger Stand Test Code", 1995.

[10] Moustapha, H., Zelesky, M., Baines, N., Japiske, D. Axial and radial turbines, Concepts

NREC, Vermont, ISBN 0 933283 12 0, 2003.

[11] Martin, G., Higelin, P., Caillol, C., Talon, V., "Implementing turbomachinery physics into data map-based turbocharger models" SAE Technical Paper 2009-01-0310, 2009.

[12] Benson, R.S., The thermodynamics and gas dynamics of internal-combustion engines, vol. I, Oxford University Press, Oxford, ISBN 0 19 856210 1, 1982.

[13] Payri, F., Benajes, J., Reyes, M., "Modelling of supercharger turbines in internal combustion engines," *Int J Mech Sci.* 8–9:853–69, 1996.

[14] Serrano, J.R., Arnau, F.J., Dolz, V., Tiseira, A., Cervelló, C., **"**A model of turbocharger radial turbines appropriate to be used in zero- and one-dimensional gas dynamics codes for internal combustion engines modelling," Energy Conversion and Management 49, 3729–3745, 2008.

[15] Katrasnik, T. "Hybridization of powertrain and downsizing of IC engine – A way to reduce fuel consumption and pollutant emissions – Part 1"·Energy Conversion and Management 48, 1411–1423, 2007.

[16] Katrasnik, T. "Hybridization of powertrain and downsizing of IC engine – A way to reduce fuel consumption and pollutant emissions – Part 1"·Energy Conversion and Management 48, 1424–1434, 2007.

[17] Martinez-Botas, R. "Opportunities and Challenges. Turbocharger Trends and Requirements Forum", Annex in the Proceedings of the 8th International Conference on Turbochargers and Turbocharging. London, 15-18 May, 2006.

[18] Futral, S. M., Wasserbauer, C. A., "Off-design performance prediction with experimental verification for a radial-inflow turbine," NASA Technical Report TN D-2621, 1965.

[19] Heywood, J., Internal Combustion Engine Fundamentals, McGraw-Hill Science/Engineering/Math, ISBN 0 07 028637 X, 1988.

[20] Zinner, K., Supercharging of Internal Combustion Engines, Springer-Verlag, New York,

ISBN 3 540 08544 0, 1978.

[21] Muñoz, M., Payri, F., Motores de Combustión Interna Alternativos, Sección de Publicaciones de la E.T.S. de Ingenieros Industriales Fundación General – U.P.M, Madrid, ISBN 84 86043 01 9, 1989.

TABLE CAPTIONS

Table 1: k_i coefficients for the A_{eff} to A_0 ratio of the three vaneless stator truck turbines.

Table 2: Estimated values for α_1. Experimentally from stator blades metal angle for the vaned stator turbines and theoretically for the vaneless turbines

FIGURE CAPTIONS

Figure 1: Vaneless example turbines (turbine maps). A) Large size truck turbine [17]. B) Medium size truck turbine. C) Small size truck turbine.

Figure 2: Vaned example turbines (turbine maps). A) Commercial turbine map [18]. B) Passenger car turbine.

Figure 3: A_{eff} to A_0 ratio versus blade to speed ratio for large size truck turbine. Data measured at constant turbocharger speed [17].

Figure 4: A_{eff} to A_0 ratio versus blade to speed ratio for the Commercial and the Passenger car turbine. Column A) Commercial turbine [18]. Column B) Passenger car turbine. Data measured at constant turbocharger speed.

Figure 5: A_{eff} to A_0 ratio versus blade to speed ratio data measured at constant expansion ratio. A) Medium size truck turbine. B) Small size truck turbine.

Figure 6: A_{eff} to A_0 ratio versus blade to speed ratio and versus corrected blade speed for stator vaneless turbines. Data measured at constant turbocharger speed (Large [17]) and at constant expansion ratio (Medium and Small)

Figure 7: Corrected mass flow charts versus expansion ratio for the large size truck turbine. Rhombic dots: Measured points [17]. Continuous line: Equation (1) predicted mass flow for subsonic conditions and choked flow for supersonic conditions. Dotted line: Equation (1) predicted mass flow for subsonic flow conditions.

Figure 8: Corrected mass flow charts versus turbocharger speed. A) Medium size truck turbine. B) Small size truck turbine

Figure 9: Corrected mass flow charts versus expansion ratio for vaned stator turbines. Column A) Commercial turbine [18]. Column B) Passenger car turbine. Rhombic dots: Measured points. Continuous line: Equation (1) predicted mass flow for subsonic conditions and choked flow for supersonic conditions. Dotted line: Equation (1) predicted mass flow for subsonic flow conditions.

Figure 10. A) Velocity triangles for a radial turbine. B)Enthalpy versus entropy diagram for the turbine stage.

Figure 11: Isentropic efficiency fit for vaneless stator turbines; data measured at constant expansion ratio. A) Medium size truck turbine. B) Small size truck turbine. Rombic dots: Experimental data. Continuous line: Equation (23) predicted efficiency.

Figure 12: Isentropic efficiency fit for the vaneless stator large size truck turbine. Experimental data measured at constant corrected speed [17]. Rhombic dots: Experimental data. Continuous line: Equation (27) predicted efficiency.

Figure 13: Isentropic efficiency fit for vaned stator turbines; data measured at constant turbocharger speed. A) Commercial turbine [18]. B) Passenger car turbine. Rhombic dots: Experimental data. Continuous line: Equation (23) predicted efficiency.

Figure 14: K_1 coefficient, β_2 angle and A_0 for five turbines from the studied set.

Figure 15: Variation of α_1 versus blade to speed ratio. A) Example turbines with vaned stator. B) Example turbines with vaneless stator. In B) chart size reduction in triangles and circles indicates expansion ratio reduction for a given turbine.

TABLES

Table 1: k_i coefficients for the A_{eff} to A_0 ratio of the three vaneless stator truck turbines

Coefficient	*Large size*	*Medium size*	*Small size*	*k_i coefficient trend with turbine size*
k_1	0.50	0.32	0.20	↓
k_2	-0.30	-0.25	-0.13	↑
k_3	-0.20	-0.13	-0.19	≅
k_4	0.35	0.34	0.31	≅
R^2	97	97	99	

Table 2: Estimated values for α_1. Experimentally from stator blades metal angle for the vaned stator turbines and theoretically for the vaneless turbines

Turbine type	α_1
Vaned Stator Commercial turbine	63°
VGT Passenger car 0% opening	83°
VGT Passenger car 50% opening	64°
VGT Passenger car 100% opening	43°
Small truck vaneless turbine	60°
Medium truck vaneless turbine	62°

FIGURES

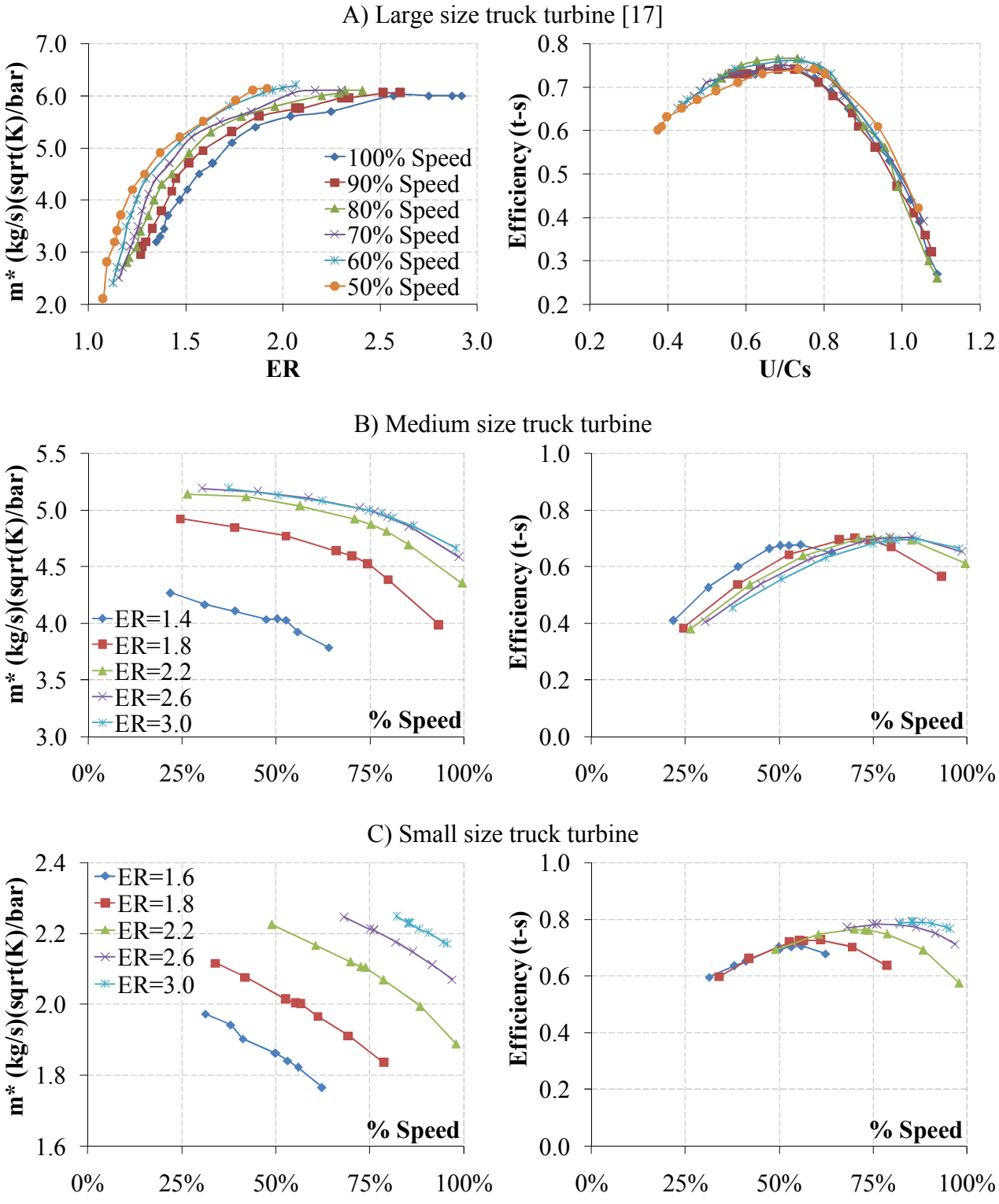

Figure 1: Vaneless example turbines (turbine maps). A) Large size truck turbine [17]. B) Medium size truck turbine. C) Small size truck turbine.

A) Commercial turbine [18]

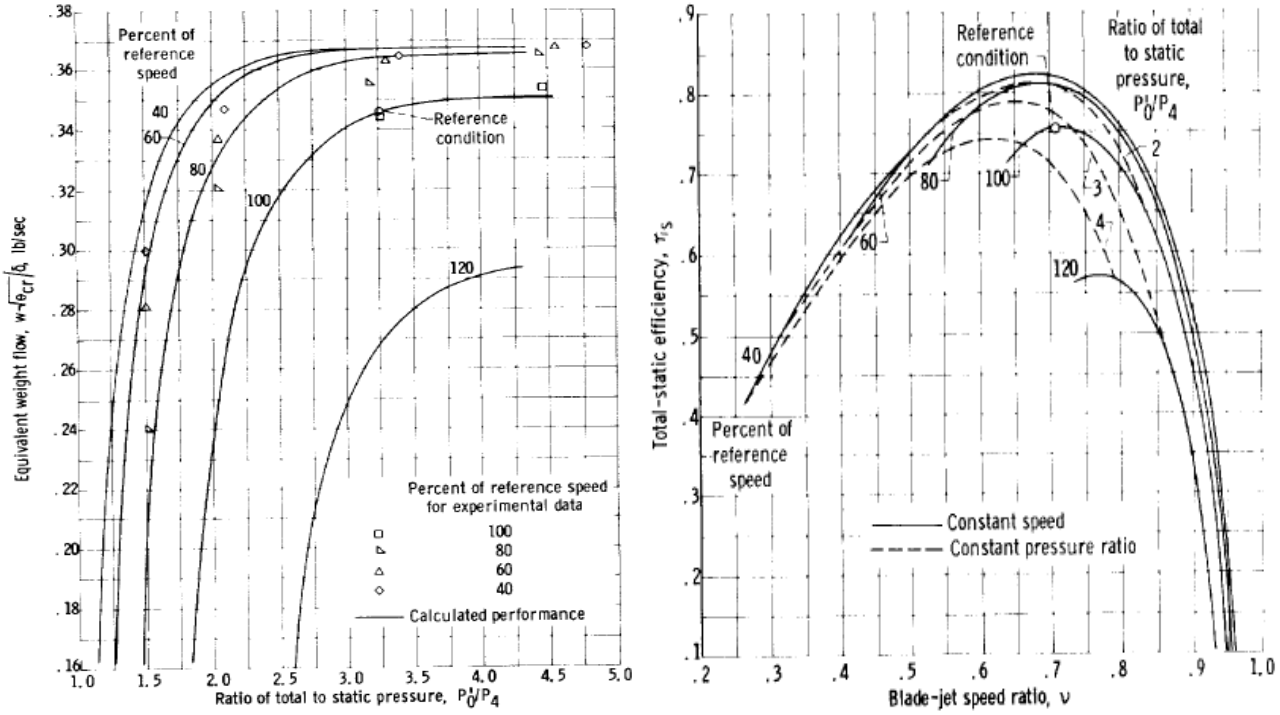

B) Passenger car turbine

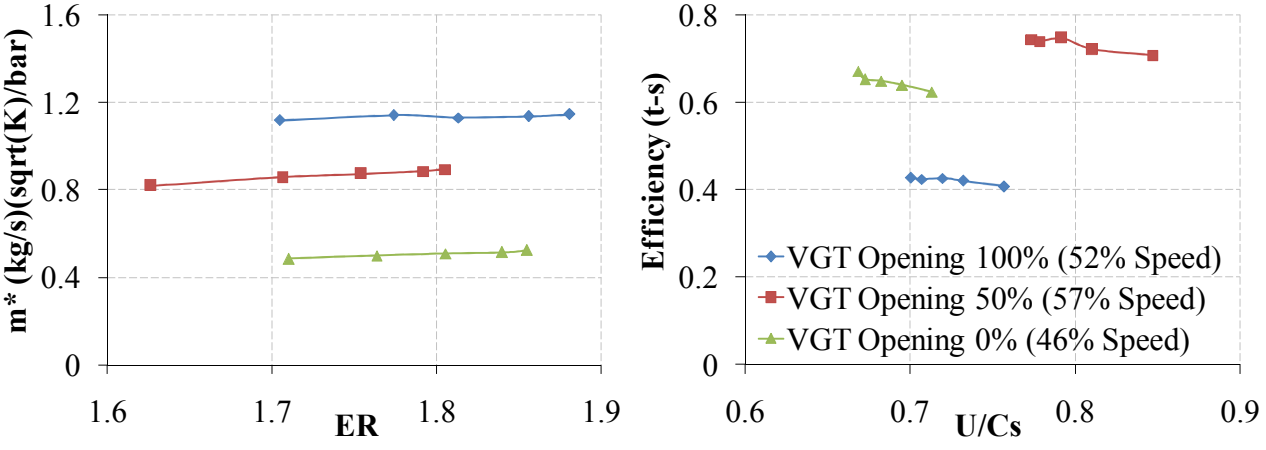

Figure 2: Vaned example turbines (turbine maps). A) Commercial turbine map [18]. B) Passenger car turbine.

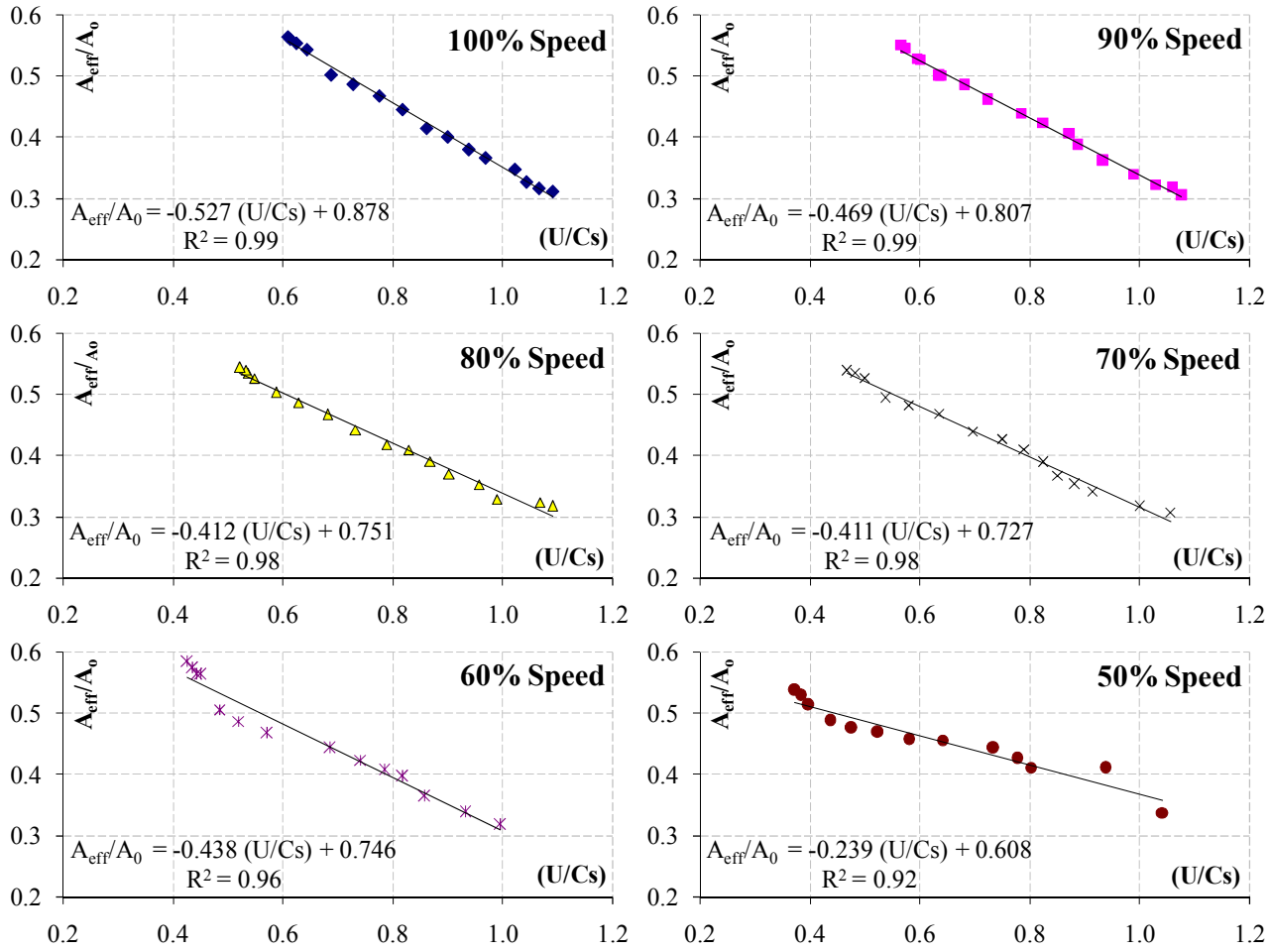

Figure 3: A_{eff} to A_0 ratio versus blade to speed ratio for large size truck turbine. Data measured at constant turbocharger speed [17].

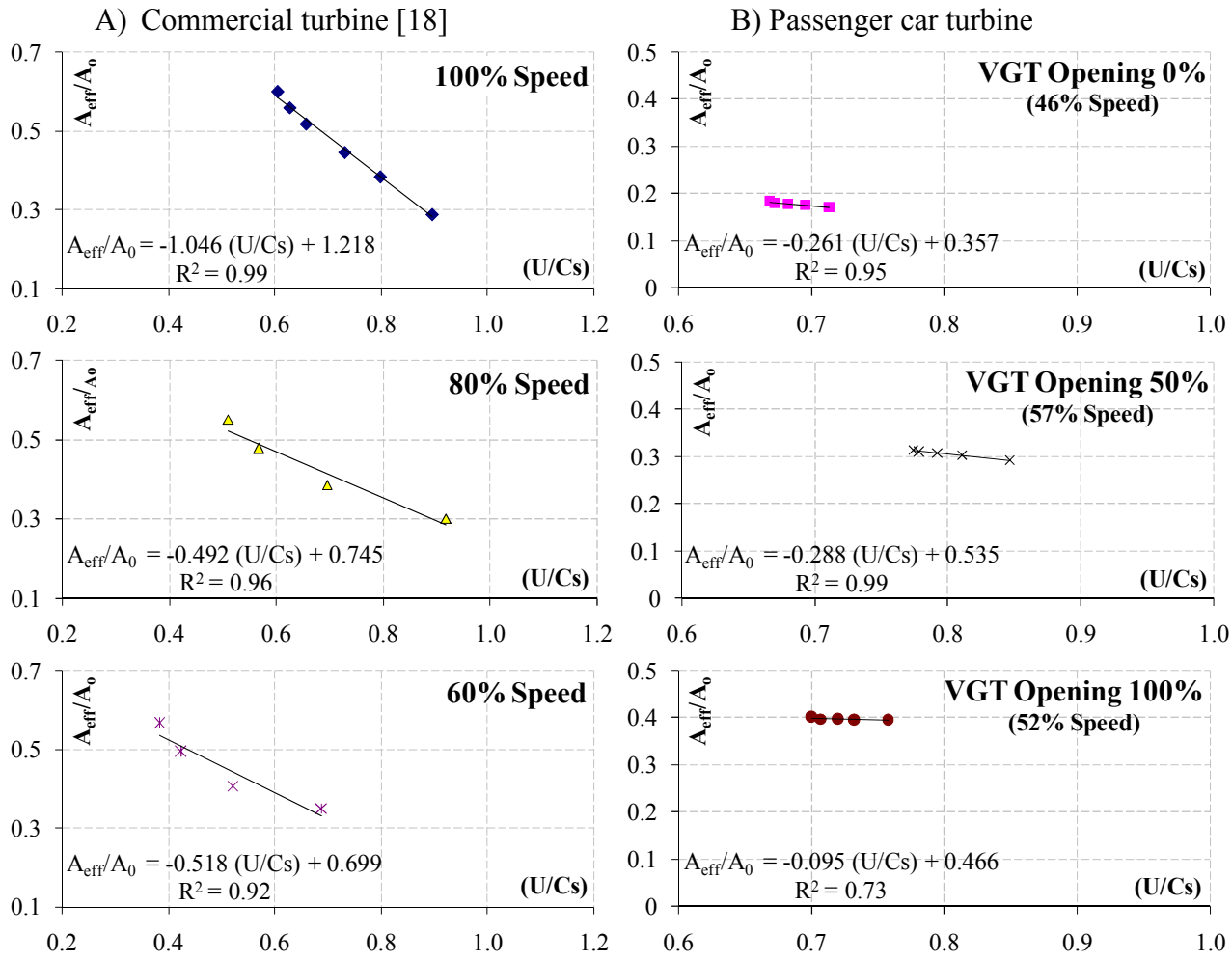

Figure 4: A_{eff} to A_0 ratio versus blade to speed ratio for the Commercial and the Passenger car turbine. Column A) Commercial turbine [18]. Column B) Passenger car turbine. Data measured at constant turbocharger speed.

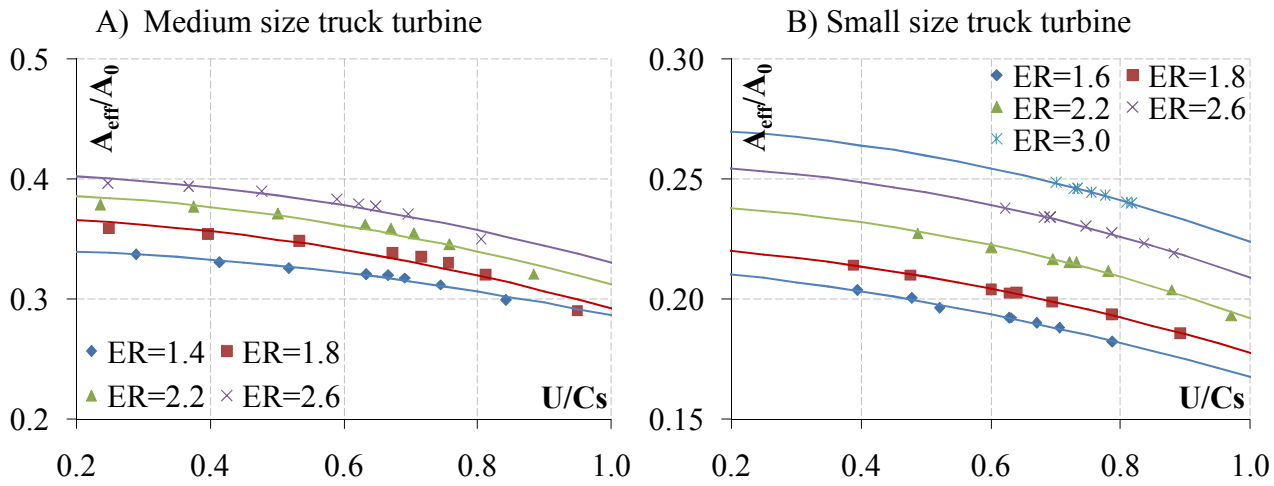

Figure 5: A_{eff} to A_0 ratio versus blade to speed ratio data measured at constant expansion ratio. A) Medium size truck turbine. B) Small size truck turbine

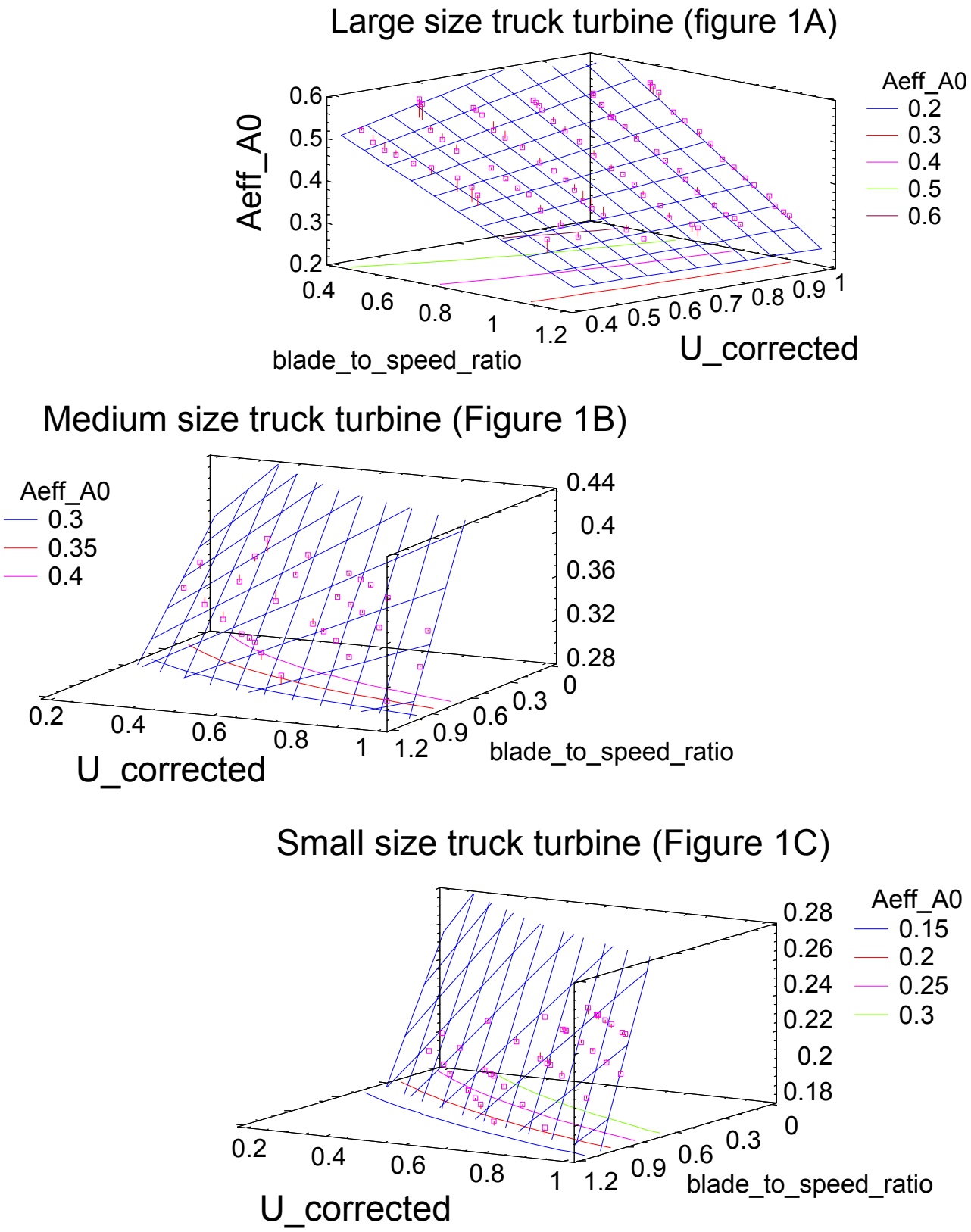

Figure 6: A_{eff} to A_0 ratio versus blade to speed ratio and versus corrected blade speed for stator vaneless turbines. Data measured at constant turbocharger speed (Large [17]) and at constant expansion ratio (Medium and Small)

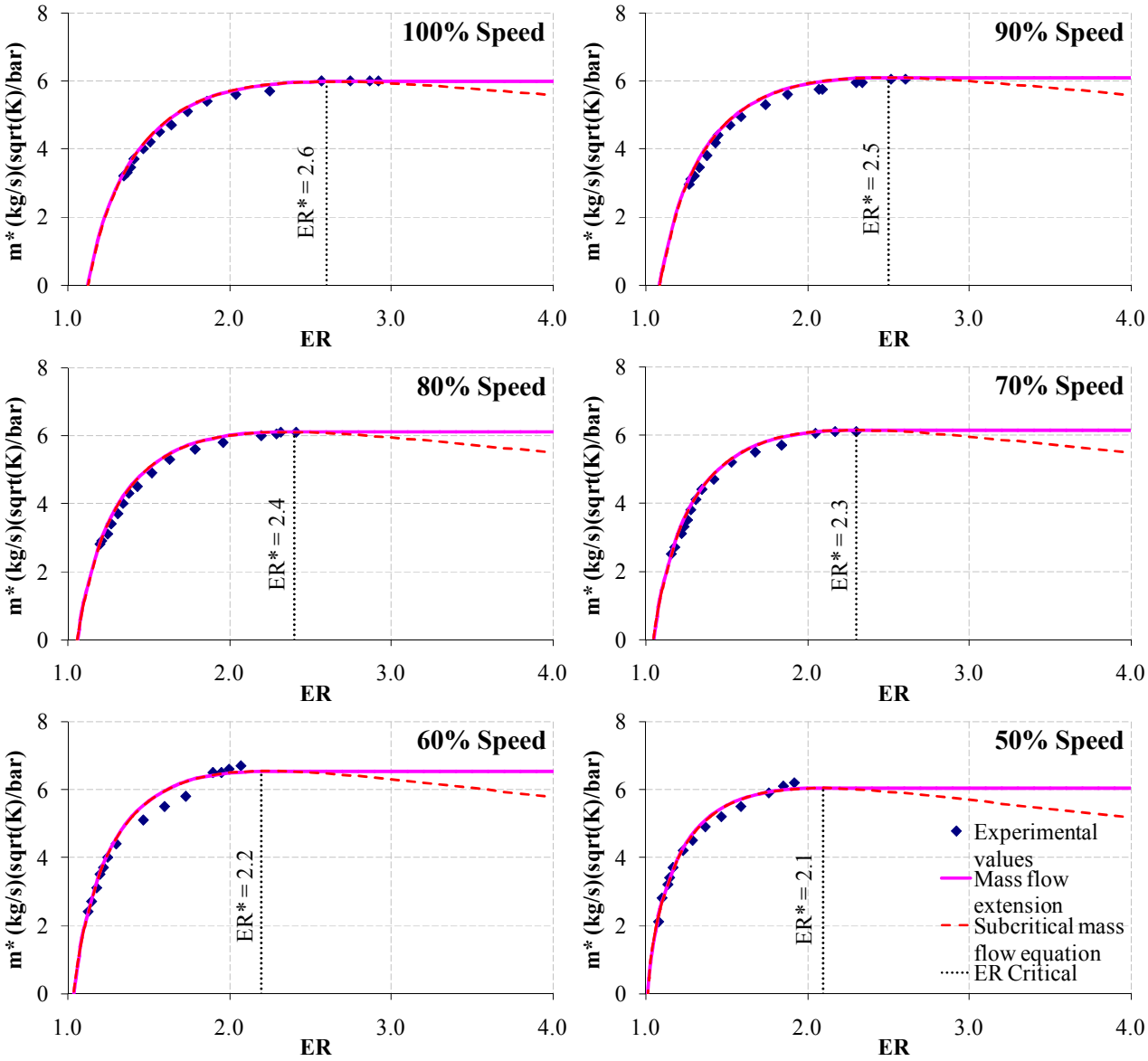

Figure 7: Corrected mass flow charts versus expansion ratio for the large size truck turbine. Rhombic dots: Measured points [17]. Continuous line: Equation (1) predicted mass flow for subsonic conditions and choked flow for supersonic conditions. Dotted line: Equation (1) predicted mass flow for subsonic flow conditions.

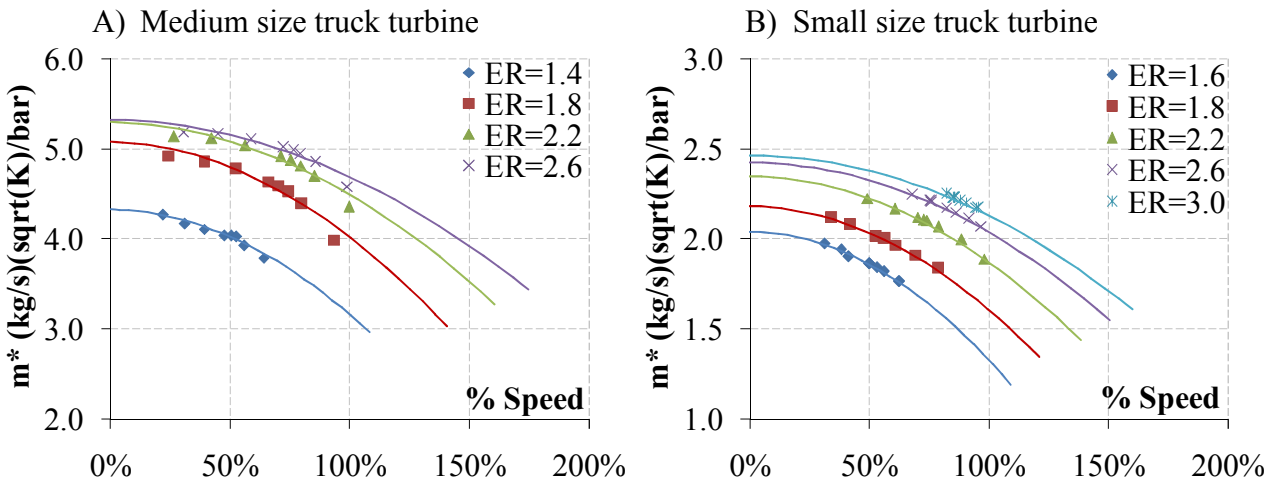

Figure 8: Corrected mass flow charts versus turbocharger speed. A) Medium size truck turbine. B) Small size truck turbine

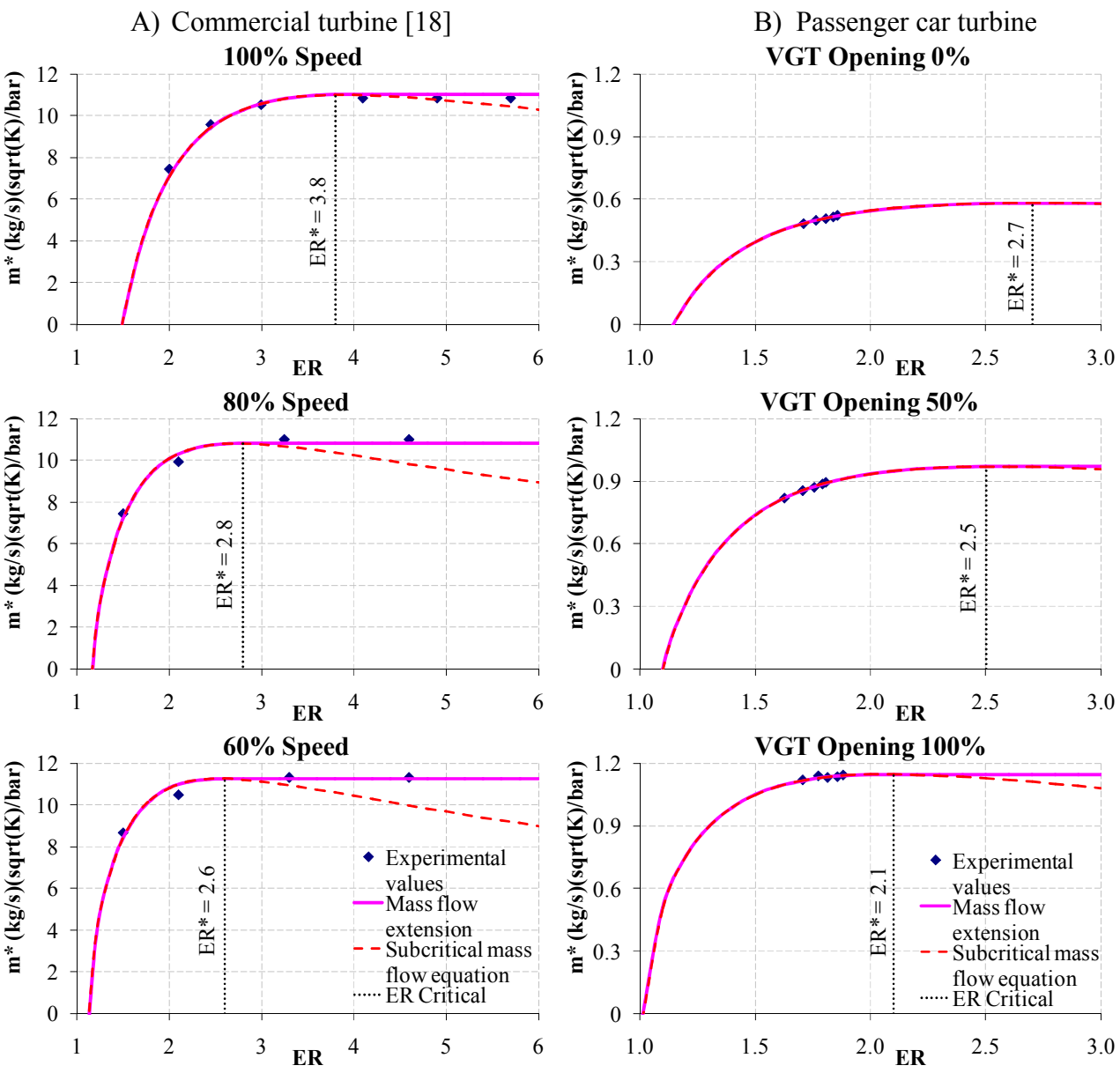

Figure 9: Corrected mass flow charts versus expansion ratio for vaned stator turbines. Column A) Commercial turbine [18]. Column B) Passenger car turbine. Rhombus: Measured points. Continuous line: Equation (1) predicted mass flow for subsonic conditions and choked flow for supersonic conditions. Dotted line: Equation (1) predicted mass flow for subsonic flow conditions.

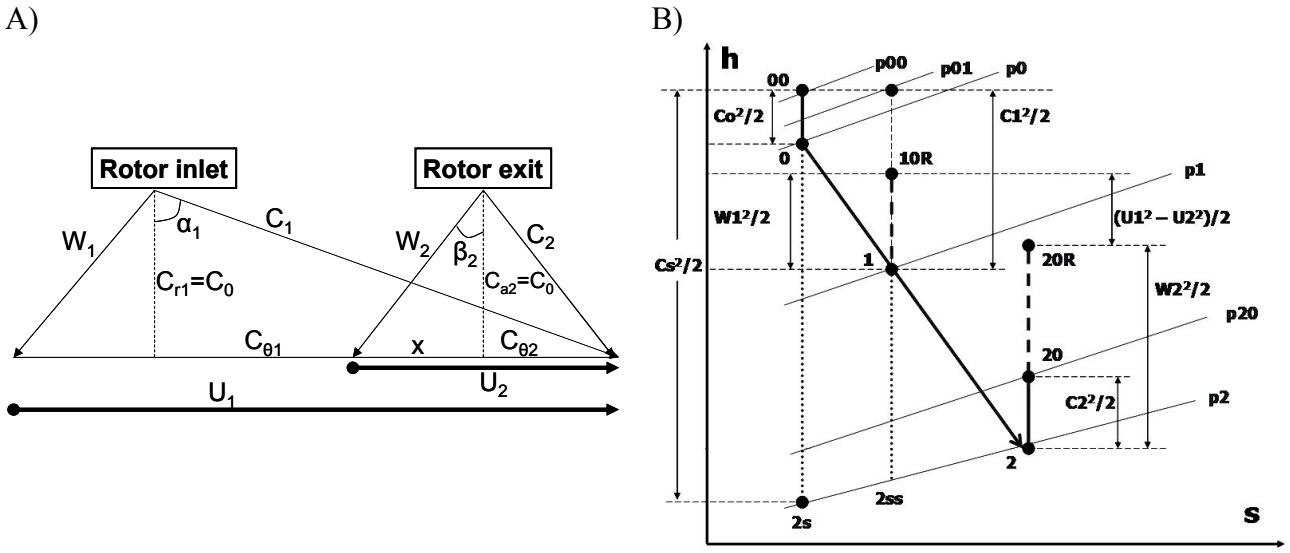

Figure 10. A) Velocity triangles for a radial turbine. B) Enthalpy versus entropy diagram for the turbine stage.

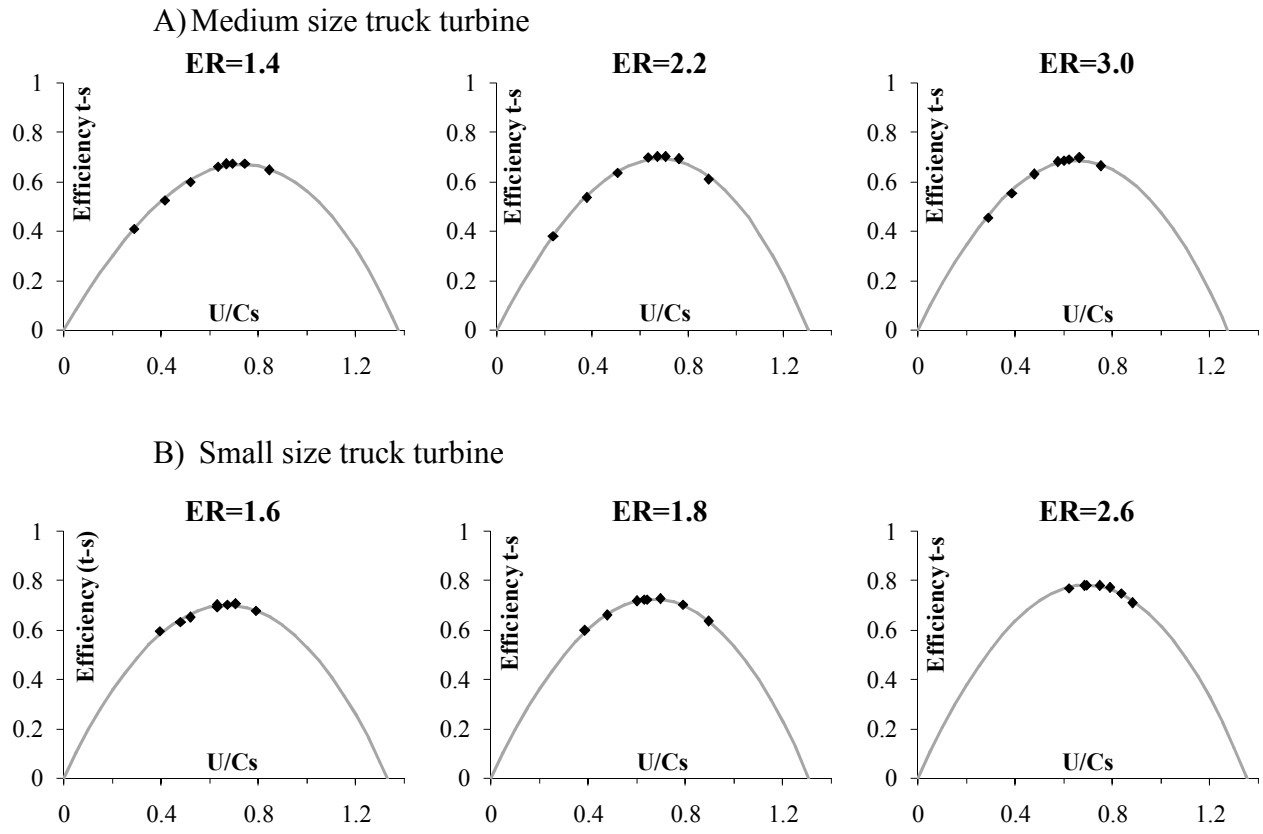

Figure 11: Isentropic efficiency fit for vaneless stator turbines; data measured at constant expansion ratio. A) Medium size truck turbine. B) Small size truck turbine. Rhombus: Experimental data. Continuous line: Equation (23) predicted efficiency.

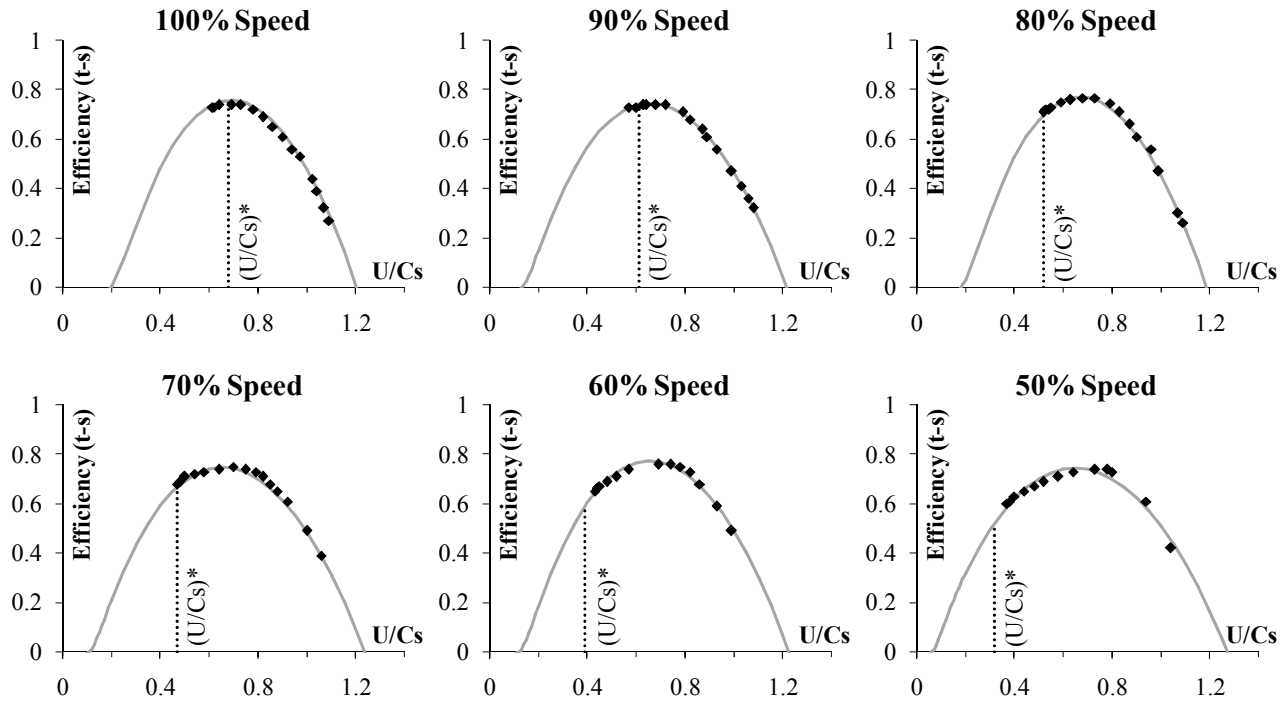

Figure 12: Isentropic efficiency fit for the vaneless stator large size truck turbine. Experimental data measured at constant corrected speed [17]. Rhombus: Experimental data. Continuous line: Equation (27) predicted efficiency.

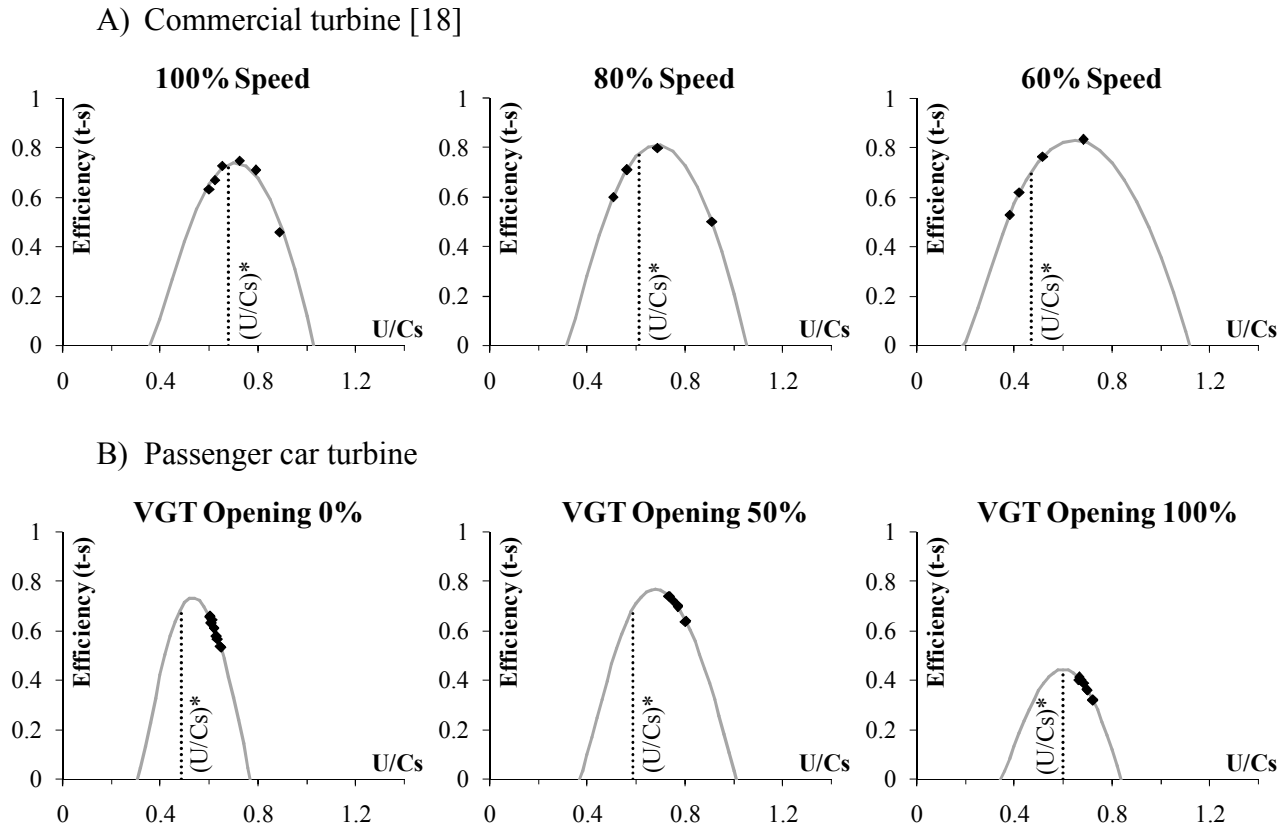

Figure 13: Isentropic efficiency fit for vaned stator turbines; data measured at constant turbocharger speed. A) Commercial turbine [18]. B) Passenger car turbine. Rhombus: Experimental data. Continuous line: Equation (23) predicted efficiency.

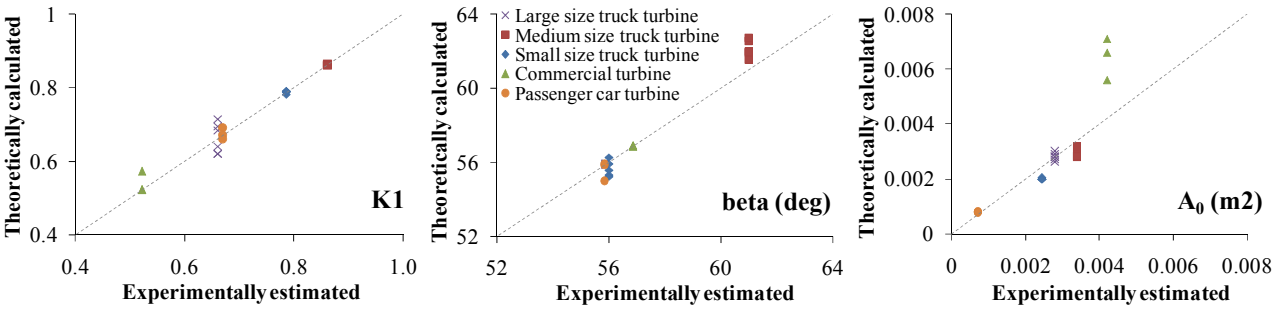

Figure 14: K1 coefficient, β_2 angle and A_0 for five turbines from the studied set.

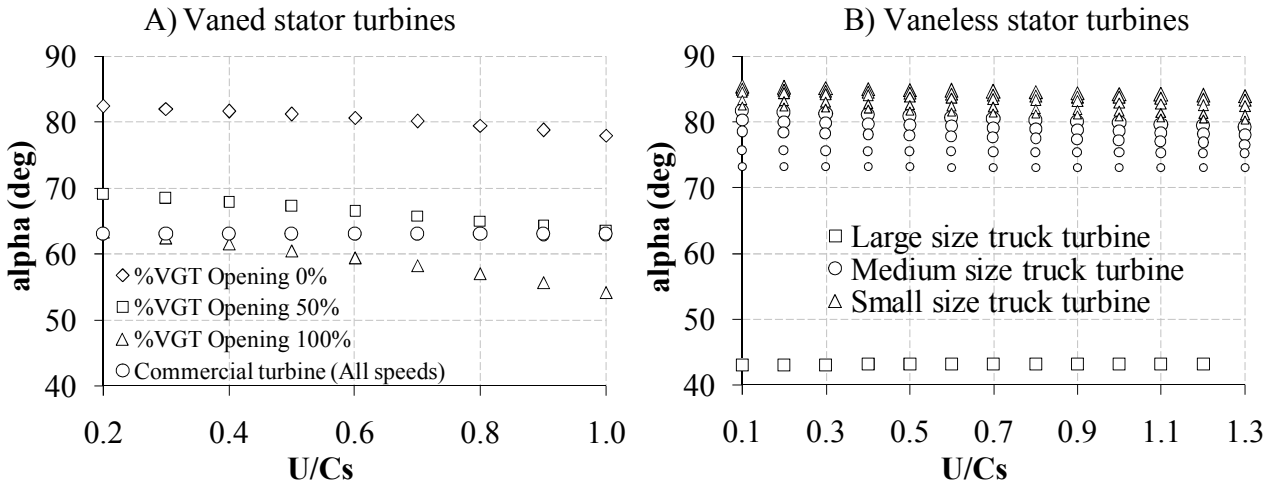

Figure 15: Variation of α_1 versus blade to speed ratio. A) Example turbines with vaned stator. B) Example turbines with vaneless stator. In B) chart size reduction in triangles and circles indicates expansion ratio reduction for a given turbine.

ANEXO IV: NUMERICAL STUDY OF THE IMPLEMENTATION OF AN ACTIVE CONTROL TURBOCHARGER ON AUTOMOTIVE DIESEL ENGINES

NUMERICAL STUDY OF THE IMPLEMENTATION OF AN ACTIVE CONTROL TURBOCHARGER ON AUTOMOTIVE DIESEL ENGINES

Galindo, J.[1]; Dolz, V.; Tiseira, A.; Gozalbo, R.

Universidad Politécnica de Valencia
CMT – Motores Térmicos
Camino de Vera, s/n. 46022. Valencia, SPAIN.

(*Received date ; revised date*)

ABSTRACT – Active control turbocharger (ACT) has been proposed as a way to improve turbocharger performance under highly pulsating exhaust flows. This technique implies that the variable geometry mechanism in the turbine is used to optimize its position as a function of the instantaneous mass flow during the engine cycle. Tests presented in the literature showed promising results in a pulsating gas-stand. In this work, a modelling study has been conducted at different engine conditions aimed to quantify the gain in on-engine conditions and to develop a strategy to integrate the ACT system within the engine. Different ways of changing the displacement of the variable mechanism have been analyzed by means of a one-dimensional gas-dynamic model. The simulations have been carried out at constant engine operating points defined by fixed air-to-fuel ratio for different mechanism displacement functions around an average position that guaranties the desired amount of intake air. The benefits in overall engine efficiency are lower to those predicted in the literature. It can be concluded that it is not possible to use the ACT system to optimize the turbine operating point and at the same time to control the engine operating point.

KEY WORDS: Turbocharger, ACT, Air management, VGT, IC engine

1. INTRODUCTION

Turbochargers are a successful mean of increasing the power output of a reciprocating engine of both the Gasoline and Diesel variety and are used extensively nowadays, especially in small sized diesel engines. However, a fundamental issue that has so far not been addressed satisfactorily is the less than ideal combination of a reciprocating engine providing energy to drive a rotodynamic machine such as a turbocharger turbine.

Yet even with the use of current Variable Geometric Turbines (VGTs), this mismatch is not eliminated, since a VGT responds to operating point changes only (*Filipi Z., et al., 2001)*. A VGT assumes a non-changing, optimal condition at steady-state operation for a nozzle setting. However, regardless of the engine operating at steady-state or transient mode, the inlet conditions to the turbocharger still include a highly pulsating flow field with widely varying pressure and mass flow rate levels at all times. The turbine does not receive a constant pressure and constant mass flow, which would be what a rotodynamic device would like to see. Instead, pressure pulses arrive at the turbine inlet, affecting its overall performance.

Another strategy to improve the coupling between the IC engine and the turbocharger is the use of a turbine waste-gate. This mechanism allows bypassing exhaust gas flow around the turbine, allowing control on the gas flow through the turbine and on the engine backpressure (*Ghazikhani M., et al., 2008).* Although the original waste-gate mechanism does not eliminate the pulsating flow mismatch, as it only responds to operating point changes, recent developments have led some authors (*Möller et al., 2005 and Roth et al., 2010)* to develop the Divided Exhaust Period method, in which the cylinder exhaust period is divided in two phases. Initially the cylinder discharges directly to a fixed geometry turbine in a first phase, while in a second phase the turbine is bypassed to reduce the IC engine pumping losses. In order to achieve this control action, a modified camshaft developed by *Smith F., Simpson R., (2005)* is used. Unfortunately, matching exhaust pressure and mass flow pulses is not easy, as the actuators and the control system used must have a very rapid and dynamic response to changes in very short time periods (*Ferreaua H. J. et al., 2007)*.

[1]*Corresponding author*. e-mail: galindo@mot.upv.es

As proposed in this study, an Active Control Turbocharger (ACT) could be a smart solution to address this mismatch problem. The ACT is a special type of VGT, where the inlet nozzle is able to alter the inlet area at the throat of the turbine inlet casing in phase and at the same frequency as that of the incoming exhaust gas pulses. Therefore, by continually altering the effective throat area of the turbine and adapting it the instantaneous pressure, extra energy can be recovered as the turbine will always be working at is optimum point. These inlet nozzle periodic oscillations will also aid in the matching of the reciprocating engine with the rotodynamic device. The control system selected for this type of turbocharger can be very complex as it has to have a very rapid and precise response. Coordination and adjustment problems may appear (*García-Nieto S., et al., 2008)* as the ACT system will have to vary accordingly with the frequency and amplitude of the pulses at the turbine inlet.

According to experiments which have already been carried out using this new turbocharger concept (*Pesiridis A. and Martinez-Botas R. F., 2007*), ACT exhibits a good potential as the turbine achieved an actual power gain ranging between 3% and 7% depending on the nozzle area phasing. These experiments were carried out using a pulse generator in order to simulate the exhaust pulses generated in a real engine. This basically proves that the ACT concept is feasible, as it is able to achieve a significant improvement on its performance, although tests with real engines should be carried out in order to corroborate this improvement.

Reciprocating 4-stroke engine performance is very dependent on backpressure and pumping losses. Backpressure pulses are also very helpful in extracting the exhaust gases from the combustion chamber and this is why good exhaust pipe designs are required. Unfortunately, as just explained, the use of an ACT will cancel this pulses, as the inlet effective area will be constantly varying and adapting to the pressure pulse, consequently cancelling the pulses. This continuous opening and closing of the turbine's nozzle will probably also affect the exhaust backpressure and could therefore increase the pumping losses. The effect of the ACT on the overall engine performance is unknown and this is what will be tried to be unveiled in this research.

2. THE ACT CONCEPT

ACT stands for Active Control Turbine and it is an evolution of the actual VGTs. Its main difference consist in the fact that VGTs only respond to changes in operating points, while this new turbine concept is not just able to do this, but is also capable of responding to pressure pulses when operating at a constant engine regime.

There are two fundamental problems with actual turbines as seen in *Watson N. and Janota M.S., (1982)* and *Karamanis N, et al. (2001)*. Firstly, there is a mismatch between the desired steady-state flow which the turbine is designed for and the pulsating exhaust flow that the engine works with. Secondly, as this pressure pulses are not taken into account by the turbine, this energy is wasted, as the turbine assumes the flow is constant.

Both of these problems can be solved by using an active controlled turbine, as this turbine has the ability to vary its inlet throat area, not just when the operating point of the engine varies, but with the pressure pulses in the exhaust. By continually altering the effective throat area, extra energy can be recovered. Fortunately, this also has very positive effect on the matching between the engine and the turbine, as by actively controlling the throat area, pulses entering the turbine are cancelled, making the turbine work with quasi-steady flow.

The benefits of using this system can be quantified and many experiments have been carried out previously with very positive results. The performance of the turbine can be increased as proved by *Pesiridis A. and Martinez-Botas R. F. (2007)*. Unfortunately, this gain in potential comes at a cost, which is due to the complicated mechanism required for the rapid control of inlet nozzle. In a 4 cylinder engine, like the one used in this research, there will be 4 pressure pulses per cycle, so at an engine operating regime of 4000rpm, this implies that the nozzle will have to open and close 133 times every second. i.e. 130Hz. Apart from this, if this active control wants to be directly linked to the exhaust pressure, a rapid acquisition sensor of the same or higher frequency will be required, as well of a very rapid control system. Previous experiments have been carried out using an electro-magnetic shaker supplied by a powerful amplifier in order to actuate the nozzle. This shaker was not linked to a pressure acquisition system, but to a sine wave generator system closely matched the pressure pulses.

3. OBJECTIVES

The main objective of this study is to optimize the efficiency and performance of a turbine mounted on a commercial Diesel engine, making use of turbine active control techniques. At the same time, the effects that these techniques will cause on engine backpressure, pressure losses and overall performance of the engine will also be investigated.

In order to achieve these objectives, three main tasks were carried out:

1) Calibration using measured data for 5 operating points of the Diesel engine 1D model with a conventional turbocharging system.
2) Generation of a specific sub-model for the turbine which allowed changing the VGT position as a function of time in concordance with the engine exhaust pulsations.

3) Optimisation of the VGT position evolution to improve turbine efficiency and engine backpressure and pumping losses.

4. 1D GASDYNAMIC MODEL

The 1D gas-dynamic code used in this paper to model the IC engine and the turbocharger is a wave action model which has been developed at CMT-Motores Térmicos in Universidad Politécnica de Valencia. This model calculates the IC engine and the turbocharger behaviour by means of unsteady equations of mass, momentum and energy conservation and it is solved by finite differences schemes (*Galindo et al, 2009a*). The model is known now as OpenWAM as it has been recently published as open source in *www.openwam.com*. This tool allows modelling with high precision the entire engine system (cylinders, valves, tubes, etc.) as well as the turbocharging system, as demonstrated by *Serrano et al, (2008)* (VGT turbine) and *Galindo et al. (2009b)* (compressor). The OpenWAM model has been fitted using experimental data from an IC engine and turbocharger installed in a research test ring.

Two outstanding OpenWAM model aspects in steady flow are emphasized: The heat transfer model and the turbocharger model. This gas-dynamic model calculates the heat transfer in pipes and cylinders. The heat transfer model is able to calculate the heat transfer in steady and transient operation. The heat transfer model is evolved from *Galindo et al, 2006*.

In addition, OpenWAM is able to reproduce the turbocharger performance based on the measured characteristics of the turbocharger. Nevertheless, it is capable of extrapolating operating conditions that differ from those included in the turbine maps, since the engines usually work within these zones as presented by *Serrano et al, 2008.*

The turbocharger is considered as a model divided in two elements: turbine and compressor. Each component of the turbocharger is represented by means of ducts (1-D elements), volumes (0-D elements) and boundary conditions. On the hand, the modelling of the turbine must take into account the fluid-dynamic behaviour of the gas along the exhaust system: interaction between cylinders, and flow evolution downstream of the turbine. On the other hand, the modelling of the turbine must take into account the energy conversion and the non isentropic processes generated in the expansion process. This energy will be available to the compressor, and it must be done a balance between the energy produced by the turbine and the energy consumed by the compressor.

The turbine model is based on the representation of a turbine by two ideal nozzles discharging to an intermediate volume. The first nozzle represents the stator of the turbine and the second nozzle stands for the turbine rotor. The intermediate chamber is able to account for the mass accumulation in transient conditions like pulsating flow, which takes place in reciprocating engines. This model is able to calculate the pressure drop produced at the stator and at the rotor, taking into account the turbine efficiency and may be formally expressed as:

$$\frac{p_1}{p_2} = \left(1 + \frac{T_{00}}{T_0}(R-1)\eta_{Ts}\left[1 - \left(\frac{p_2}{p_{00}} \right)^{\frac{\gamma-1}{\gamma}} \right] \right)^{k/k-1} \quad (1)$$

Once these pressure drops are know, it is possible to calculate the effective areas of the equivalent nozzles representing the turbine stator and rotor. The stator effective area is defined as:

$$S_{eff\_st} = \dot{m}_T \cdot \frac{\sqrt{\Re \gamma T_{00}}}{p_{00}} \cdot \frac{1}{\gamma} \cdot \left(\frac{p_{00}}{p_1} \right)^{1/\gamma} \cdot \left(\sqrt{\frac{2}{\gamma-1}\left[1 - \left(\frac{p_1}{p_{00}} \right)^{(\gamma-1)/\gamma} \right]} \right)^{-1} \quad (2)$$

and the rotor effective area:

$$S_{eff\_st} = \dot{m}_T \cdot \frac{\sqrt{\Re \gamma T_{00}}}{p_{10}} \cdot \frac{1}{\gamma} \cdot \left(\frac{p_{1R}}{p_2} \right)^{1/\gamma} \cdot \left(\sqrt{\frac{2}{\gamma-1}\left[1 - \left(\frac{p_2}{p_{10R}} \right)^{(\gamma-1)/\gamma} \right]} \right)^{-1} \quad (3)$$

The compressor boundary condition is modelled using the energy obtained by the turbine and the compressor map information.

5. MODEL CALIBRATION

When working with computer models, the model calibration is the most important aspect. Due to the complexity of the model and simplifications used, computer models are not able to output values with no errors. Results might be very close to reality, but there always have an induced error due to simplifications. In order to counteract this effect, models are calibrated using real data obtained from experimental evaluations.

OPENWAM uses a 1D model to reproduce the flow interactions in an engine, so even though the code is very robust and reliable, correction factors are required to match the model generated by the software with the real engine. These corrections are required especially for the heat transfer produced by swirl in the cylinder, as well as for the efficiency of the compressor and turbine, as the efficiencies supplied by the manufacturer do not take into account pulsating flow or exhaust gas properties. Results for a 4 cylinder passenger car engine were readily available before the start of this investigation, as previous experiments had already been carried out at “CMT – Motores Térmicos” with this particular engine, so this engine model was used. The engine characteristics can be observed in Table 1.

The engine operating points that were calibrated can be seen in

Table 2. All the modelled average results, including admission pressure and temperatures, air-fuel ratio, power, torque, air mass flow, cylinder pressure and

temperature, EGR, exhaust pressures and temperatures, were kept under ± 5% difference from the measured values. Special care was taken with the results affecting the turbine, such as the entry and exit pressures and temperatures.

Table 1. Engine characteristics

Engine type	Direct Injection Turbocharged Diesel engine
Displacement	1998 cm^3
Compression ratio	19:1
Nº of Cylinders	4
Maximum torque	320 Nm @ 1750 rpm
Maximum power	100 kW @ 4000 rpm

Table 2. Engine operating points.

Point	Speed (rpm)	BMEP (bar)	Comment
#1	4000	13.40	Full load – Max power
#2	2250	18.95	Full load – Max torque
#3	1500	6.00	Low load
#4	2000	10.00	Medium load
#5	2500	14.00	High load

Instantaneous modelled results were in phase and matched the measured results. Figure 1 shows an example for test points #1 and #4. The figure only shows the pressures at the entry (P3) and exit (P4) of the turbine for clarity. The maximum pressure difference is around ± 0.2 bar for all the studied cases.

6. ACTIVE CONTROL TESTS

After the analysis of the exhaust pressure pulses, a series of different tests were carried out in order to analyse the behaviour of the active control turbine when matched with an internal combustion engine.

6.1. Optimum control

An initial test was carried out fixing the turbine's efficiency to its highest value in order to obtain the maximum potential benefits of the engine. These results will be set as target values for the active control tests, as the aim is to make the turbine operate as close as possible to its maximum efficiency. For the test turbine, the maximum efficiency was 0.7.

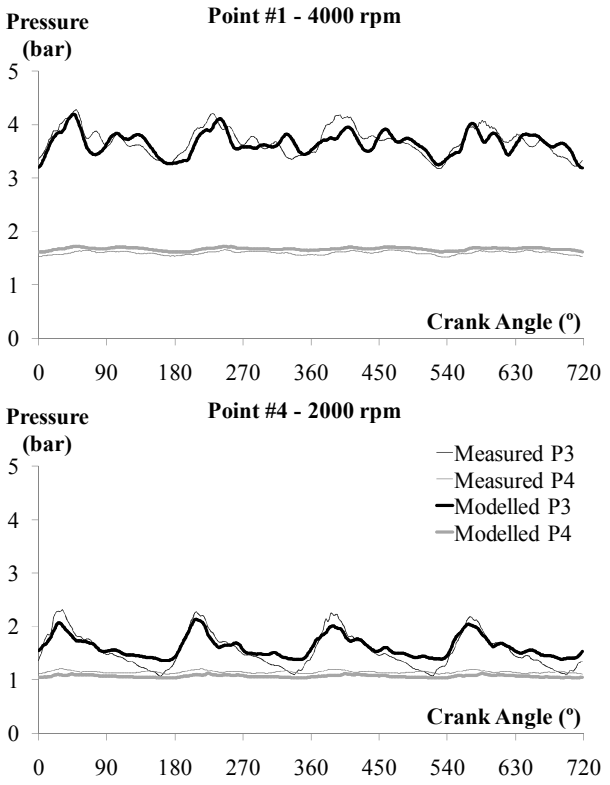

Figure 1. Instantaneous modelled and measured results for test points #1 and #4

Increasing the turbine's efficiency results in an increase in the air mass flow of the engine, as more energy is transferred to the compressor and more work is done. This implies that the engine is at another working condition, so to keep the results comparable for all the tests points, the engine air-fuel ratio was kept as constant as possible. The extra fuel pumped to maintain the A/F ratio, provided an increase in torque and power, while there was a slight reduction in specific fuel consumption.

Table 3 and

Table 4 show the results of the optimum control experiments for the test points #1 and #4. As it can be seen, increasing the air mass flow but keeping the A/F ratio constant, a maximum torque increase of 3.33% is obtained with a reduction in specific fuel consumption of 0.71% at 2000rpm. At 4000rpm similar results are observed: a reduction of specific fuel consumption of 0.68% with an increase in maximum torque of 2.35%.

Table 3. Optimum control results for point #1

4000RPM	REF	TEST	DIFF
Torque	212.9	218.1	2.35%
AF ratio	21.4	21.5	0.27%
Mair	473.3	483.0	2.00%
SFC	0.249	0.247	-0.68%

Table 4. Optimum control results for point #4

2000RPM	REF	TEST	DIFF
Torque	161.2	166.7	3.33%
AF ratio	16.8	16.7	-0.5%
Mair	136.7	143.5	4.71%
SFC	0.242	0.239	-0.71%

Thus, the target values to be achieved by using ACT are a torque increase of 2.35% and 3.33% for point #1 and #4, respectively.

6.2. Sine wave control

Once the maximum available gain in torque and performance of the engine was obtained from the previous test, a series of tests were carried out in order to control the opening and closing of the variable geometry turbine nozzle.

A sinusoidal wave was initially implemented in the code to control the VGT opening and was synchronized in phase with the exhaust pressure pulses to obtain the maximum benefits. The VGT opening was controlled by the actuator shaft displacement and was opened at peak pressure pulses and closed at low pressure valleys to compensate for the non-steady flow.

To allow for comparison between the effects of the different active control tests and the base engine performance, the average VGT opening and the air-fuel ratio was kept constant. Keeping the average VGT opening constant implies that the operating point of the turbine and the engine will not change. If the efficiency of the turbine changed, this will translate into a change of engine air mass flow, which was compensated by keeping the air-fuel ratio constant, in order to obtain comparable results.

The sinusoidal wave control was implemented for the two studied cases: point #1 and point #4, with different shaft displacement amplitudes (1mm and 2mm) as can be seen in Figure 2. The reference value is the original VGT shaft displacement used at each operating engine operating point.

Table 5 shows the results for the different tests. As it can be observed, the results are not as expected as the turbine average efficiency decreases for most of the test cases, especially for the 2mm – 2000 rpm case, were the efficiency drops by 2.25%. The rest of the engine parameters show little or no change at all.

In order to better understand why the turbine's average efficiency has decreased, a plot against crank angle is shown in Figure 3. By comparing Figure 3 with Figure 2, it can be clearly seen that the efficiency drops below the reference value when the VGT is opened (increase VGT shaft displacement), while it increases when the VGT is closed.

Taking the cycle average efficiency, the results are very close to the reference efficiency as shown in Table 5. In both cases (1mm and 2mm displacement), when the VGT is closed, similar maximum efficiency values are attained, but when the VGT is opened, the drop in efficiency is bigger for the 2mm case. Thus, this explains why they average efficiency is always lower for the 2mm shaft displacement.

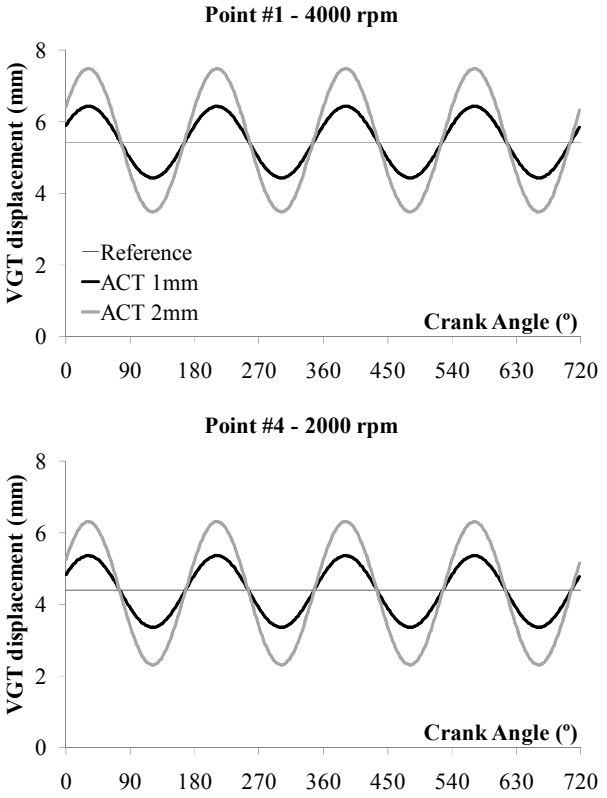

Figure 2. Sine wave displacement model

Table 5. Sine wave mean efficiency results

	#1 - 4000 rpm		**#4 - 2000 rpm**	
	1mm	2mm	1mm	2mm
Reference	0.651	0.651	0.666	0.666
ACT	0.652	0.648	0.661	0.651
Difference	0.15%	-0.46%	-0. 75%	-2.25%

The reason for this variation in efficiency when varying the VGT shaft displacement can be further analyzed and explained using the efficiency-displacement plots shown in Figure 4.

This plot shows the relationship between the efficiency and the VGT shaft displacement of the turbine used in this investigation with respect to the change in blade to jet speed ratio. The efficiency values of this turbine were only supplied by the manufacturer for shaft displacements of 2, 4, 6 and 8 mm and for different blade to jet speed ratios, so as to complete the efficiency-displacement plot, the data was interpolated between the shaft displacements of 2 to 8 mm.

When the results are represented on the efficiency-displacement plot, the effect of the ACT can be clearly observed. When the VGT is closed, the turbine operates very close to the maximum efficiency area, but all this gain is lost when the VGT is opened, as the turbine moves into very low efficiency regions.

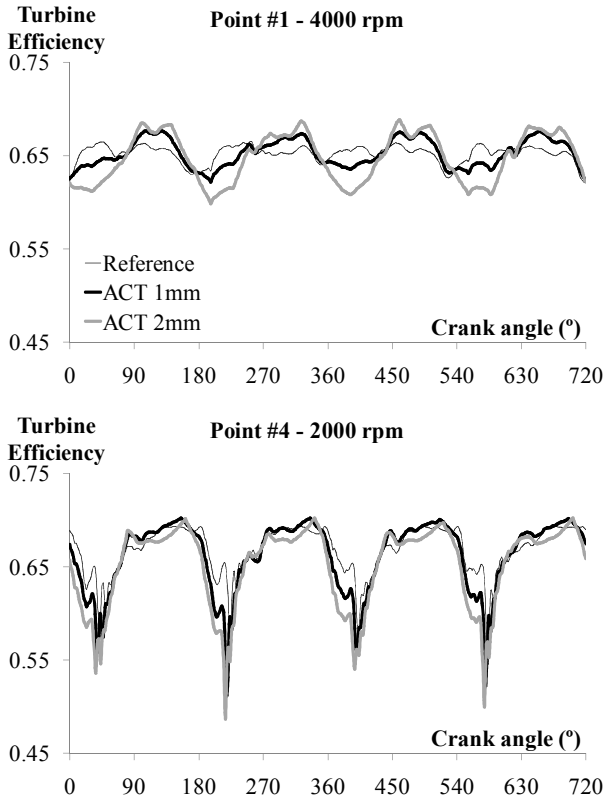

Figure 3. Sine wave instantaneous efficiency

6.3. Half - sine wave control

According to the previous results, it seems that the turbine VGT opening is adjusted to work with the peak pressure pulses, as there was only a gain in efficiency when closed at the pressure valleys. All the potential gain was lost when the turbine was opened at peak pulses, so another control strategy was developed.

Instead of opening and closing, it was decided just to close at the pressure valleys and leave the original opening position on the peak pressure pulses. This control strategy is shown in Figure 5.

The effect of this new half-sine curve is shown in the following Figure 6. The gain in average turbine efficiency with respect to the reference value was of 1.33% for the 2mm opening at point #1.

This half-sine wave control was just tested for one point and one opening, as unfortunately by just closing the VGT implied that the average opening is much lower than the original, so the turbocharger was working at a different operating point. This lead to a change in engine operating conditions, and although the A/F ratio was kept constant, this test point can not be compared with the base engine performance as the operating conditions are different.

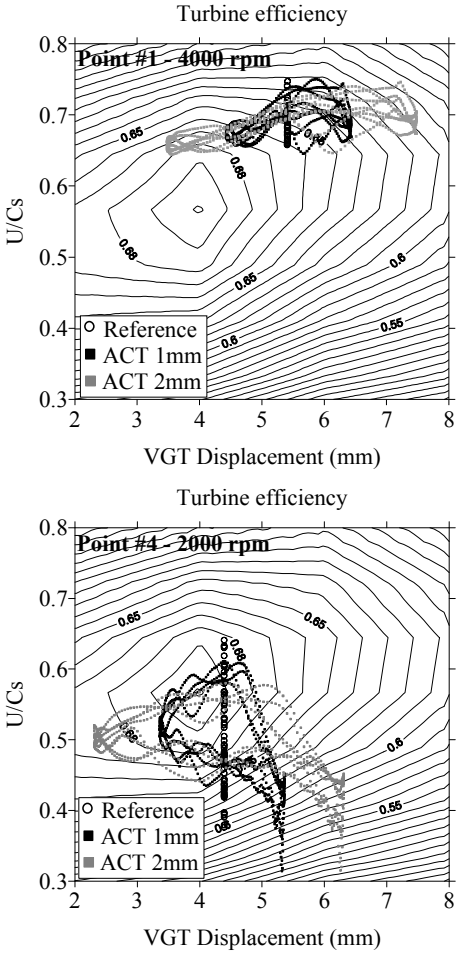

Figure 4. Sine wave efficiency-displacement plot

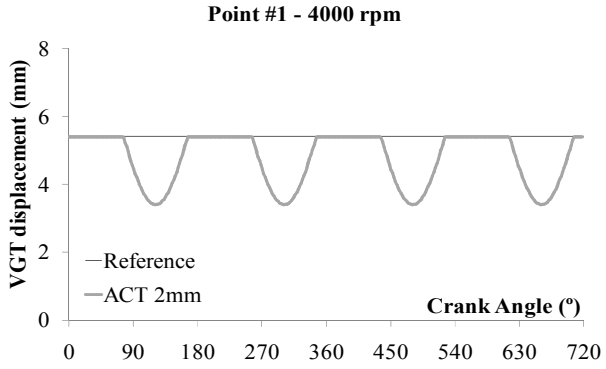

Figure 5. Half-sine wave displacement model

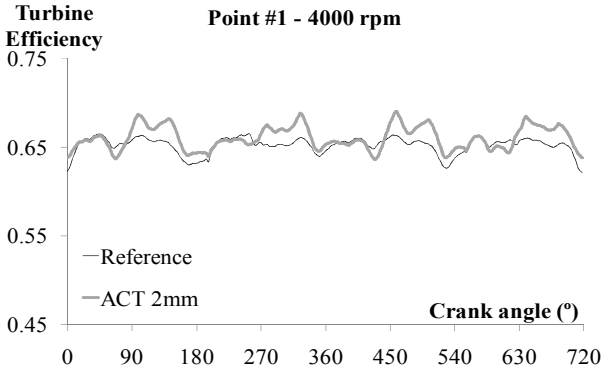

Figure 6. Half-sine wave instantaneous efficiency

So, although there is a gain in turbine efficiency, with this control strategy the operating conditions are changed and the engine performance can not be compared. Probably very similar results would be obtained if the turbine was closed to a fixed position as it will be working in an area closer to maximum efficiency. That is, using a constant VGT displacement about 5mm to obtain a result with the same air mass flow as the reference point.

6.4. Modified half - sine wave control

As a gain was observed when just using a half-sine wave control, a modification of this control strategy was applied in order to make results comparable with the base engine performance.

The same half-sine wave control in phase with the exhaust pressure valleys was maintained, but this time, the average turbine opening was kept constant so as to work at the same operating point. Figure 7 shows this new control strategy, this time for both test points and both opening amplitudes.

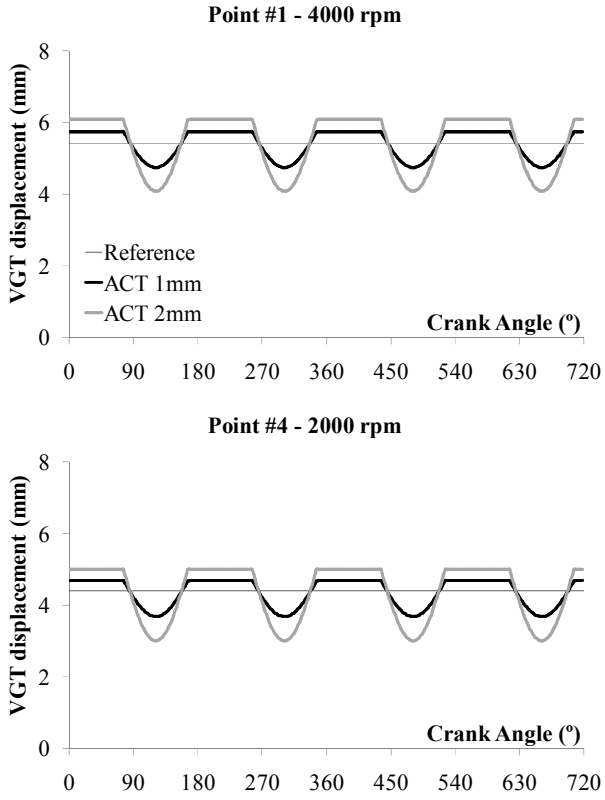

Figure 7. Modified half-sine displacement model

Table 6 and Figure 8 show the results for the different modified half-sine wave tests. As it can be observed, the results again are not as expected as the turbine efficiency barely changes and is not even close to the 1.33% gain for the original half-sine wave.

The reason for this occurrence is the same as with the previous sine wave experiments. In order to maintain the average VGT opening, the turbine has to be opened, so all the gain acquired when closed is lost completely when opened. This can be clearly seen in Figure 9.

Table 6. Modified half-sine mean efficiency results

	#1 - 4000 rpm		#4 - 2000 rpm	
	1mm	2mm	1mm	2mm
Reference	0.651	0.651	0.666	0.666
ACT	0.652	0.652	0.666	0.660
Difference	0.15%	0.15%	0%	-0.90%

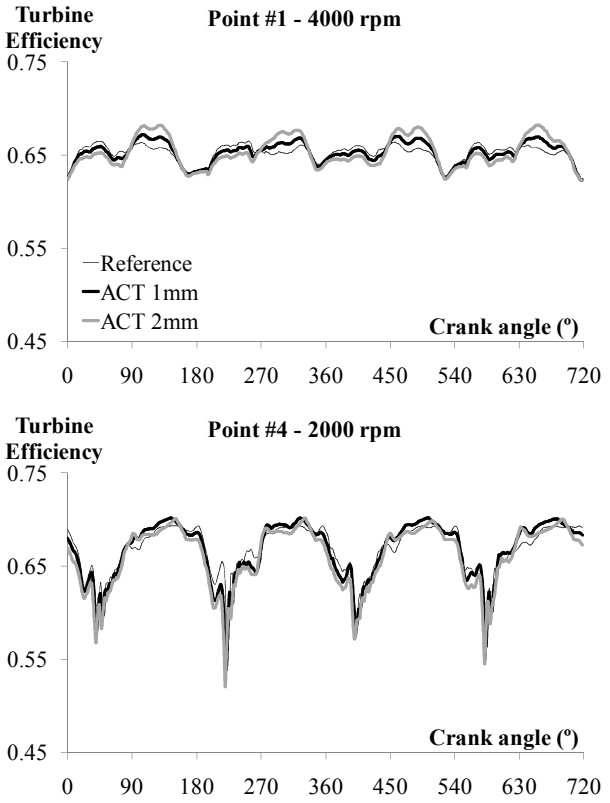

Figure 8. Half-sine wave instantaneous efficiency

The efficiency drop is not as big when using the modified half-sine wave in comparison with the sine wave because the operating loop seen in Figure 9 is not as wide as in Figure 4. When using the sine wave, the loop is wider so the turbine operates in much lower efficiency areas than in the last case.

7. CONCLUSION

Although the theory behind the ACT concept is very promising, the results do not seem to follow. As it can be seen, especially on the efficiency-displacement plots, getting close to the maximum efficiency region can not be done without moving to low efficiency regions if the operating point is kept. This implies that all the benefits obtained by getting close to maximum efficiency are lost when moving away.

The maximum gain in turbine efficiency has been a miserable 0.15% while in most of the cases the efficiency has dropped slightly. These changes in efficiency have had hardly any effect in the engine performance.

It is important to highlight that ACT can not improve the global performance of the engine as it was expected. This is due to the fact that the engine is the one that imposes the turbine operating point, limiting the advantages of ACT.

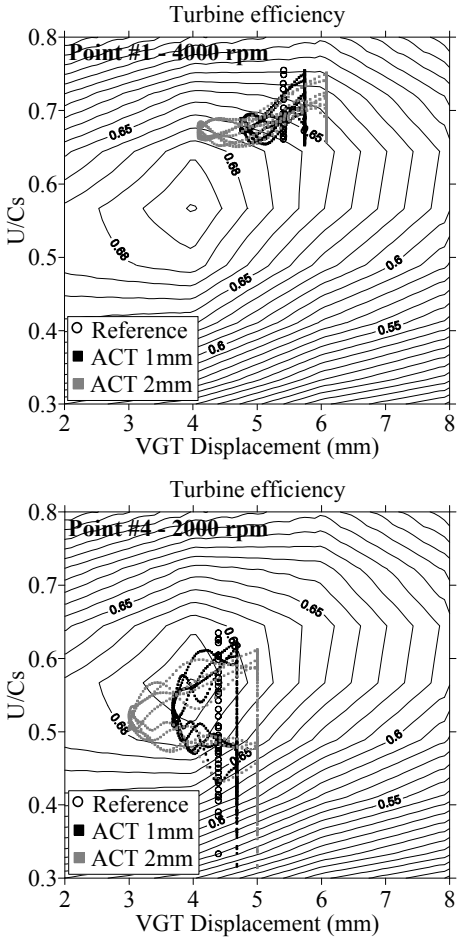

Figure 9. Half-sine wave efficiency-displacement plot

ACKNOWLEDGEMENT– The authors wish to thank Mr. Fabrice Vidal from PSA Peugeot Citroën (France) for his contribution to the work presented here.
The work has been partially funded by the Spain's Ministerio de Ciencia y Tecnología through project TRA2007-65433.

REFERENCES

Ferreaua H. J., Ortnerb P., Langthalerb P., del Reb L. and Diehla M., (2007) "Predictive control of a real-world Diesel engine using an extended online active set strategy", *Annual Reviews in Control, Volume **31**, Issue **2**, 293-301*

Filipi Z., Wang Y. and Assanis D. (2001) "Effect of Variable Geometry Turbine (VGT) on Diesel Engine and Vehicle System Transient Response", SAE 2001-01-1247

Galindo J, Luján J.M., Serrano J R, Dolz V. and Guilain S. (2006) "Description of a heat transfer model suitable to calculate transient processes of turbocharged diesel engines with one-dimensional gas-dynamic codes", *Applied Thermal Engineering Volume 26, Issue 1, 66-76*

Galindo J, Serrano J R, Arnau J R and Piqueras P. (2009a) "Description of a Semi-Independent Time Discretization Methodology for a One-Dimensional Gas Dynamics Model", *Journal of Engineering for Gas Turbines and Power, Volume 131, Issue 3, paper 034504.*

Galindo, J., Climent, H. ; Guardiola, C. ; Tiseira, A., (2009b) "On the effect of pulsating flow on surge margin of small centrifugal compressors for automotive engines", *Experimental Thermal and Fluid Science; Journal Volume: **33**; Journal Issue: **8***

García-Nieto S., Martínez M., Blasco X., and Sanchis J., (2008) "Nonlinear predictive control based on local model networks for air management in diesel engines" Control Engineering Practice Volume 16, Issue 12, 1399-1413.

Ghazikhani M., Davarpanaha M. and Mousavi Shaegha S.A., (2008) "An experimental study on the effects of different opening ranges of waste-gate on the exhaust soot emission of a turbo-charged DI diesel engine", Energy Conversion and Management; Volume 49, Issue 10, 2563-2569

Karamanis N., Martinez-Botas R. F., and C. C. Su (2001) "Mixed Flow Turbines: Inlet and Exit Flow Under Steady and Pulsating Conditions", *J. Turbomachinery, , Volume **123**, Issue **2**, 359-371*

Möller, C., Johansson, P., Grandin, B., and Lindstrom, F. (2005) Divided Exhaust Period, A Gas Exchange System for Turbocharged SI Engines, *SAE Paper* 2005-01-1150.

Pesiridis A. and Martinez-Botas R. F. (2007) "Experimental Evaluation of Active Flow Control Mixed-Flow Turbine for Automotive Turbocharger Application", *J. Turbomachinery, Volume **129**, Issue **1**, 44*

Roth, D.B., Keller, P. and Sisson, J. (2010) Valve-Event Modulated Boost System, *SAE Paper* 2010-01-1222.

Serrano J.R., Arnau F.J., Dolz V., Tiseira A., and Cervelló C., (2008) "A model of turbocharger radial turbines appropriate to be used in zero- and one-dimensional gas dynamics codes for internal combustion engines modeling", *Energy Conversion and Management Volume **49**, Issue **12**,. 3729-3745*

Smith F., Simpson R., (2005) "A Camshaft Torque Actuated Vane Style VCT Phaser", *SAE Paper 2005-01-0764*

Watson N., Janota M.S., (1982) "Turbocharging the internal combustion engine", *Macmillan London; ISBN 0333242904 (U.K.).*

Reception standby 2010-05-22 00:01:44	NUMERICAL STUDY OF THE IMPLEMENTATION OF AN ACTIVE CONTROL TURBOCHARGER ON AUTOMOTIVE DIESEL ENGINES	History
	Registration	Heat Transfer, Fluid and Thermal Engineering

History Print

Date	Status
2010-05-22	Manuscript submitted

Close

ANEXO V: OPTIMIZATION OF THE INLET AIR LINE OF AN AUTOMOTIVE TURBOCHARGER

Optimization of the Inlet Air Line of an Automotive Turbocharger.

Authors:

J.R. Serrano*, X. Margot, A. Tiseira, R. Gozalbo
Universidad Politécnica de Valencia. CMT-Motores Térmicos.
Camino de Vera, s/n. 46022. Valencia, SPAIN.

***Corresponding author:**
Phone: + 34 96 387 96 57
Fax: + 34 96 387 76 59
E-mail: jrserran@mot.upv.es

Abstract

This paper presents different aspects of air inlet behaviour near the inducer of a radial compressor and how the geometry can contribute to its stability and performance. Unfortunately the space reserved for installation of an automotive turbocharger in a vehicle is constantly being reduced, so it is necessary to study the effects that elbows and abrupt changes in flow directions originate on the compressor performance. The work presented in this paper studies the effect that different 90º elbows have on the compressor with respect to its ideal, straight, no-elbow configuration, in order to obtain the best possible elbow configuration.

The methodology followed has been to, initially, study different geometries in CFD code in order to obtain the best possible configuration. Then, several 90º elbows were constructed and characterised on a continuous flow test bench in order to validate the CFD results and to obtain optimum results. The elbows were then installed on a radial compressor and tested on a hot, continuous turbocharger test bench, where the compressor was characterised and maps were obtained with each different elbow. The results were compared with respect to the ideal, no-elbow configuration, which was taken as the base performance.

After analysing the results obtained, it is possible to observe that in most of the cases the elbows have a negative effect on the compression ratio, which tends to be reduced especially at high rotor velocities and high air mass flow. On the other hand, the effect on the surge limit seems to be positive, as the surge line shifts to lower air mass flows, although the maximum mass flow allowed is reduced. It seems as if the compressor map shifts to the left with a reduction in compression ratio. From theoretical and experimental study it has been concluded that flow uniformity index and pressure loss are the most important factors affecting the performance of the compressor.

Nomenclature

A_d = flow area of duct (m^2)
c = axial velocity (m/s)
C_D = discharge coefficient
d = duct
K = pressure loss coefficient
$\dot{m}$ = mass flow rate (kg/s)
Δp = pressure loss rise (bar)
p_{amb} = ambient pressure (bar)
p_s = pressure in setting tank (bar)
R = reference gas constant (air) (J/kg.K)
T_{amb} = ambient temperature (K)
u = flow velocity (m/s)
W_c = compressor work (J)

Greek symbols

ρ = density (kg/m^3)
λ = angle of swirl
γ = ratio of heat capacities (1.4)
π_c = compression ratio
η = efficiency
ξ = uniformity index

Subscripts

1 = compressor inlet
2 = compressor outlet
a = axial

Acronyms

IC = Internal combustion
CFD = Computational fluid dynamics
FFT = Fast Fourier Transform

Keyword: turbocharging compressor, inlet at 90º, depression, surge, uniformity, pressure drop

1. Introduction

Turbochargers have been in common use for at least the past 50 years to enhance the performance of internal combustion (IC) engines. Turbocharged diesel engines are standard and turbocharging is becoming increasingly widespread for spark ignition engines as well. This trend is set to continue with the ongoing drive for improved fuel economy and increasingly tight emissions legislation, where engine downsizing enabled by turbocharging is already playing a significant role.

Turbocharging is a form of supercharging, which is the pressurised air induction of an IC engine. A turbocharger is a machine which is mechanically separate from the IC engine and consists of a centrifugal compressor directly coupled to a radial turbine, which is driven by the, otherwise wasted, exhaust gases.

Radial compressors are limited at high flow rates by choke and at low flow rates by flow instability known as surge. The phenomenon of compressor surge is basically a problem of air stalling which leads to flow reversal and recirculation within the compressor, which can result in either a local instability and sound problems or a complete compressor instability and unacceptable drivability issues in a vehicle. The stalling of air is likely to occur when air flow is low and the pressure gradient is too high, therefore the surge limit is the leftmost border in any compressor map.

In normal engine operating conditions, surge had never been a problem as, traditionally, the compressor did not operate close to the surge line. But in recent years the demand for higher low engine speed torque, implies that high compressor pressure ratios are required at low mass flows. This translates in the compressor having to operate very close to the surge limit.

A simple solution to solve this problem would be to use a smaller compressor which could operate further away from the surge line at the required low mass flow. Unfortunately, a smaller compressor also translates into a lower maximum mass flow, as the compressor will choke earlier and would imply not being appropriate for the engine when operating at full load.

The admission line design can influence the compressor surge limit, which can be modified or affected by altering the inlet or outlet geometry of the compressor. According to White et al [1], the impossibility of placing the correct admission line when the compressor is installed on a vehicle can lead to significant problems, as the surge limit line will be different to the one determined by the manufacturer. An incorrect admission line can create great instability and non uniform flow at the inducer or blade leading edges, causing a phenomenon known as rotating stall which leads to compressor surge.

The literature reports that in the case of axial compressors they commonly exhibit rotating stall before surge [2]. The rotating stall not only depends on the compressor blade characteristics but also on the system in which it is installed and this is also extensive to the centrifugal compressors [3]. It is possible to consider the inlet distortions as the primary cause of the rotating stall phenomena as it is the main factor affecting the uniformity of the flow [4]. Surge and efficiency are known to be significantly influenced by the flow discharge characteristics on the impellers, which mainly depend on the behaviour of the airflow through the inducer [5]. Some distortions, evidenced in the flow, are caused by the elements that compose the inlet configuration line, inducing undesirable instabilities that reduce the compressor efficiency or produced compressor surge [6]. These distortions can be severe or light, but in any case they affect the compressor performance, so it is evidently important to study the inlet admission geometry line when a compressor is installed.

In recent years, when turbocharging the automotive Diesel engines, it is very common to find this type of problems in the inlet geometry compressor admission. This is due to the fact that the space reserved for the installation of the turbocharging system is being constantly reduced, mainly due to engine downsizing as well as due to the other auxiliary elements installed around the engine. Engine manufacturers want to pack everything together and make engines as compact as possible in order to reduce space, weight and cost.

In many modern engine configurations, due to the lack of space, it is becoming very common to have an elbow in the admission duct very close to the inducer of the centrifugal compressor [7]. Therefore, the main purpose of this work is to analyse the effect that 90º elbows have on the compressor performance when installed close to the inducer and study different elbow configurations and geometries. All the elbows tested are designed to fit in the same space and are located at the same distance from the compressor inducer, but they differ in their external and internal geometry.

The different geometries proposed have been designed using a CFD code. Furthermore, they have been tested experimentally on a cold, continuous flow test rig. With the results of the experimental characterisation and the CFD modelling, a complete study of the effect of the elbows on the compressor behaviour has been conducted for some of the designed elbows.

Apart from this, an extra experiment has been conducted, which consists in generating a depression at the compressor inlet with a straight (no-elbow) configuration. The depression was generated with a restriction (automatic valve) placed close to the compressor, at the same distance where the elbow would be. The literature says that the compressor performance is not affected or it has no important implications [8], although it seems to produce an improvement in the surge limit area.

2. Elbows Configuration

The elbows have been developed considering different designs with the same main structure and occupying the same space. All the elbows had a circular outlet section of diameter 39.2mm, imposed by the inducer diameter of the compressor; and a rectangular entry section of 20x60mm. The entry section shape was imposed by the strict limitations in space available in the studied car and it is representative of modern cars [7]. The space between the inducer and the engine was limited to 35mm (Figure 1) so in order to have a reasonable radius at the elbow corner, it was decided that a rectangular entry section of the cited dimensions had to be used. The dimensions of the rectangular section were selected in order to match the area of the inducer as these would decrease the pressure drop produced by the change in section. Another imposed value in the design was that the elbows had to have a curvature of 90º.

The methodology used in the design was to compare the flow behaviour through the elbow and its evolution till the exit area, where the compressor inducer will be placed. The different geometries have been studied and parameters such as the flow uniformity and pressure loss indexes have been obtained from the CFD model. The different elbow configurations tested are further listed and represented schematically in Figure 1.

- V1: curvature radius 0mm.
- V2: Sharp elbow of curvature radius 5 mm.
- V3: Smoother elbow with large inner elbow radius of 15.5 mm.
- V4, V5, V6 and V7: Sharp V2 type elbows with internal directional plates of different shapes and locations.
- V8: Sharp V2 type elbow with internal wedge located before the elbow.
- V9: Smooth V3 type elbow with two flat internal plates at incidence
- V10: Similar to V3 type elbow but with the two internal curved guide vanes placed such that they divide the duct in three channels of the same cross-sectional area
- V11: Smooth V3 type elbow with one internal curved guide vane placed such that it divides the duct in two channels of the same cross-sectional area.

3. CFD evaluation

The method used to find an optimum solution for the elbows has been carried out using a mathematical 3D code. FLUENT 6.0 commercial CFD program has been employed for all the calculations with the segregated implicit solver and the standard k-ε turbulence model. The following assumptions have been made to reduce calculation time:

- The symmetry of the flow with respect to a mid-plane passing through the elbow axis allows reducing the number of cells, as only half the geometry needs to be calculated.

- The airflow is considered incompressible and therefore density is constant throughout the domain. The error made by this simplification is very low and does not affect the general conclusions of the comparative study performed here.

- Possible transitional and unsteady effects are also neglected. The convergence criteria used for the steady state calculations are based on small residuals (order 10e-4) and a stabilisation of the mass flow rate and the velocity profile at the duct exit.

- A pressure difference between inlet and outlet of 1500 Pa has been imposed by the inflow/outflow pressure boundary conditions.

A structured mesh criterion was adopted with 26500 number of cells, value chosen after a mesh independence study. Furthermore, to avoid contour condition problems and obtain continuous flow at the outlet, a longer exit tube was used. The general mesh characteristics and contour conditions can be observed in Figure 2.

Figure 3 shows the uniformity index and pressure loss coefficient for the same Δp (1500 Pa) for all the elbows calculated, V1 to V13. Pressure loss coefficient (K) is defined as shown in equation (1).

$$K = \frac{\Delta p}{0.5 \rho u^2} \quad (1)$$

Where:

ρ = density (kg/m^3)
u = inlet flow velocity (m/s)

The flow uniformity index (γ) has been defined on the basis of the axial velocity at the entry section of the compressor. It takes the value 1 for the straight duct case [9].

$$\xi = 1 - \sum_i \frac{|(c_i - c_m) \cdot a_i|}{2 \cdot c_m \cdot A} \quad (2)$$

Where:

W_i = axial velocity in cell *i* of the compressor inlet
W_m = axial average velocity at the compressor inlet section
a^i = area of cell *i*.
A = area of the cross section

After analysing the results, the following four elbows were selected to be built and tested in the continuous flow and turbocharger test rigs due to the following characteristics:

- Elbow V1: curvature radius 0º. Used as reference of worst case.
- Elbow V3: lowest pressure drop coefficient
- Elbow V9: moderate pressure loss coefficient and high uniformity index
- Elbow V12: highest uniformity index

Figure 4 shows the CFD velocity pattern study for each of the four selected elbows. The circle magnified in each image represents the transversal inducer area. In the V1 case, it can be clearly seen that the flow is not well distributed in this section, while on the other three cases the flow distribution has been greatly improved. Elbow V1 was the most unstable, as proved by Figure 3 and Figure 4 in which it can be seen that it has the highest value of pressure loss of the selected elbows and the lower value of uniformity index. This elbow will be used as the base worst test case from which to make comparisons.

It has to be recalled that the objective of the CFD study is just for comparison and no further studies than the ones showed were carried out as the only purpose of this study was to evaluate and select the different geometries before they were built and tested.

4. Continuous flow test rig

To quantify the pressure loss coefficients of each elbow built, a continuous flow test rig is used. The methodology followed consists of two tests: A and B. Test A will be used to determine the pressure loss coefficient of the ducts and flanges that will be used

to couple and fix the elbows to the rig in test B. Therefore using the results of both experiments, the pressure loss produced by the elbow can be established. Figure 5 shows a scheme of the experimental tests A and B.

The methodology used to calculate the pressure loss produced by the elbow is the following:

Every pressure loss coefficient (K) referred to the ducts 1 and 2 is added resulting in a total K of the test A as shown in equation 3:

$$K_A = K_{d1i} + K_{d1} + K_{d2} + K_{d2e} \quad (3)$$

where:

$$K_A = \frac{\Delta p_A}{0.5 \rho_i u_i^2} \quad (4)$$

and the density ρ_i is calculated from ambient conditions at the inlet of duct 1.

Once the value of K_A has been obtained, the test B is performed with the same elements of test A plus the 90º elbow in order to obtain its pressure loss coefficient.

$$K_B = K_{d1i} + K_{d1} + K_{elbow} + K_{d2} + K_{d2e} \quad (5)$$

where:

$$K_B = \frac{\Delta p_B}{0.5 \rho_i u_i^2} \quad (6)$$

Once K_B is obtained from test B, the subtraction of the two K coefficients is performed and the K value obtained corresponds to the tested element, in this case the 90º elbow.

$$K_{elbow} = K_B - K_A \quad (7)$$

To calculate the pressure drop Δp_{elbow} in the flow through the elbow, the obtained K_{elbow} value is used as shows equation (8):

$$\Delta p_{elbow} = K_{elbow} 0.5 \rho_{iB} u_{iB}^2 \quad (8)$$

The results extracted from these tests are shown in Figure 6, where the pressure drop and the loss coefficient (K) is plotted versus the mass flow rate for every tested elbow (V1, V3, V9 and V12). Although the tests were carried out until a mass flow of 0.15 kg/s, the results over 0.1 kg/s should not be considered as valid as they might have a significant error. This is because above this value, the velocity of the flow was over Mach 0.2, limit at which compressible flow phenomena starts to appear, making the hypothesis of incompressible flow used to calculate K_{elbow} and Δp_{elbow} not valid. It is also interesting to note that the maximum possible mass flow achieved for elbow V12 was of 0.09 kg/s due to flutter produced by the internal guide vanes.

Figure 6 also shows the evolution of C_D with respect to the air mass flow. This coefficient refers to the loss of effective area produced by the elbow geometry, and can be seen that drastically drops after 0.1 kg/s. To calculate the C_D coefficient the expression (9) has been used.

$$C_D = \frac{\dot{m}_{real}}{\dot{m}_{theorical}} \qquad (9)$$

Where the theoretic mass flow rate is calculated by Eq. 10

$$\dot{m}_{theorical} = A_d\, p_{amb} \sqrt{\frac{2\gamma}{R(\gamma-1)T_{amb}}} \sqrt{\left(\frac{p_s}{p_{amb}}\right)^{\frac{2}{\gamma}} - \left(\frac{p_s}{p_{amb}}\right)^{\frac{\gamma+1}{\gamma}}} \qquad (10)$$

From these experiments the general conclusion is that the maximum pressure drop has been observed in elbows V1 and V9, just as it was predicted with the CFD tests. On the other hand, the elbow that produces the lowest pressure drop is V3. Very similar results have been observed when analysing the discharge coefficient (C_D), having the highest value the elbow V3 and the lowest elbow V9. It is interesting to highlight that the C_D value for V1 is below 0.65, implying that only 65% of the geometric area is used by the flow.

5. Compressor and elbow tests in a specific rig

The experimental tests with the centrifugal compressor and the elbows were carried out in the continuous, hot flow turbocharger test bench, where the compressor can be characterised and its map can be obtained [10]. In this experimental facility, the surge line is determined analysing the instantaneous pressure recorded upstream and downstream of the compressor. This is done by a sequential analysis of all the measured points applying FFT [10]. The compressor is characterised by recording the values of rotor speed, pressure ratio, air mass flow and temperatures. Compressor efficiency and total to total compression ratio are calculated.

Figure 7 shows a diagram of the turbocharger test bench installation with the instrumentation used and its location. The number and position of the pressure and temperature transducers satisfy the SAE standards [11]. The main instrumentation used in these tests is the following:

- Compressor air mass flow rate**:** Hot-film anemometers (range: 0 – 720 kg/h)
- Inlet and output compressor instantaneous pressures**:** Piezoresistive traducers (range: 0 – 5 bar)
- Inlet and output compressor temperatures**: T**hermocouples type K (range : 20 – 1300 ºC)
- Turbocharger speed**:** Eddy current sensor (range: 0 – 400K min^{-1})

An initial test with a straight pipe line at the compressor inlet was carried out in order to obtain the compressor map which will be used as a base for comparison. The

same test was repeated for each of the selected elbows, as these permitted comparisons between the compressor maps with and without the 90º elbows.

Figure 8 shows the results of these experiments and as it can be seen, all the tested elbows are not just compared with the original straight duct but also with V1 elbow, as it was the worst reference elbow design with the lowest uniformity index and the highest pressure drop. This permitted not just comparing between an elbow and a straight configuration, but between a bad design elbow and a more sophisticated design.

The effects of installed elbow V1 can be easily spotted when comparing with the original compressor configuration. The surge limit seems to be unaffected over compression ratios of 2, but below this limit using elbow V1, the surge limit shifts to the right, meaning that the compressor will surge at higher mass flows. This is obviously a negative effect as it reduces the mass flow range. But apart from this, V1 elbow also has very negative effects on the pressure ratio and on the maximum flow rate. As it can be seen, for the same rotor speed, the compression ratio is always lower. This can be clearly seen at the highest velocities where the difference is greater. The maximum flow rate has also been reduced significantly when using this elbow, making the admissible operating flow range even smaller.

On the other hand, by observing Figure 8a it can be seen that the V12 elbow configuration manages to shift the surge limit to the left, implying that the compressor will surge at lower mass flows which is always a benefit. Unfortunately, just as with elbow V1, the compression ratios achieved are smaller than with the original configuration. This time though, the effect is slightly different as the drop in compression ratio does not come with the increase in rotor speed but with the increase in mass flow. For a given speed and low mass flows, the values of compression ratio are similar to the original results, but as mass flow increase, compression ratio falls and results become very similar to those with elbow V1. Also, just like with V1, the maximum mass flow allowed is reduced, but this time, as the surge line is shifted to the left, the admissible operating flow range does not vary significantly.

Alternatively, the results obtained when testing elbow V3 can be seen in Figure 8b. Once again, the surge limit has been shifted to the left, benefiting the compressor behaviour at low mass flows, but as it seems common with the elbow configuration, the compression ratio also drops. This time though it shows an opposite trend to elbow V12. For a given rotor speed and low mass flow, the compression ratio is the same as with elbow V1, but as the mass flow increases, the compression ratio increases significantly close to values observed with the original no-elbow configuration. This is because the lowest pressure drop coefficient was measured with V3 elbow.

Figure 8c shows the effect that elbow V9 has on the compressor map. Again, the surge limit has been shifted to the left, but the compression ratios have dropped significantly showing very similar results to those when using V1 elbow, as expected considering Figure 6b results

The reason why these effects are happening will be further discussed. In Figure 8d the results of all the elbows are combined and only the region of high compression ratio and low mass flow is shown for simplicity. This figure will help to better understand further discussion.

6. Discussion of results

In order to understand why the surge limits change, it is fundamental to understand why surge happens. In the impeller of a compressor, the airflow pressure is higher downstream than upstream, therefore creating a pressure gradient opposite to the streamline direction. As the mass flow rate decreases, for a constant rotor velocity, the adverse pressure gradient increases, which at the same time increments the viscous shear stress at the impeller blades. At a certain point of the impeller wall, the flow velocity becomes zero because the momentum in the streamline adjacent to the wall is insufficient to overcome the adverse pressure gradient and viscous stress. Unfortunately this situation deflects the streamlines and affects directly the boundary layer, which increases its thickness. This situation will create reverse flow that will increase in the surface of impeller wall as the compressor gets closer to the surge point. When the reverse flow becomes more important than the main flow, the rotor compressor velocity is insufficient to overcome the magnitude of the adverse pressure gradient, therefore the streamlines completely deflect from the impeller wall, creating an abrupt stall for all the rotor impellers and consequently generating surge.

The main parameter that affects the surge limit is the uniformity index of the flow in the elbows. Figure 8d shows the elbows with the highest uniformity index (V3, V9 and V12) and a benefit in the surge limit can be observed. On the other hand, V1 elbow that has a uniformity index of 0.742 does not show this behaviour. As it is shown in Figure 3, the CFD analysis shows that in an important part of the area at the inducer the velocity of the flow is zero for elbow V1. This has a very negative impact on the uniformity of the flow, making it very irregular at the impeller's surface, resulting in distortions that will cause rotating stall and surge.

Discharge coefficient (C_D) is another important parameter that affects the surge limit. As for all the cases this value is below 1 and the mass flow has not been changed, according to the continuity equation, this implies that the velocity of the flow at the inducer is higher. It has to be recalled that surge occurs when the reverse flow, produced by the adverse pressure gradient, is more important than the main flow; therefore, increasing the velocity of the main flow at the compressor inlet will delay surge and make the compressor more stable. This effect, combined with a more uniform flow, benefits the compressor behaviour at low mass flows and moves the surge limit to the left of the map.

It is important to note that although the C_D of elbow V1 is very low, which should be theoretically beneficial in shifting the surge limit to the left, its uniformity index is very low with high asymmetric flow cancelling all the other possible benefits. On the other hand elbow V3 and V12, show a C_D closer to 1, which is not so beneficial for surge, but this is compensated by having a very high uniformity index. V3 elbow shows the best characteristics (Figure 8d) at high compression ratios.

With respect to the drop in compression ratio when compared to the original no-elbow case, the explanation is pretty simple: it is due to the pressure loss produced by the different elbow configurations. Although the compressor is compressing at the same ratio, the fact that the inlet pressure at the inducer is lower (due to the elbows pressure loss), implies that the pressure at the outlet will also be lower. As it can be seen in

Figure 7, the inlet pressure sensor is not installed at the inducer, but at the inlet of the elbow, so when calculating the compression ratio, the pressure loss produced by the elbow is included in the calculation.

In order to deduct the effect of the pressure loss produced by the elbow and observe the real compression ratio, the pressure loss calculated in the continuous flow test rig for all the elbows has been subtracted from the elbow inlet pressure, so as to obtain the pressure at the inducer. This is shown in equation 11, where Δp is the pressure loss of every elbow which varies with the mass flow rate.

$$\pi_{\text{with elbow}} = \frac{p_{\text{outlet}}}{p_{\text{elbow inlet}}} < \pi_{\text{without elbow}} = \frac{p_{\text{outlet}}}{p_{\text{elbow inlet}} - \Delta p_{\text{elbow}}} \qquad (11)$$

The new results are plotted in Figure 9, where it can be seen that with this correction, there is hardly any difference in compression ratio, except at the maximum tested rotor speed. In this case, it can be observed how the elbows with higher uniformity index (V9 and V12) have the same compression ratio as the original test case with no elbow; while on the other hand, the elbows with a lower uniformity index show reduced compression ratios at high rotor speeds.

Figure 10 shows the plot of the compressor efficiency with respect to mass flow rate for three different rotor speeds, comparing also the effect of adding or subtracting the pressure loss produced by the different elbow configurations. As it can be seen, when the pressure loss is subtracted, the compressor efficiency seems almost unaffected having the best results with the elbows V3 and V12, which show the lowest pressure drop coefficient. While if Δp is included in the calculations, as the mass flow increases, the efficiency reduces with respect to the original no-elbow case.

This can be explained using an enthalpy-entropy diagram as shown in Figure 11. With a straight duct fitted on the compressor, the inlet pressure would be atmospheric pressure (p_{atm}), while its exit pressure would be p_2'. On the other hand, if an elbow is installed at the compressor inlet and the pressure still measured from the compressor inducer (p_1) to the compressor exit (p_2), the compression ratio would still be the same as before, but both inlet and outlet pressures would be lower, due to the pressure drop produced by the elbow at the compressor inlet. Conversely, if the pressure is measured from the elbow inlet (p_{atm}) to the compressor exit (p_2), the compression ratio is reduced as it includes the loss in pressure produced by the elbow. This is the reason why the efficiency is lower when taking into account the complete system (elbow + compressor). The elbow produces a pressure loss which affects the efficiency of the compressor. If this loss is subtracted, as seen in Figure 10, there is virtually no difference in efficiency.

$$\eta_{p_{atm}-p_2'} = \eta_{p_1-p_2} > \eta_{p_{atm}-p_2} \qquad (12)$$

7. Influence of the lower pressure at the compressor inlet.

A second series of tests were carried out in order to experimentally confirm that the main parameters that affect the surge limit on a radial compressor are uniformity index and flow velocity. Flow velocity was achieved by reducing C_D as discussed in previous sections.

These tests were carried out using a straight, no-elbow duct with a valve upstream in order to generate a pressure drop. The main function of this valve is to create an increase in speed and a reduction in pressure at the compressor inducer, while the mass flow is kept constant. These can be explained by means of the continuity equation, as if the mass flow is kept constant and the flow density is reduced (higher pressure drop), this will produce an increase in flow speed. Two different pressure drops were measured: 150mbar and 300mbar. The valve was also positioned 14 diameters upstream of the mass flow measuring plane placed 10 diameters before the inducer. These distances were selected in order to obtain a good uniformity in the flow. A sketch of the installation can be seen in Figure 12.

As it can be observed in the results shown in Figure 13 the influence of the depression at the compressor inducer has almost negligible effects on the compression ratio. This was the expected behaviour attending to the results obtained, where the pressure drop was discounted in the 90º elbows tests. The variables represented in these figures have been always corrected with the flow conditions just upstream the compressor.

The surge line has been shifted to the left in both cases confirming that flow velocity at the inducer and flow uniformity are the main parameters affecting surge. Unfortunately, the compressor choke line has also shifted to the left, reducing the maximum mass flow in the compressor. So this set up is just for phenomena demonstration, because although it shows very positive results with respect to the surge line limit, all this benefits are lost with respect to the choke line limit, as the mass flow operating range of the compressor has been reduced.

8. Conclusions

Two phenomena have been found to have a major effect on the compressor performance when an elbow with a 90º corner is installed at the compressor inducer: the flow uniformity index and the pressure drop coefficient. Both effects appear interdependent and mainly affecting the surge limit of the compressor and the compression ratio. The higher the uniformity index the better, as there will be no irregularities in the flow at the impeller's surface. On the other hand, a high pressure drop means low discharge coefficient implying high flow velocity at the inlet and delaying surge, but it has the negative effect of reducing the compression ratio, due to the pressure loss produced at the compressor inlet. Also, although a low discharge coefficient is beneficial for surge, it is disadvantageous for choke. As shown, although the surge line shifts to the left, the choke does the same, so the maximum flow allowed by the compressor is reduced.

Therefore it is important to design elbows with the maximum uniformity index possible, as this has no drawbacks, and with the lowest possible pressure drop, as although it is beneficial for surge it has other major downsides, so it is preferred to be kept as low as possible.

So attaining to these conclusions and the results presented in this article, that the elbow V12 can be confirmed as the most optimum solution of all the elbows tested, having the highest uniformity index and lowest discharge coefficient. Nevertheless, elbow V13 should be even better due to a small difference in uniformity index (ξ) and sensibly lower pressure drop.

References

1. White, F.M., "Fluid Mechanics", McGraw-Hill, Inc., 2003, ISBN-0-07-240217-2.
2. Moore, F.K., "A Theory of Post-Stall Transient in Multistage Axial Compressor Systems", NASA, cr 3878, March 1985.
3. Siedel, U., Chen, J., Haupt, U., Hasemann, H., Jin, D., Rautenberg, "Rotating Stall Flow and Dangerous Blade Excitation of Centrifugal Compressor Impeller, Part 1 Phenomenon of Large –Number Stall Cells", ASME 1991, Paper No. 91-GT-102.
4. Soranna, F., Chow, Y.C., Uzol, O., Katz, J., "The Effect on Inlet Guide Vanes Wake Impingement on the Flow Structure and Turbulence around a Rotor Blade", ASME Journal of Turbomachinery 2006, Vol.128, pp.82-95.
5. Engada, A., Kim, Y., Aungier, R., Direnzi, G., "The Inlet Flow Structure of Centrifugal Compressor Stage and Its Influence on the Compressor Performance", ASME, Journal of Fluid Engineering , September 2003, Vol. 125, pp. 779-785.
6. Elder, R.L., Gill, M.E., "A Discussion of the Factors Affecting Surge in Centrifugal Compressors", ASME, Journal of Engineering for Gas Turbines and Power, April 1985, Vol. 107, pp. 499-506.
7. J.Galindo, J.R.Serrano, X.Margot, A.Tiseira, N.Schorn, H.Kindl. "Potential of flow pre-whirl at the compressor inlet of automotive engine turbochargers to enlarge surge margin and overcome packaging limitations". International Journal of Heat and Fluid Flow 28 (2007), pp. 374-387.
8. Pampreen, R.C., "Compressor Surge and Stall", 1993, Concepts ETI, Inc ISBN 0-933283-05-9.
9. Kindl, H., Schorn, N., Schulte, H., Serrano, J.R., Margot, X., Donayre J.C., "Influence of Varius Compressor Inlet Designs on Compressor Performance", September 2004 Valencia España THIESEL 2004, pp. 103-115.
10. J.Galindo, J.R.Serrano, C.Guardiola, C.Cervelló. "Surge limit definition in a specific test bench for the characterization of automotive turbochargers". Experimental Thermal and Fluid Science 30 (2006), pp. 449-462.
11. Supercharger Testing Standard, 1995. SAE J1723 ISSUED Aug95. 909 Society of Automotive Engineers, Inc.

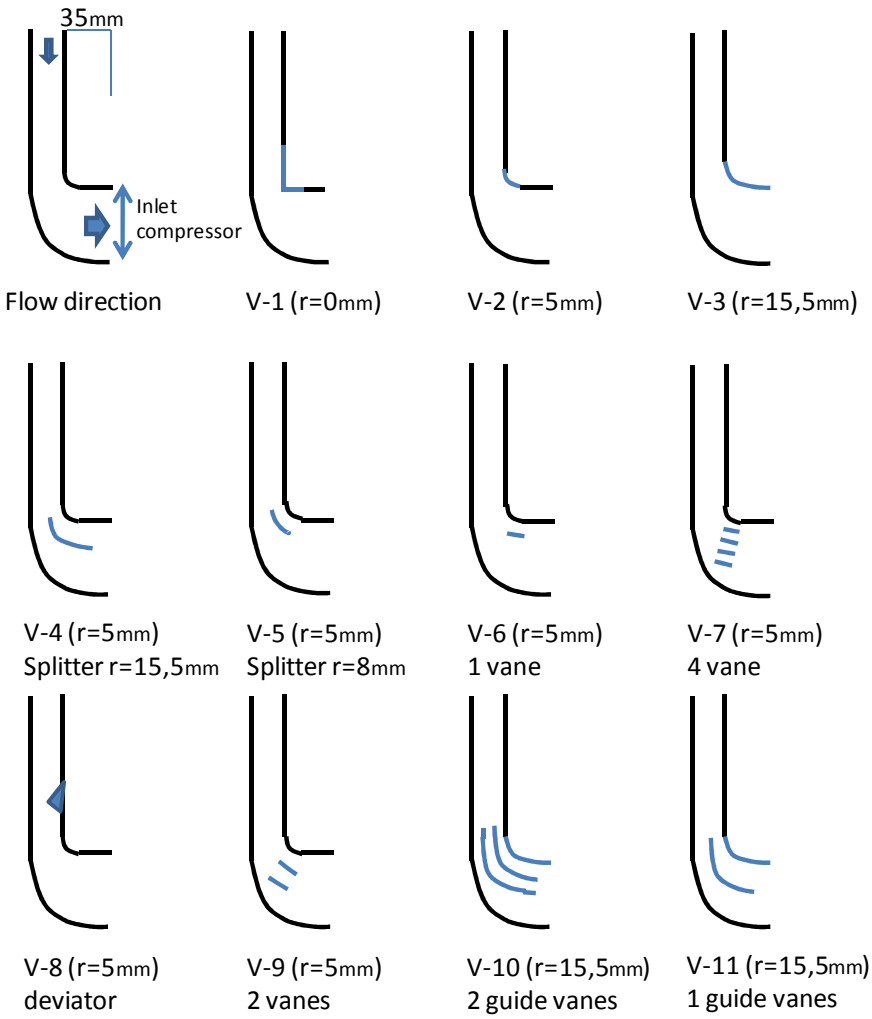

Figure 1. Variant of elbows propose

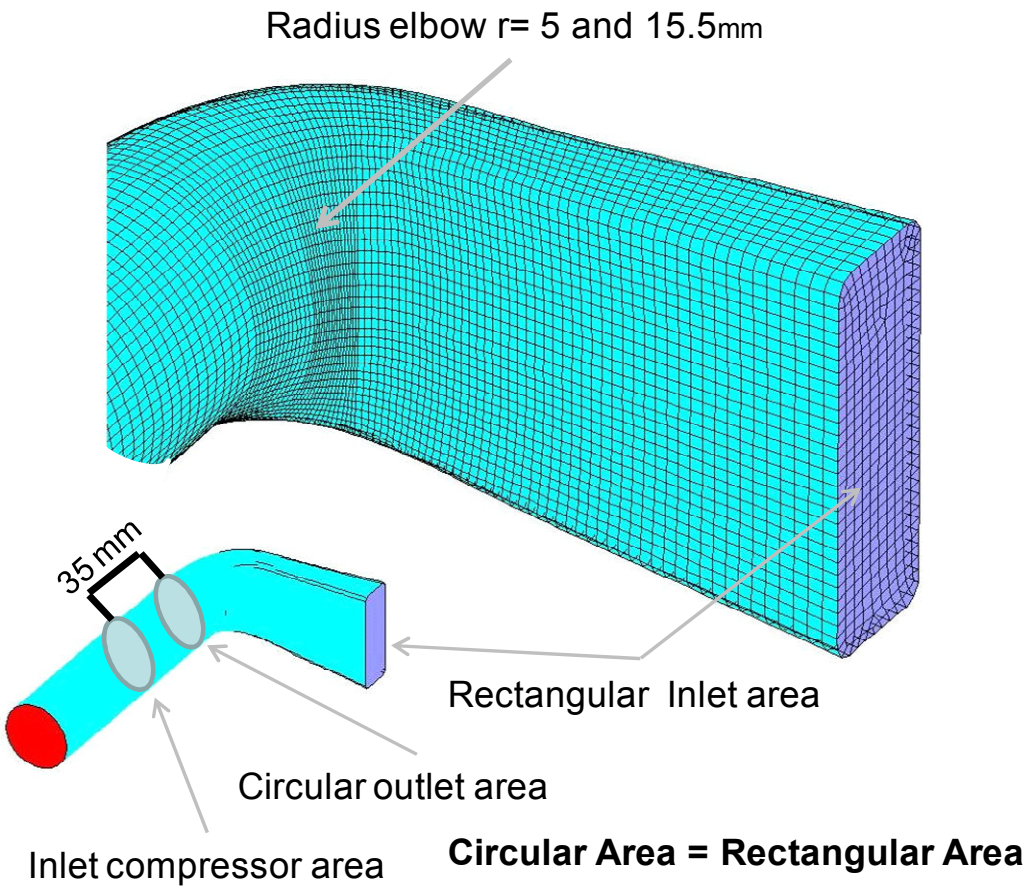

Figure 2. Characteristic mesh used to calculate the flow behaviour inside the elbows

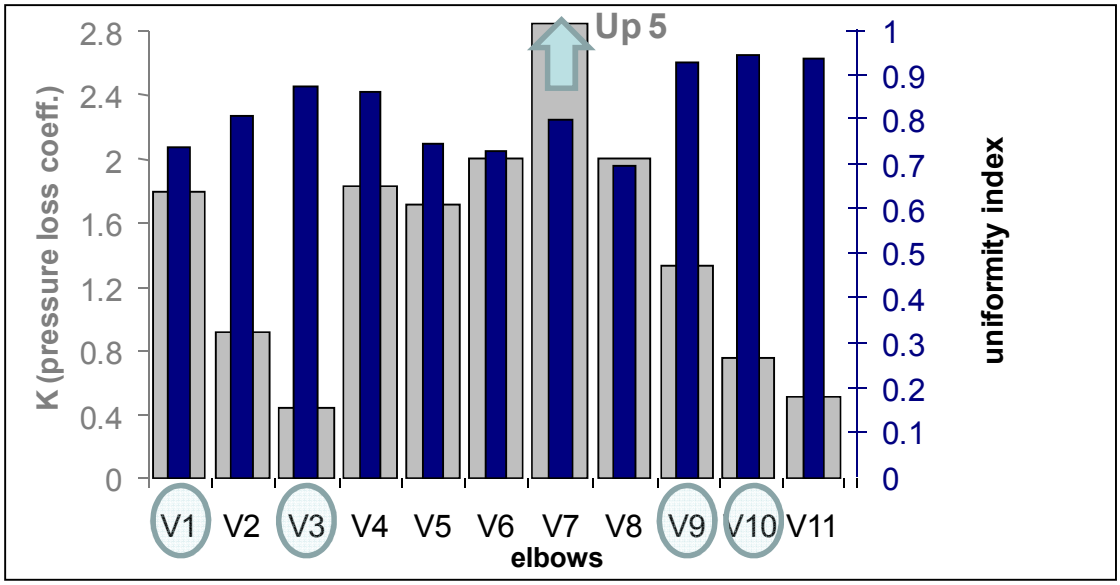

Figure 3. Graphic corresponding to uniformity index and pressure loss for each elbow at 0.1 kg/s

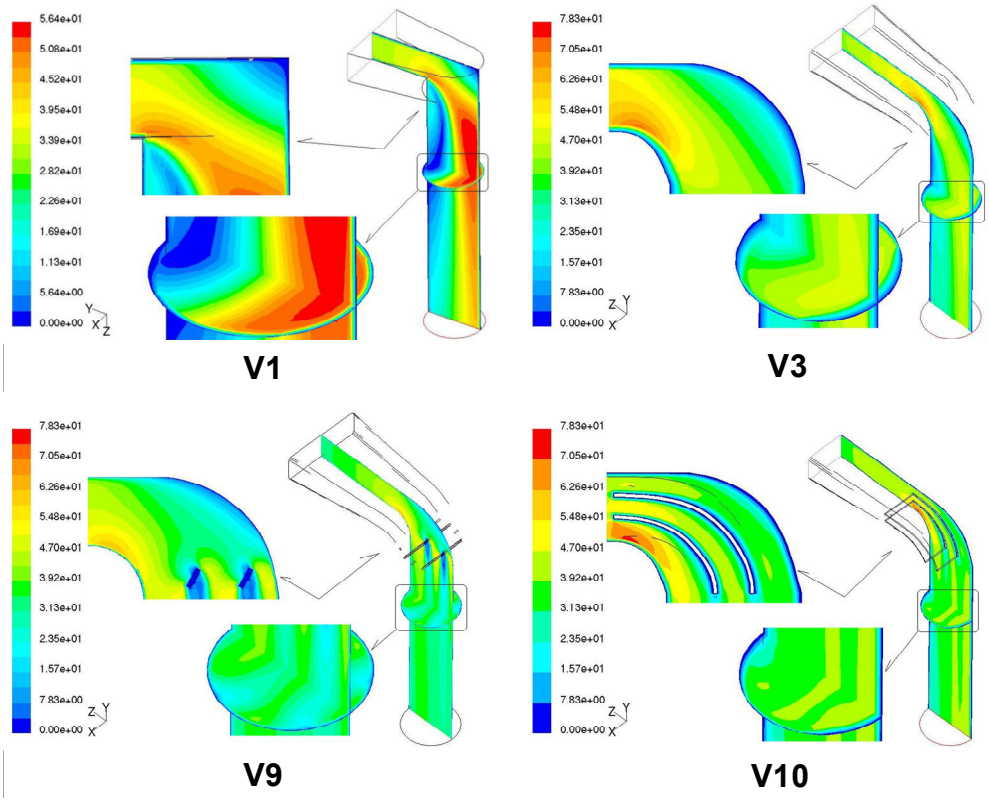

Figure 4. Pattern flow described by the calculus CFD (the circle shows the inducer area), the V1, V3, V9 and V12 are the elbows built.

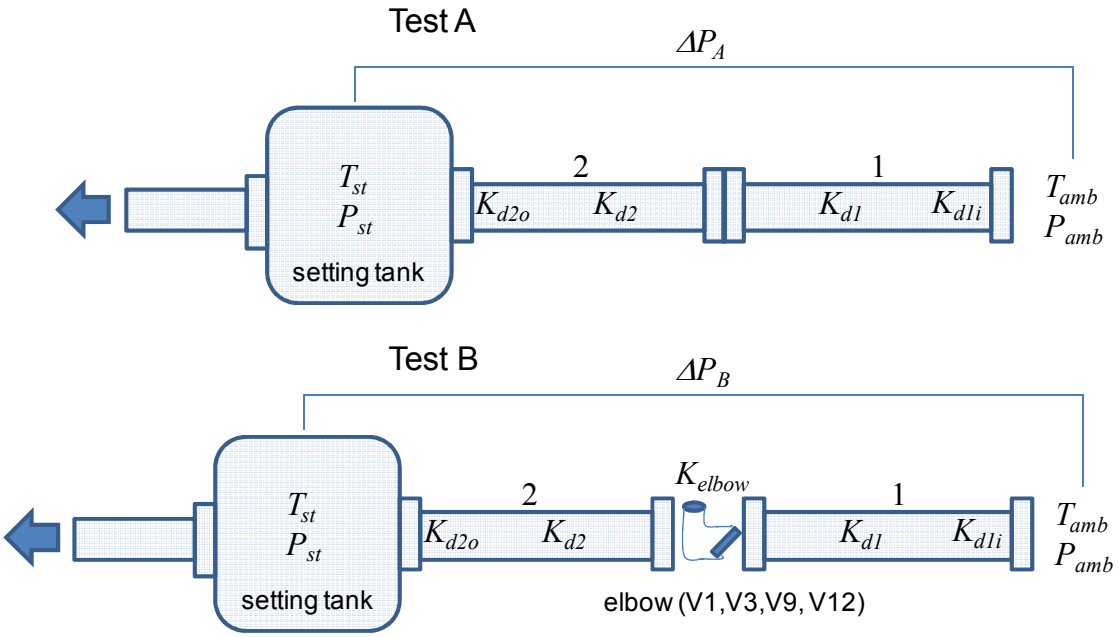

Figure 5. Methodology implemented in the test rig using two tests A and B, to calculate the pressure drop caused by the elbows built.

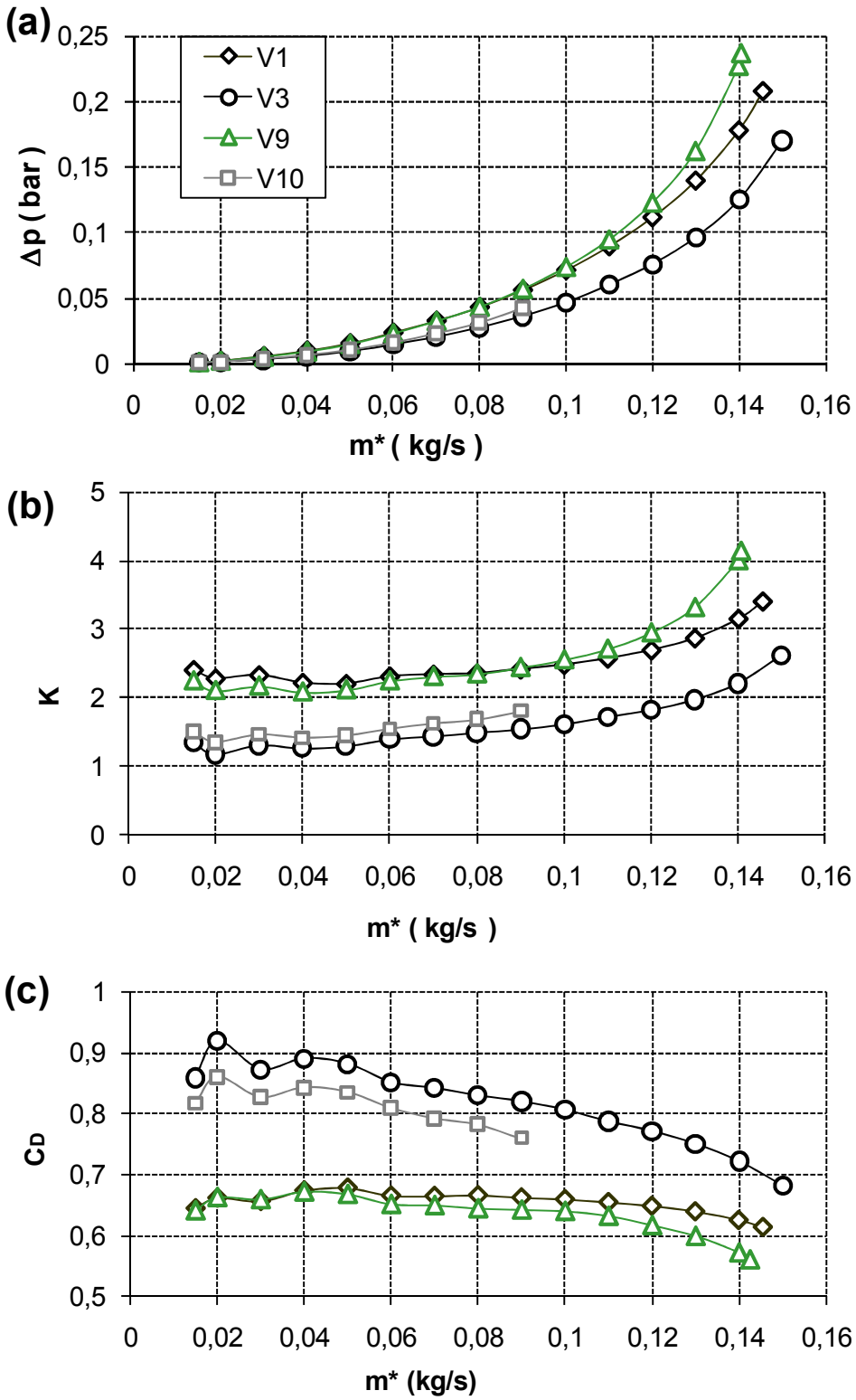

Figure 6. Variation of pressure loss, pressure loss coefficient (K) and discharge coefficient (CD) with respect to mass flow for all the tested elbows.

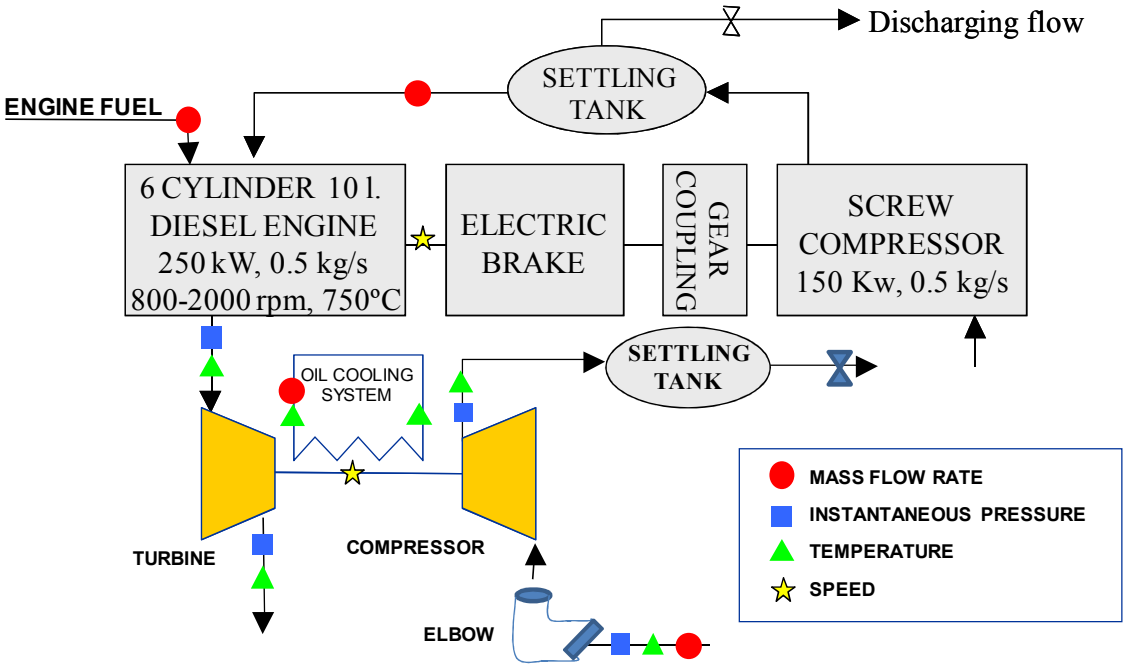

Figure 7. Turbocharger test bench installation and instrumentation

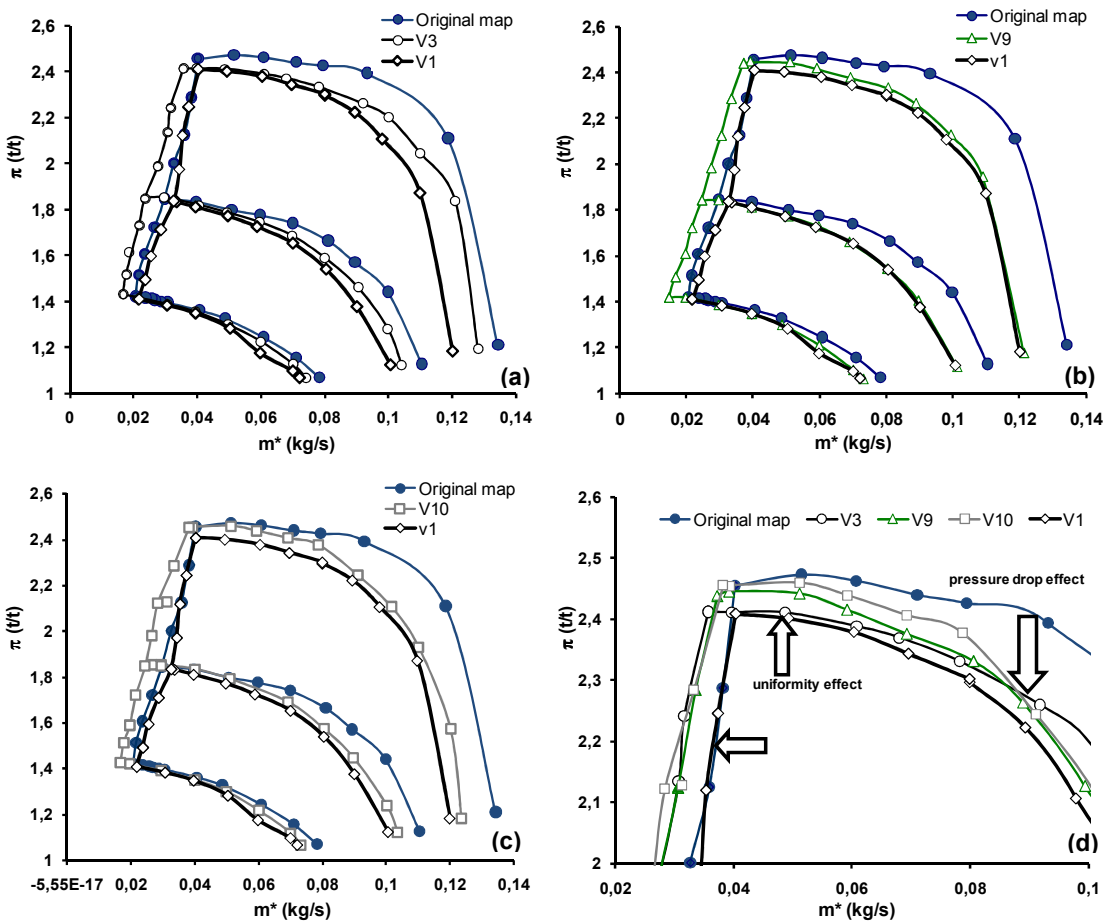

Figure 8. The maps compressor obtained in the turbocharger test bench (V1, V3, V9, V12 and original straight admission)

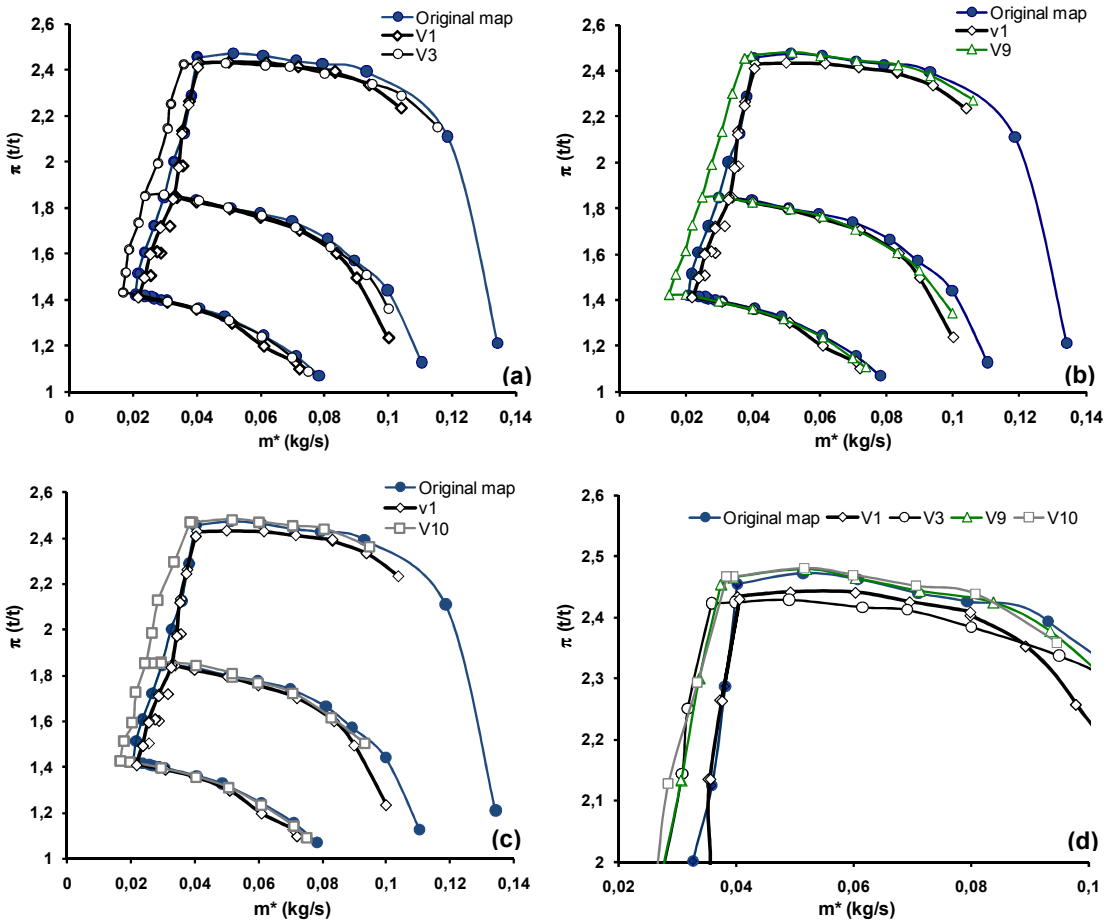

Figure 9. Each case of elbows map with pressure loss added through the results obtained in the test rig.

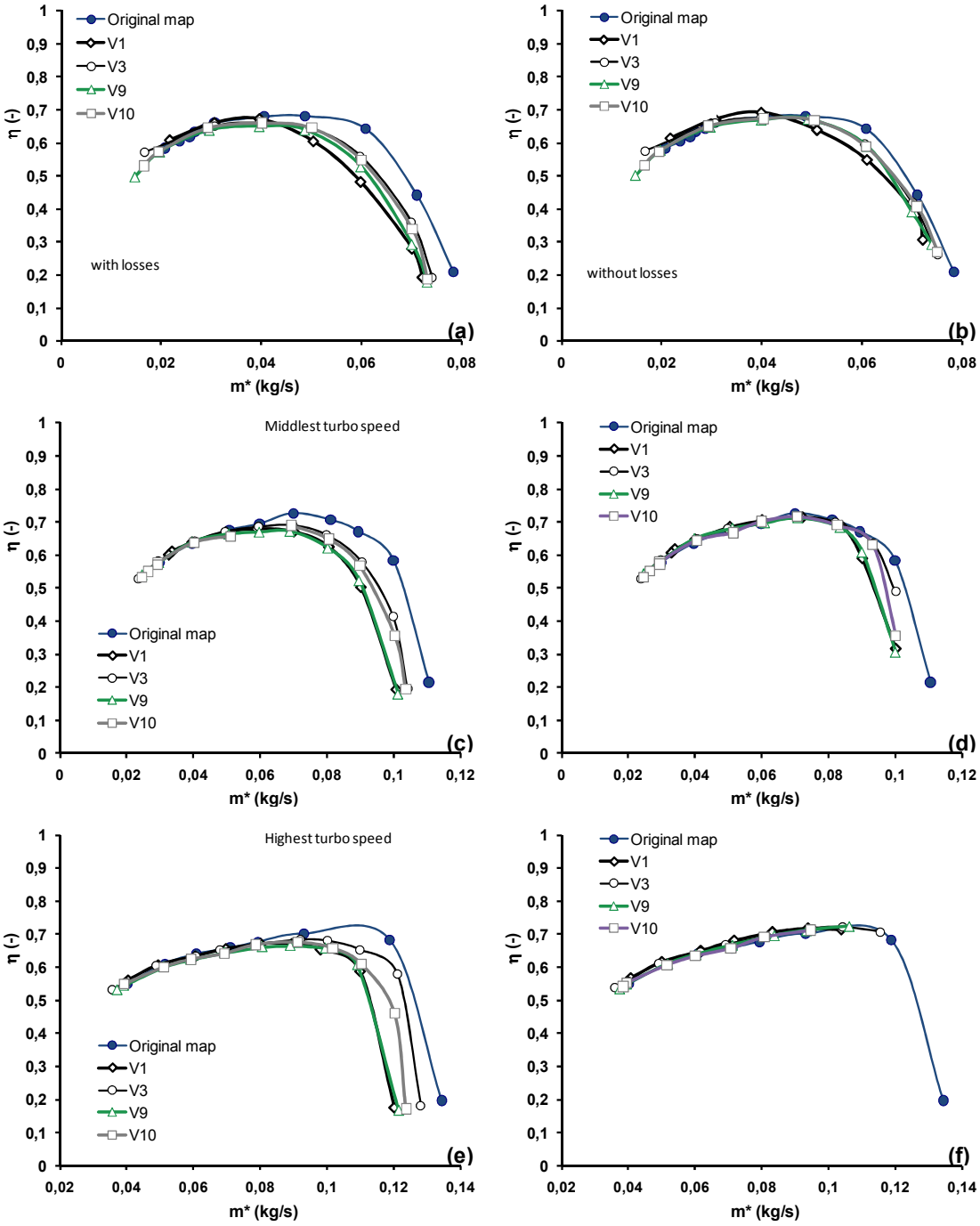

Figure 10. Efficiency comparisons among the different situation with and without pressure loss

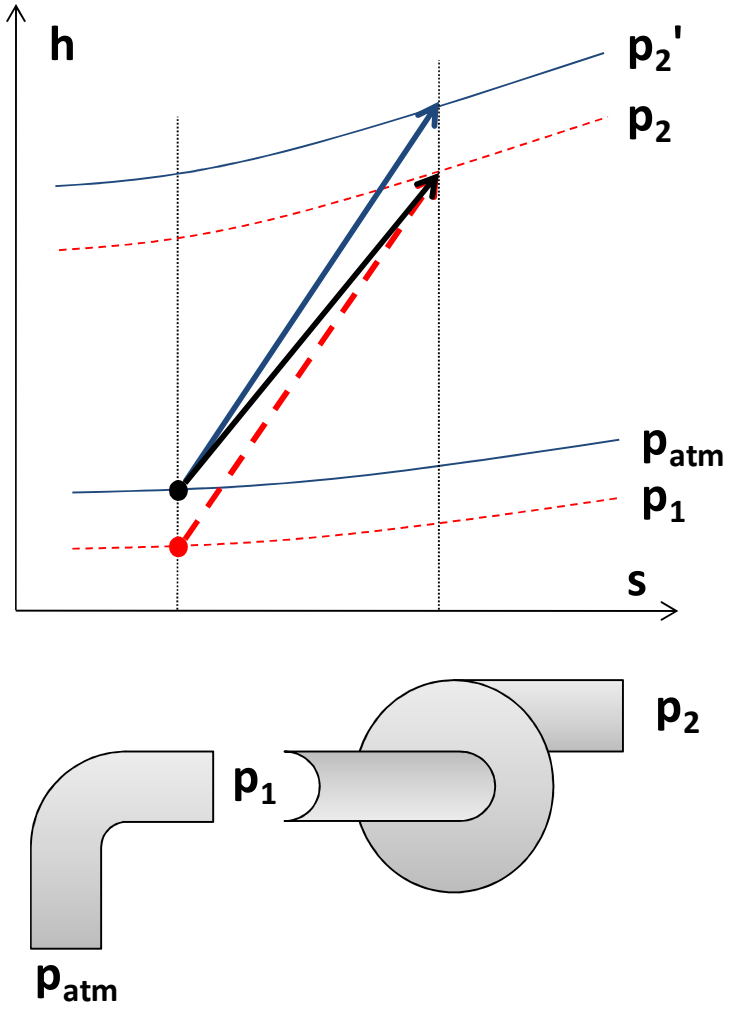

Figure 11. Compressor enthalpy-entropy diagram showing the effect of the pressure loss produced by the elbow at the compressor inlet on the compression ratio.

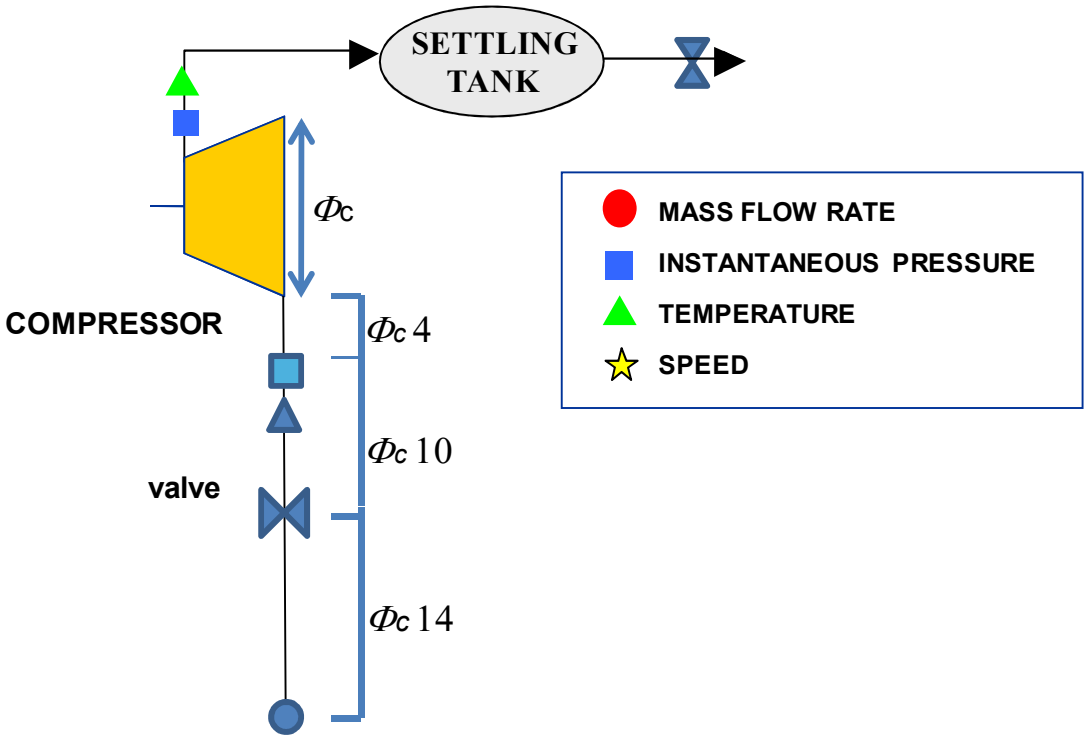

Figure 12. Experimental installation set up.

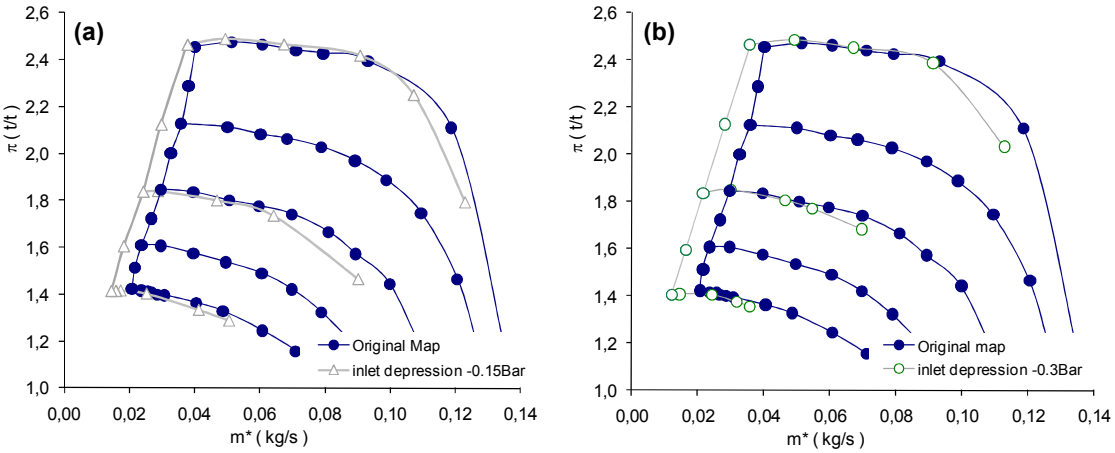

Figure 13. Original map compared with inlet depression (-0.15 and -0.3Bars) compressor map.